TUNNELING EXPERIMENTS WITH SUPERCONDUCTORS

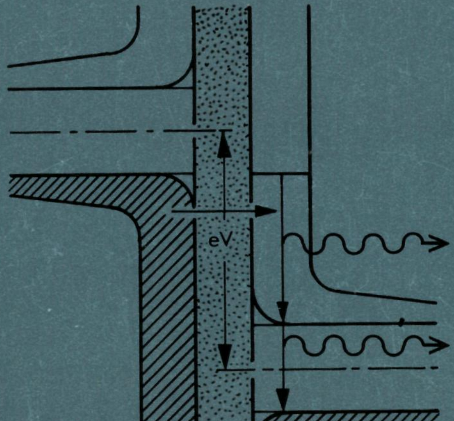

j. bakker

TUNNELING EXPERIMENTS
WITH
SUPERCONDUCTORS

PROMOTOR:

PROF. DR. P. WYDER

TUNNELING EXPERIMENTS
WITH
SUPERCONDUCTORS

PROEFSCHRIFT
TER VERKRIJGING VAN DE GRAAD VAN DOCTOR IN DE
WISKUNDE EN NATUURWETENSCHAPPEN AAN DE KATHO
LIEKE UNIVERSITEIT TE NIJMEGEN, OP GEZAG VAN DE
RECTOR MAGNIFICUS PROF MR F J F M DUYNSTEE
VOLGENS BESLUIT VAN HET COLLEGE VAN DECANEN
IN HET OPENBAAR TE VERDEDIGEN OP DONDERDAG
25 OCTOBER 1973 DES NAMIDDAGS TE 4 UUR

DOOR

JOZEPHUS WILHELMUS MARIA BAKKER

GEBOREN TE ARNHEM

1973
DRUK STICHTING STUDENTENPERS NIJMEGEN

Aan mijn ouders

Aan Marga, Freek en Floor

Bij het verschijnen van dit proefschrift zou ik gaarne al diegenen, die mij gedurende vele jaren hebben geholpen, hartelijk willen bedanken.

In het bijzonder Herman van Kempen, die mij in de mysteries van de lage temperatuur fysika inwijdde, en zoveel geduld betracht heeft. En jou Huub, wil ik bedanken voor de vriendschappelijke steun gedurende de afgelopen twee jaar.

De medewerkers van de technische diensten ben ik zeer erkentelijk voor hun medewerking in vele praktische problemen.

CONTENTS

GENERAL INTRODUCTION 11

CHAPTER I

TUNNELING WITH SUPERCONDUCTORS

I.1 Introduction 13
I.2 The theory of tunneling with superconductors 17
  I.2.1 The phenomenological model of the tunneling process 17
  I.2.2 A more sophisticated approach 27
  I.2.3 The semiconductor diagrams 33
I.3 Specific cases 38
  I.3.1 The superconductor-insulator-normal metal (SN) junction 38
  I.3.2 The superconductor-insulator-superconductor (SS) junctions 41
I.4 Computer evaluation 43
  I.4.1 SN case 43
  I.4.2 SS case 47
References 51

CHAPTER II

APPLICATION TO THERMOMETRY-AN ABSOLUTE THERMOMETER IN THE 0.12 - 1.2 K RANGE

II.1 Outline of the experiment 55

II.2 The use of ruby as a cooling agent 57

II.3 Calibration of carbon thermometers 59

II.4 Experimental details 64

  II.4.1 Preparation of junctions 64

  II.4.2 Cryogenic part of the apparatus 67

  II.4.3 Electronic circuitry 71

II.5 Experimental results 75

II.6 Discussion 84

References 87

CHAPTER III

A NEW PHONON SPECTROSCOPY IN THE VERY HIGH FREQUENCY REGION (10^{11} Hz)

III.1 Introduction 93

III.2 Phonon processes in superconductors 97

III.3 Generation of phonons 103

  III.3.1 Phonon generation with a SS junction .. 103

  III.3.2 Phonon generation by means of a fluorescence film 106

III.4 Detection of phonons 108

III.5 Experimental details 112

III.5.1 Sample preparation 112

III.5.2 Electronic circuitry 115

III.5.3 A local magnetic field 121

III.6 Experimental results on sapphire and ruby 124

III.6.1 Monochromatic phonons in sapphire 124

III.6.2 Monochromatic phonons in ruby 131

III.6.3 Frequency tuning of monochromatic phonons 133

III.7 Phonons and heat pulses in Helium 137

III.7.1 Introduction 137

III,7.2 Second sound propagation in HeII 138

III.7.3 Explosion of a Rollin film 141

III.7.4 Shock waves in He gas 145

III.8 A proposal for a phonon spectroscopy experiment 150

References 153

APPENDIX 159

SUMMARY 162

SAMENVATTING 165

CURRICULUM VITAE 168

GENERAL INTRODUCTION

In this thesis we want to discuss some aspects of one of the most powerful methods for investigating superconducting and other solid state properties: the tunneling process between a superconductor and another metal, which can be normal or superconducting, separated by an insulating layer.

Since the first tunnel experiment was performed in 1960 (1) a huge amount of information has been collected. In the early stage, tunneling with superconductors served as an accurate proof of the then newly developed BCS theory for superconductors (2). It eventually led to a refinement of this theory and to the understanding of some normal state properties of metals. A great number of applications has since emerged from tunnel junctions (3), especially if one is also thinking of Josephson tunneling.

This thesis is divided in three main parts. The first one is concerned with the theory of tunneling between superconductors properly. The main feature is that the simple semiconductor model, as an intuitive way of thinking about tunneling, gives in most cases the correct results. Starting from basic principles, there is still no definite theory of tunneling between superconductors available, but there are a few promising approaches. The second part of this thesis shows a direct link between experiment and the well known BCS theory of superconductivity. Because this theory in its more elaborate form can describe within a few percent the results of superconducting tunneling experiments, it is possible to invert the procedure and to use the temperature dependence of simple experimental curves as an absolute thermometer. The third part introduces a new field of spectroscopy where tunneling junctions are used as generator and detector of monochromatic ultra high frequency phonons in the 10^{11} Hz region. The range of validity and usefulness depends of course on the critical temperature T_c of the used superconductors.

References

(1) I.Giaever, Phys. Rev. Letters 5, 464 (1960).

(2) J.Bardeen, L.N.Cooper and J.R.Schrieffer, Phys. Rev. 106, 162 (1957).

(3) For a general review, see e.g. L.Solymar: 'Superconductive Tunneling and Applications'; Chapman & Hall, London (1972).

CHAPTER I TUNNELING WITH SUPERCONDUCTORS

I.1 Introduction

The story of superconductivity starts way back in 1911 when H. Kamerlingh Onnes discovered that the resistance of a Hg wire below a certain critical temperature T_c becomes unmeasurably small (1). In the years to follow several attempts were made in order to explain the superconducting properties, which were not only restricted to zero resistance but also included the Meissner effect (2). Several phenomenological theories were deduced from the experimental data, which proved to be very useful. We would like to mention the work of Gorter and Casimir (3) who introduced the two fluid model, and the phenomenological electromagnetic theory of the London brothers (4). The phenomenology of the superconducting state was later on further developed by Ginzburg and Landau (5) and by Pippard (6). During the early fifties, several experiments helped to clarify the way towards a microscopic theory. The isotope effect (7) showed that the electron - phonon interactions had to play an important role. But it was not until 1957, when the microscopic theory of the superconducting state was proposed by Bardeen, Cooper and Schrieffer (8), which is now widely known as the BCS theory.

A new condensed state was proposed in which electrons are allowed to form (Cooper) pairs. It may be looked upon physically as one electron being affected by the lattice deformation caused by another electron. In terms of wave vectors, it means that an electron with wave vector k emits a phonon q which is then absorbed again by another electron having a wave vector k'. The nature of the resulting electron - electron interaction turns out to be attractive for sufficiently small phonon energy $\hbar\omega q$. It was shown by Cooper (9) that two electrons with an arbitrarily small attractive interaction in the presence of the filled Fermi sea can form a bound state. By putting a macroscopic fraction of electrons in such a bound state the total energy of the system would be smaller than that of the filled Fermi sphere. The maximum binding energy between electron states is reached when electrons are paired with equal and opposite momentum and spin.

The main assumptions in the derivation of the ground state are as follows:

(i) The superconducting ground state can be expressed in terms of Cooper pairs such that the states $(\vec{k},-\vec{k}')$ are occupied or empty simultaneously.

(ii) The various other interactions may be taken identical in the normal and superconducting state. Only the phonon and screened Coulomb-interaction need to be separated for examination,

(iii) The difference between the phonon - and screened Coulomb interaction - $V_{kk'}$ is defined as follows:

$$V_{kk'} = V \qquad |\varepsilon_k|, |\varepsilon_{k'}| \leq k\,\Theta_D$$
$$= 0 \qquad \text{otherwise}$$

where ε_k is the single-particle energy of the electron and is measured from the Fermi surface and Θ_D is the Debye temperature.

The BCS theory was able to explain most of the experimental data of Brown et al. (10), and the thermal conductivity data of Goodman (11) had a better fit with an exponential law, indicating an energy gap, as opposed to the until then successfull Gorter-Casimir cubic law.

However, at this time nobody had measured the energy gap directly; but in that same year 1957 Glover and Tinkham (12) were successful in reaching the far infrared region of the electromagnetic spectrum, and they observed in lead a discrete drop in the absorption above a well defined frequency, which was then identified as the energy gap and found to be in the right order of magnitude within the BCS theory. Later results on tin (13) also confirmed the first results.

However, in a few years, experimentally some small deviations from the BCS theory were found. For instance the critical field curve of Pb did not fit to the BCS theory exactly, and a careful analysis of the absorption measurements on Pb gave a gap which was greater than 3.5 $k_B\,T_c$, the BCS value. It is not a coincidence that Pb also has a low Θ_D (= 95 K) which is not terribly much higher than the energy-gap value (Δ = 12 K), which means that some of the approximations in the simple-minded BCS theory are not justified. When taking these so called strong coupling effects into account, one was able to explain the Pb data perfectly well within the framework of the extended BCS theory (15).

Unfortunately, the technique of far infrared absorption is rather complicated and also was not very well suited for measurements at energies outside the gap region because absorption is already too great for energies slightly higher than Δ, the superconducting energy gap.

Then, at the VIIth International Low Temperature Conference in Toronto (1960),for the first time a new and much more simpler technique was introduced by Giaever (14): tunneling. By this technique one can measure not only the gap with very good accuracy, but also one is able to deduce directly the density of states as a function of energy and to compare this with the BCS theory. This led in the following years to the solution of the 'bad actors' problem of Pb and Hg, especially by the work of Rowell and McMillan (15). As a result, the BCS theory was refined to include also the phonon effects (when Θ_D is not $\gg T_c$) and nowadays the more elaborate BCS theory is accurate to some fraction of a percent for all superconductors.

Let us conclude this introduction by mentioning some of the enormous wealth of information the tunnel junctions has provided us.

First the dependance of the energy gap on various parameters, such as temperature (16), magnetic field dependance (17), transport current (18) and crystal orientation (19). The last one is important because it showed anisotropy of the gap, where in the

BCS theory in its primitive form only an isotropic model was considered. The disappearance of the gap (gapless superconductivity) due to magnetic impurities or magnetic field was first measured by Reif and Woolf (20), and by Tinkham and Millstein (21). We should also mention numerous proximity effect measurements, e.g. Smith et al. (22), and Hauser (23), studies of vortex - structures and so on. Information on the lifetime of the excited electrons was obtained by Ginsberg (24), and Miller and Dayem (25).

Of course numerous device applications have been found and were reviewed(26) in the last couple of years. One of these, the junction as an absolute thermometer, is one of the subjects in this thesis.

I.2 The theory of tunneling with superconductors

I.2.1 Phenomenological model of the tunneling process

The problem of tunneling through a barrier is as old as quantum mechanics. In this first paragraph we begin with tunneling between normal metals, in order to show the basic ideas behind a simple theory of tunneling with superconductors. This simple theory will then be sketched, and it will be shown that under certain assumptions this theory leads to the correct results. The second paragraph I.2.2 tries to justify these assumptions in a more realistic way. The last paragraph of this chapter demonstrates the physical meaning of the semiconductor model and shows the obvious shortcoming of this model.

The derivation of the formula for the tunneling current between two metals separated by an insulating layer was first done by Sommerfeld and Bethe (27); their analysis has been applied to many problems. A modern presentation and extension of their work is given by Holm (28). Further theoretical work was stimulated by the invention of the tunnel diode by Esaki (29), who used the formalism to describe tunneling in degenerate semiconductor junctions. This formalism will be applied to superconductors in paragraph I.2.3.

In the following 'V' denotes the energy difference eV between Fermi levels due to a potential difference V of two metals separated by a potential barrier in thermal equilibrium and at T=0 K. The two Fermi levels E_{F1} and E_{F2} have to coincide for thermodynamical reasons (Fig.I.1a). If we apply a negative bias voltage to the metal (1) on the left, all the electrons on the left will have an energy increase of V and consequently the energy diagram versus density of states will look like Fig.I.1b.

We must keep in mind that the electrons of both metals behave like independent Fermi-Dirac particles occupying a given state of energy E with a probability $f(E)=[1+\exp(\beta E)]^{-1}$, where $\beta=1/kT$ The number of electrons which will move from left to right in an energy interval dE must be proportional to the number of occupied states at the left, that is to

$$N_1(E-V)f(E-V)dE \qquad (I.1)$$

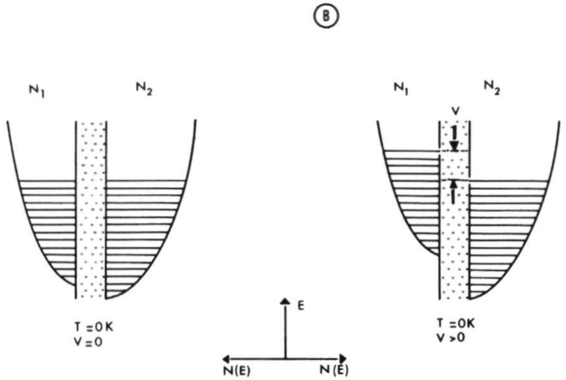

Fig.I.1 Normal metal-insulator-normal metal junction. (A) The density of states versus energy diagram at T = 0 K in thermal equilibrium. At T = 0 K, states are filled up to the Fermi levels E_{F1} and E_{F2}. This is represented by the shaded area, a convention which holds for all of the following diagrams. (B) The junction with an applied bias voltage V. Electrons are allowed to tunnel from left to right.

where N_1 is the density of states of the left metal. We will measure the energy from the Fermi level of the right metal. Only if there are unoccupied states at the right, the electrons can move to the right, hence the current must be proportional to

$$N_2(E)[1-f(E)] \qquad (I.2)$$

where N_2 is the density of states in metal 2. Taking into account the tunneling probability $P_{12}(E)$ through the barrier, one gets for the current $I_{1\rightarrow 2}$ from the left to the right for a certain energy E

$$I_{1\rightarrow 2} \propto P_{12}(E)N_1(E-V)N_2(E)f(E-V)[1-f(E)] \qquad (I.3)$$

The same argument holds of course for a current from the right to the left

$$I_{2\rightarrow 1} \propto P_{21}(E)N_1(E-V)N_2(E)f(E)[1-f(E-V)] \qquad (I.4)$$

If we assume the principle of detailed balance

$$P_{12}(E)=P_{21}(E)$$

we get by integrating over all energies for the total current

$$I \propto \int_{-\infty}^{+\infty} P(E)N_1(E-V)N_2(E)[f(E-V)-f(E)]\,dE \qquad (I.5)$$

or

$$I \propto \int_{-\infty}^{+\infty} P(E)N_1(E+V)N_2(E)[f(E)-f(E+V)]\,dE \qquad (I.6)$$

by making the transformation E → -E, and using $f(x)=1-f(-x)$. We make the following assumptions:

(i) $P(E)$ is independent of energy. This seems to be justified for low bias voltage, i.e. $V \ll E_F$.

(ii) The density of states is a slowly varying function and can therefore be replaced by its value at the Fermi level:

$$N_1(E+V) \cong N_1(E) \cong N_1(0),$$
$$N_2(E) \cong N_2(0).$$

With these assumptions (I.6) reduces to

$$I \propto AN_1(0)N_2(0)\int_{-\infty}^{+\infty}[f(E)-f(E+V)]\,dE \qquad (I.7)$$

Here, A contains the transition probability P and unknown geometry factors. For small voltages the difference of the two Fermi functions can be approximated by

$$f(E)-f(E+V)=-V\,\partial f/\partial E \qquad (I.8)$$

If in addition the temperature is low, ($kT \ll E_F$), the derivative of the Fermi functions can be replaced by a δ-function, giving for the current

$$I=AN_1(0)N_2(0)V \qquad (I.9)$$

This means that a metal-insulator-metal configuration obeys Ohm's law for sufficiently low bias voltages and temperatures which is confirmed by experiments.

The next step is to replace one of the metals, say 2, by a superconductor. For this purpose, Giaever et al. (30) developed a semiphenomenological theory based on the foregoing analysis, adding the following assumptions:

(iii) The probability P is independent of whether the metals are superconducting or not.

(iv) The density of states in a superconductor at T=0 K is given by the BCS expression:

$$N_S(E)=n_S(E)N_N(E) \qquad (I.10)$$

$$n_S(E)=|E|/(E^2-\Delta^2)^{\frac{1}{2}} \qquad |E| \geq \Delta$$

$$n_S(E)=0 \qquad |E| < \Delta$$

With assumption (ii) it follows that

$$N_S(E)=N_N(0)n_S(E) \qquad (I.11)$$

Then for the current between a normal metal and a superconductor we get from (I.5)

$$I_{NS}=C_{NN}\int_{-\infty}^{+\infty} n_S(E)[f(E-V)-f(E)]\,dE \qquad (I.12)$$

where $C_{NN}=AN_1(0)N_2(0)$

is the conductance when both metals are normal. The only difference with (I.7) is the appearance of the BCS-density of states factor $n_S(E)$, i.e. the current-voltage characteristic of such a junction is directly related to the BCS-density of states $N_S(E)$ and the Fermi-function f(E). Let us make this more clear by differentiating (I.12) with respect to the voltage. We obtain:

$$dI_{NS}/dV=C_{NN}\int_{-\infty}^{+\infty} n_S(E)\left(\frac{\beta\exp[\beta(E-V)]}{\{1+\exp[\beta(E-V)]\}^2}\right)dE \qquad (I.13)$$

The second factor is a bell-shaped function which is symmetrical about its maximum at E=+V. The magnitude of this maximum is proportional to 1/T and the function degenerates for T=0 to a δ-function. So for T=0 K (I.13) reads

$$(dI_{NS}/dV)_{T=0} = C_{NN}\int_{-\infty}^{+\infty} n_S(E)\delta(E-V)dE = C_{NN}n_S(V) \qquad \text{(I.14)}$$

$$= C_{NN}|V|/(V^2-\Delta^2)^{\frac{1}{2}} \qquad |V| \geqslant 0$$

$$= 0 \qquad |V| < 0$$

If Δ is energy independent, (I.14) can be integrated to give

$$(I_{NS})_{T=0} = C_{NN}(V^2-\Delta^2)^{\frac{1}{2}} \qquad |V| \geqslant 0 \qquad \text{(I.15)}$$

$$= 0 \qquad |V| < 0$$

To make a pictorial view of these formulas we show a semiconductor model of a normal metal-insulator-superconductor junctions. In Fig.I.2a all states are filled up to $E_F-\Delta$ and there are no filled states above the gap. This represents the situation at T=0 K. At a finite temperature there are electrons above the gap and holes below. Note that the energy scale compared to Fig.I.1 is considerably smaller, because $\Delta/E_F \approx 10^{-3}$.

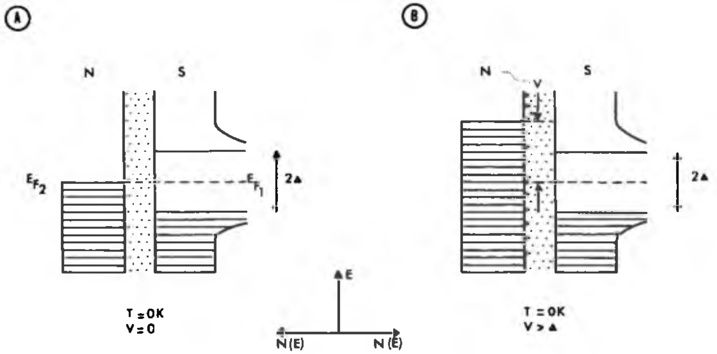

Fig.I.2 Normal metal-insulator-superconductor junction. (A) The density of states versus energy diagram at T = 0 K in thermal equilibrium. (B) The junction with an applied bias voltage V. Electrons are allowed to tunnel whenever V > Δ.

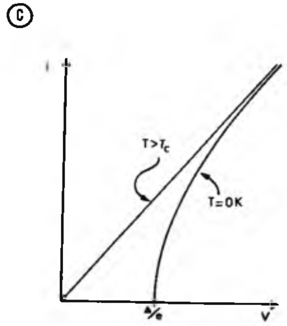

Fig.I.2 (C) The corresponding current-voltage characteristic at $T = 0$ K and for $T > T_c$.

From Fig, I.2.a it is clear that for small bias voltages and at thermal equilibrium there cannot be a tunneling current because of the forbidden energy range. This situation holds until $V = \Delta$, where one has a sharp rise in current because the electrons face a large density of states at the right. At voltages $V \gg \Delta$ the current-voltage relation gradually approaches the Ohmic behaviour as if both metals were normal.

For $T \neq 0$ K, a more sophisticated discussion will be given in the next chapter. However, a more qualitative discussion can also be given in terms of our semiconductor model. In the semiconductor diagrams of Fig.I.3 some of the electrons at the left have ener-

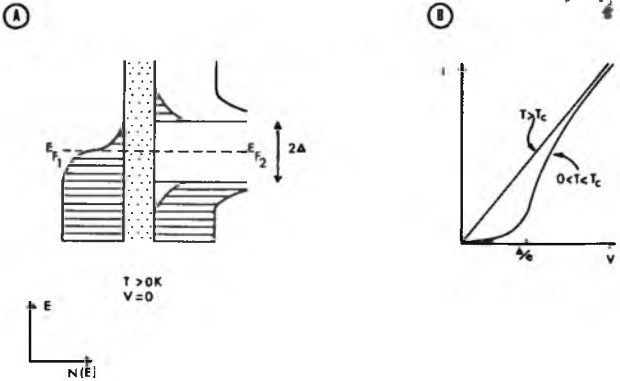

Fig.I.3 Normal metal-insulator-superconductor junction. (A) The density of states versus energy diagram at finite temperatures. (B) The corresponding current-voltage characteristic.

gies in excess of E_F even at thermal equilibrium, and there are also some normal electrons above the gap on the right. However, the rather sharp rise in current at Δ/e is still a remaining feature (Fig.I.3.b).

Let us finally consider the case of tunneling between two superconductors (neglecting the Josephson-current), and let us start assuming identical gaps. In the same way as above we get from (I.5) the following expression for the tunneling current:

$$I_{SS}=C_{NN}\int_{-\infty}^{+\infty} n_S(E-V)n_S(E)[f(E-V)-f(E)]\,dE \qquad (I.16)$$

In Fig.4 the energy diagrams are shown again. At T=0 K at thermal equilibrium and with small bias voltages there is no current flowing.

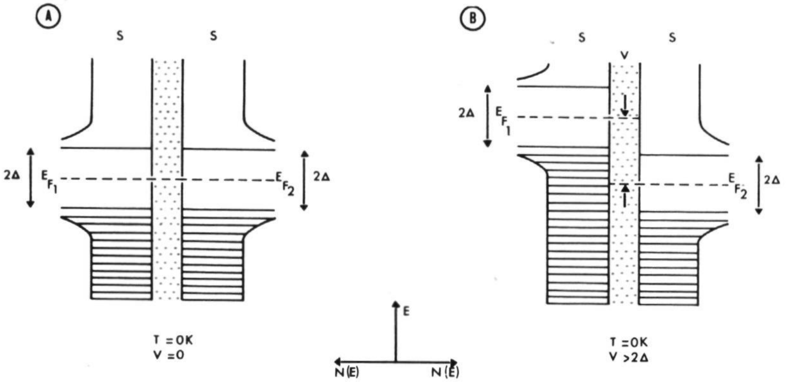

Fig.I.4 Superconductor-insulator-superconductor junction. (A) The density of states versus energy diagram at T = 0 K in thermal equilibrium. (B) The same junction with a bias voltage V > 2Δ.

Up until a bias voltage of V=2Δ/e there is still no current. At a bias 2Δ/e there is a sharp rise because electrons on the left suddenly gain access to the states above the gap on the right. Again at finite temperature there will be some rounding off of the current-voltage characteristic just as seen in Fig.I.3.b.

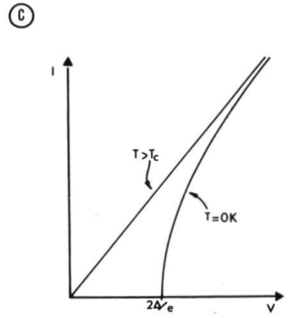

Fig.I.4 (C) The corresponding current-voltage characteristic.

For two different superconductors the same formula (I.16) holds, except that two different energy gaps Δ_1 and Δ_2 have to be used in the formulas for the density of states (I.10). For T=0 K we may apply the same diagram as Fig.I.4. However, for $T\neq0$ the situation is different. Then we may still assume that the normal electron states above the energy gap are empty but there are some thermally excited normal electrons in the smaller gap superconductor as shown in Fig.I.5.a for the case of thermal equilibrium. Applying a voltage, the current will start to flow immediately and will increase with increasing voltage until $V=\Delta_2-\Delta_1$ (Fig.I.5.b). At this stage all the electrons above the gap on the

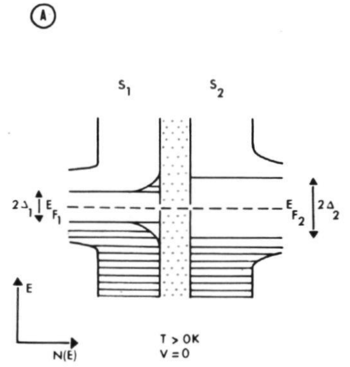

Fig.I.5 A junction consisting of two non-identical superconductors. (A) The density of states versus energy diagram at finite temperatures and zero bias.

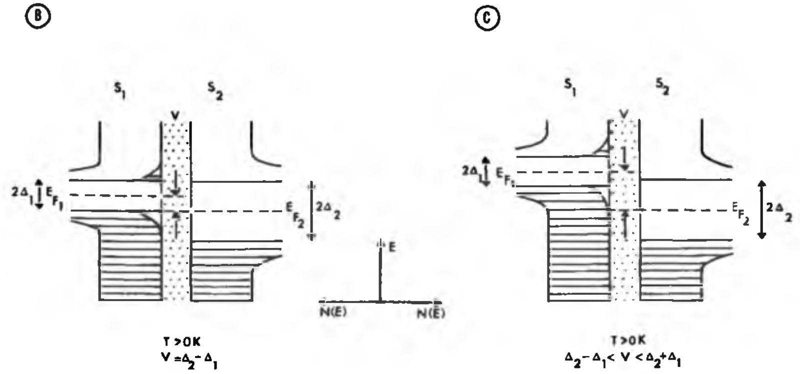

Fig.I.5 (B) The junction with a bias voltage $V = \Delta_2 - \Delta_1$. (C) The junction with a bias voltage $\Delta_2 - \Delta_1 < V < \Delta_2 + \Delta_1$.

left can tunnel across into empty states at the right. If the voltage is increased further, the number of electrons capable to tunnel across is still the same but they face a smaller density of states, hence the current decreases (Fig.I.5.c). The decrease continues until $V=\Delta_1+\Delta_2$ (Fig.I.5.d). At this point electrons from below the gap on the left gain access to empty states at the

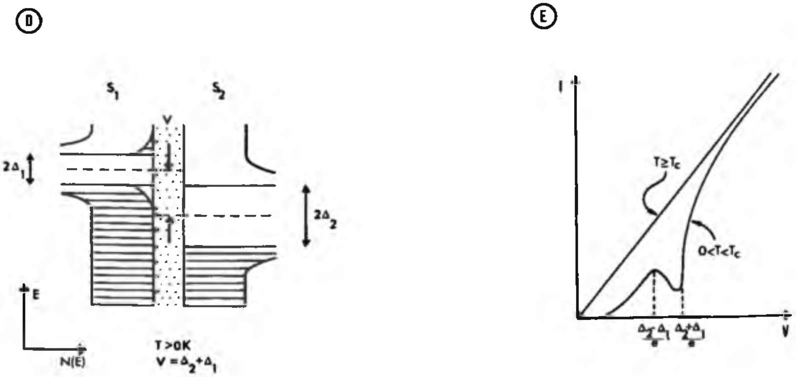

Fig.I.5 (D) The junction with a bias voltage $V = \Delta_1 + \Delta_2$. (E) The corresponding current-voltage characteristic.

right and there will be the well known rise in current up to the Ohmic behaviour. This sort of junction exhibits a negative resistance region between $V = \Delta_2 - \Delta_1$ and $V = \Delta_2 + \Delta_1$.

The semi-phenomenological theory outlined here was criticized for its apparently unjustified assumptions (cf. page 20, 21). However, from the detailed fit Giaever et al. (30),(16) and others obtained with the experimental data, it appears that it may be possible to justify these assumptions. The various ways to do this is the subject of the next paragraph.

I.2.2 A more sophisticated approach

The microscopic theories describing a current flowing through a weak link (which may be a thin oxide layer or a thin metal film) can most elegantly and effectively be described with the help of Green's functions (31). In view of the complexity of the problem most often perturbation theory approach has to be used. If the coupling between two metals (normal or superconducting) is weak, it may be treated as a small pertubation on the uncoupled system consisting of the two metals. We look at the transfer of electrons across the barrier as an instantaneous process and we will ignore interactions between electrons or electrons with phonons within the barrier. Bardeen (32) was the first to use time dependent perturbation methods on the tunneling problem which implies the use of a tunneling Hamiltonian. The use of the latter was further established by Cohen et al. (33), by Bardeen (34) and by

Prange (35).

Let us denote the two metals by subscripts (1) and (2) and use the $\vec{k}$ electron states for (1) and $\vec{q}$ electron states for (2). The Hamiltonian for the whole system is then written as

$$\mathcal{H} = \mathcal{H}_1 + \mathcal{H}_2 + \mathcal{H}_T \qquad (I.17)$$

$\mathcal{H}_1, \mathcal{H}_2$ are the full many body Hamiltonians for metal (1) and (2) respectively. $\mathcal{H}_T$ is that part of $\mathcal{H}$ which serves to describe the transfer of electrons from either side. In the formalism of second quantization

$$\mathcal{H}_T = \sum_{k,q,\sigma} \{T_{kq} a^{+}_{k\sigma} a_{q\sigma} + T_{qk} a^{+}_{q\sigma} a_{k\sigma}\} \qquad (I.18)$$

where a^{+}, a are the creation and annihilation operators for one electron states with spin σ. T_{kq} is the tunneling matrix element which connects states on both sides of the barrier.

It is possible to evaluate T_{kq} using WKB methods, and according to Harrison (36) one gets

$$|T_{kq}|^2 \propto v_k v_q |I_{kq}|^2 \qquad (I.19)$$

where v_k and v_q are the components of the group velocity of the electrons normal to the barrier in both metals. The transverse component of the momentum is conserved. I_{kq} is the tunneling integral of the type one often finds in these kind of problems and which depends exponentially on the thickness of the insulating layer. (37). It is possible to show (36) that only those electrons with energies near the Fermi value $\varepsilon_F = \frac{\hbar^2 k_F^2}{2m}$ contribute appreciably to the tunneling integral $|I_{kq}|^2$. Therefore, we may replace ε_k by ε_F in the expression for $|I_{kq}|$. In addition, if one or both metals are superconductors, the energyshifts involved are of the order of

10^{-3} eV which again can be neglected in the energy variation of $|I_{kq}|^2$. Hence in first approximation, $|I_{kq}|^2$ can be considered as energy independent. For the group velocities v_k and v_q, one has

$$\vec{v}_k = \hbar^{-1}\nabla_k E_k,$$

and

$$|\vec{v}_k| \propto (N_N(E_k))^{-1},$$

Hence it follows that the product $v_k v_q N_N(E_k) N_N(E_q)$ is energy independent, which gives the assumption used in I.2.1 that the tunneling matrix element depends very weakly on energy and does not alter when one, or both, of the metals become superconducting. $|I_{kq}|^2$ plays the same role as the probability P used in I.2.1. Therefore we see, that it is not possible to obtain information on the density of states from tunneling between normal metals, because of the cancelling effect between v and the density of states. However, for tunneling between a normal metal and a superconductor it follows from (I.10) and (I.11) that

$$v_k v_q N_S(E_k) N_N(E_q) \propto n_S(E_k),$$

i.e. for a superconductor-oxide-normal metal junction this product is proportional to the BCS density of states, which gives immediately the results of the previous paragraph.

However, in a superconductor we are not dealing anymore with 'normal' electrons but with quasi-particles described by i.e. the Bogoliubov-Valatin transformation (38). The relation between electrons and quasi-particles is given by the energy dependent coefficients u_k and v_k:

$$u_k^2 = \tfrac{1}{2}[\,1+(\varepsilon_k/(\varepsilon_k^2+\Delta_k^2)^{\frac{1}{2}})] = \tfrac{1}{2}[\,1+\varepsilon_k/E_k] \qquad \text{(I.20.a)}$$

$$v_k^2 = \tfrac{1}{2}[\,1-(\varepsilon_k/(\varepsilon_k^2+\Delta_k^2)^{\frac{1}{2}})] = \tfrac{1}{2}[\,1-\varepsilon_k/E_k] \qquad \text{(I.20.b)}$$

u_k and v_k are called the 'coherence factors' and due to normalization conditions obey the relation $u_k{}^2+v_k{}^2=1$. In the usual BCS theory, $u_k{}^2$ is the probability of having a pair state $(\vec{k},-\vec{k})$ occupied, and $v_k{}^2$ is the probability that this state is empty. We will show later that these coherence factors cancel in the formula for the current through a tunnel junction, and it is this cancellation effect which justifies the simple theory presented in I.2.1.

Let us now proceed to the calculation of the tunnel current, based on (I.17) and (I.18). In the formalism of second quantization, one gets for a normal metal-insulator-superconductor junction for the different parts of the Hamiltonian

$$\mathcal{H}_1 = \sum_{k,\sigma} \varepsilon_k a^+_{k\sigma} a_{k\sigma} \qquad \text{(I.21)}$$

$$\mathcal{H}_2 = \sum_q E_q(\alpha^+_q\alpha_q + \beta^+_q\beta_q) + \mathcal{H}\text{int} \qquad \text{(I.22)}$$

$$\mathcal{H}_T = \sum_{kq\sigma}[\,T_{kq}a_{k\sigma}a^+_{q\sigma} + T_{qk}a^+_{q\sigma}a_{k\sigma}]$$

Here k represent states in the normal metal (1), and q in the superconductor (2); ε_k is the normal electron energy measured from the Fermi level; $E_q=(\varepsilon_q{}^2+\Delta^2)^{\frac{1}{2}}$ is the superconducting quasi-particle energy and the α's and β's, the quasi-particle operators, are related to the normal electron operators by the Bogoliubov-Valatin transformation (38):

$$\alpha_q = u_q a_{q\uparrow} - v_q a^+_{-q\downarrow} \qquad \text{(I.23.a)}$$

$$\beta_q = u_q a_{-q\downarrow} - v_q a^+_{q\uparrow} \qquad \text{(I.23.b)}$$

where a_{-q} indicate the time-reversal conjugate of a_q^+. $\mathcal{H}_{int}$ is the interaction Hamiltonian within the superconductor and has terms containing operators of the form $\alpha^+\beta^+$, $\beta\alpha$ etc., and four-electron-operators.

We calculate the current by evaluating $<\frac{d}{dt}N_{1\to 2}>$, the average value of the rate of change of the number of superconducting electrons. The equation of motion reads as

$$i\hbar\frac{d}{dt}N_{1\to 2} = [N_{1\to 2}, \mathcal{H}] = [N_{1\to 2}, \mathcal{H}_T] \qquad (I.24)$$

$\mathcal{H}_1$ and $\mathcal{H}_2$ conserve the number of electrons and therefore commute with $N_{1\to 2}$. From (I.24) and (I.18) and making use of (I.23.a,b) we obtain:

$$i\hbar\frac{d}{dt}N_{1\to 2} = \sum_{kq}\{T_{qk}[u_q< \alpha_q^+ a_{k\uparrow}> + v_q <\beta_q a_{k\uparrow}>] + \text{similar terms}\} \qquad (I.25)$$

To compute terms like $<\alpha_q^+ a_{k\uparrow}>$ we would have to solve the exact equation of motion by commuting them with $\mathcal{H}$. At this point one usually introduces a Hartree-Fock(HF)approximation. After commuting $\alpha_q^+ a_{k\uparrow}$ with $\mathcal{H}_{int}$ one gets terms like

$$<\alpha_1^+\beta_2^+\beta_3 a_{k\uparrow}> \text{ etc.}$$

In the HF approximation, the expectation value of these four-electron-operators are replaced by factorized products

$$<\alpha_1^+\beta_2^+> <\beta_3 a_{k\uparrow}> - <\beta_2^+\beta_3> <\alpha_1^+ a_{k\uparrow}>,$$

evaluated to first order in T_{qk}. Terms of the type

$$<\alpha_1^+\beta_2^+> <\beta_3 a_{k\uparrow}>$$

ultimately lead to the Josephson type of tunneling current in a junction (39). When we drop these terms the result from (I.25) is

$$< \frac{d}{dt} N_{1\to 2} > = \frac{2\pi}{\hbar} \sum_{kq} | T_{kq} |^2 \{ u_q^2 \, [f(\varepsilon_k) - g(E_q)] \, \delta (E_q - \varepsilon_k) + v_q^2 [f(\varepsilon_k) - (1 - g(E_q))] \, \delta (E_q + \varepsilon_k) \},$$

where f is the Fermi-Dirac (FD) distribution and g is the modified FD distribution, defined as

$$g(E_q) = f(| \varepsilon_q |).$$

It is important to note that there are two channels q and q' such that

$$u_q^2 + u_{q'}^2 = 1$$

where $q < q_F$ and $q' > q_F$, $E_q = E_{q'}$ (cf. Fig.I.6.c of paragraph I.2.3). The same holds for v_q:

$$v_q^2 + v_{q'}^2 = 1$$

It is now possible to calculate the current by introducing a voltage difference, replacing the sum over k and q states by an integral over the energy and using

$$I_{NS} = e[< \frac{d}{dt} N_{1\to 2} > - < \frac{d}{dt} N_{2\to 1} >]$$

one finally gets

$$I_{NS} = \frac{2\pi}{\hbar} | T |^2 N_{1N}{}^{(0)} N_{2N}{}^{(0)} \int_{-\infty}^{+\infty} d\varepsilon \; n_1(\varepsilon) n_2(\varepsilon + V) [f(\varepsilon) - f(+V)]$$

where we refer to (I.10) and (I.11) for the expression of the density of states in the integrand. Hence we obtained the familiar result derived from phenomenological arguments in the previous paragraph I.2.1: (I.12), (I.16).

It should be emphasized once again that we have neglected terms giving rise to the Josephson effect. In our experiments, the Josephson effect was usually suppressed by applying a small magnetic field.

To conclude we remark that it is really the twofold degeneracy of the levels in the superconductor which leads to the disappearance of the factors u_k^2. It is this same degeneracy which often leads to confusion if one uses the semiconductor model, as we shall see in the next paragraph.

Further, one may ask what will happen to the I-V curves when higher order effects play a role. Indeed such effects are seen (40,41) in certain circumstances, that is for a 'patchy' oxide layer. Schrieffer et al. (42) have indeed explained these effects by expanding to $|T_{kq}|^4$ in (I.25).

I.2.3 The semiconductor diagrams

The so called one-particle or semiconductor diagrams are very convenient to analyse the current-voltage characteristics obtained by experiment. There is a very loose analogy between superconductors and semiconductors (both have an energy gap around the Fermi energy) and therefore it can sometimes be useful to analyse the superconducting properties in terms of the usually more familiar semiconductors.

Of course there are very fundamental differences between semiconductors and superconductors. One might say that in a semiconductor the energy gap caused by a periodic lattice potential fixed to the lattice is responsible for the zero conductivity at zero temperature, while in superconductors the internal interactions of the electrons are responsible for an energy gap in the excitation spectrum, which leads to the infinite conductivity(43).

Despite the fact that the quasi-particles used in the Bogoliubov (38) description of the superconducting state are different from the excitation in the normal state ('normal' electrons) the electron-hole excitations which are so familiar from the semiconductor picture fails only in a very few cases to explain the behaviour of superconducting tunnel junctions. Examples for this failing are the Tomasch effect (44) (which needs to be explained in terms of E_k diagrams), multiparticle tunneling (45) and the Josephson effect (39).

In the following we will try to explain those features of the superconductor which led to the common use of the semiconductor model, but one should always be very careful in using the semiconductor model, keeping in mind that it is only an analogy.

Let us look at the one-particle energy-wavevector diagram for a normal metal as in Fig.I.6.a. At T=0 K all states up to $k=k_F$ are occupied and the states above $k>k_F$ are empty. An excitation can consist of an electron having a positive energy $-\varepsilon_k=-(E_k-E_F)>0$. From

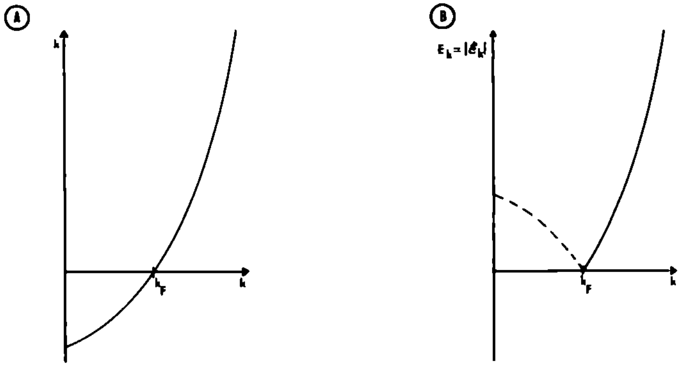

Fig.I.6 (A) One-electron energy levels for the free electron gas. (B) One-particle excitation spectrum for the normal state.

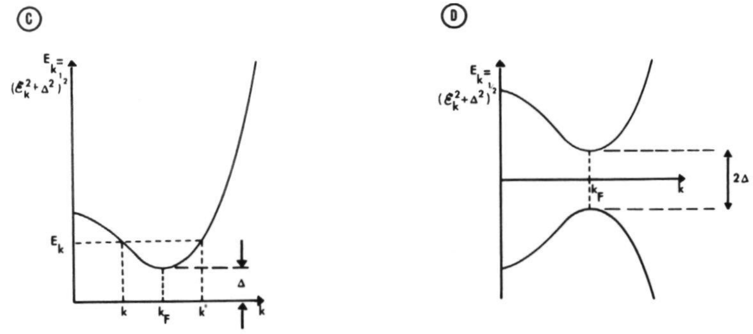

Fig.I.6 (C) One-particle excitation spectrum for the superconducting state. (D) One-particle quasi-electron and quasi-hole spectrum for the superconducting state (or the modified semiconductor model).

this we can derive the one particle excitations, as shown in the full-curve while the dashed curve gives the hole excitations (Fig.I.6.b).

The situation for a superconductor is totally different. As one can see from the excitation diagram for a superconductor it is possible to inject electrons in <u>two</u> states k and k' above and below the Fermi value k_F (Fig.I.6.c). These two states are related by $\varepsilon_k = -\varepsilon_{k'}$ (if $\Delta_k = \Delta$, independent of k). The probability that the electron of energy E_k can enter either state is $u_k^2 + u_{k'}^2 = 1$, according to (I.20). Therefore, all states k (above and below the Fermi level) can accept one electron. The same argument holds for holes, and so we can construct a complete excitation diagram for a superconductor as shown in Fig.I.6.d, where the quasi-electron energy $E_k^{(e)}$ is plotted positively upward and the quasi-hole energy $E_k^{(h)}$ is plotted positively downward. The energy needed to create an excitation is Δ or $\approx 10^{-3}$ eV. It is obvious that for $\Delta \to 0$

the hole curve for $|k|<k_F$ and the electron curve for $|k|>k_F$ are giving the 'normal' excitation curve of Fig.I.6.a. The remaining parts, that is the electron curve for $|k|<k_F$ and the hole curve for $|k|>k_F$, loose their sense because the probability of injection in these states vanishes when $\Delta=0$.

When we now consider the semiconductor diagram again, represented in Fig.I.7, the states above the gap must not be thought of as coming from Bloch states with $k>k_F$ nor the states below the lower edge from Bloch states with $k<k_F$. <u>All</u> k states appear above the gap edge and refer to added electrons, <u>all</u> k states appear below the lower gap edge and refer to holes. In a semiconductor, states above and below the gap are basically different arising from different single particle energy bands.

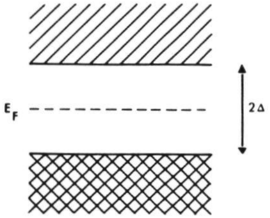

Fig.I.7 Conventional semiconductor model for the excitation spectrum of a superconductor.

Of course it is possible to represent all tunneling processes with the help of the E_k excitation diagrams (46). Here we will give two examples. In Fig.I.8 tunneling is shown between a normal metal and a superconductor at T=0 K. An excitation of energy ε_{k_1} can tunnel from k_1 either in k_2 or k_2 (Fig.I.8a,b respectively). A hole is left behind in k_1 giving an excitation energy $|\varepsilon_{k_1}|$. The quasi-particle in k_2' gives rise to an excitation energy $E_{k_2}' = [\Delta^2 + (\varepsilon_{k_2}')^2]^{\frac{1}{2}}$. The probability that the initial state

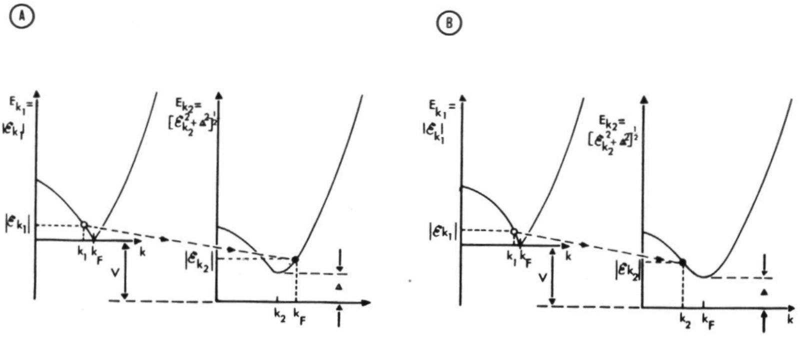

Fig.I.8 Tunneling between a normal metal and a superconductor. (A) The final state of the electron in the superconductor is $k_2' > k_F$. (B) The final state of the electron in the superconductor is $k_2 < k_F$.

$(k_2', -k_2')$ is empty is $(u_{k_2}')^2$, hence the transfer process is proportional to $(u_{k_2}')^2$. Energy is conserved when $|\varepsilon_{k_1}| + |E_{k_2}'| = V$. Because the electron can tunnel either in k_2 or k_2' the total probability of the transfer is proportional to $(u_{k_2})^2 + (u_{k_2}')^2$. As $\varepsilon_{k_2} = -\varepsilon_{k_2}'$, the sum of the coherence factors will give unity (cf.(I.20)).

For two superconductors (Fig.I.9a,b) the tunneling process will

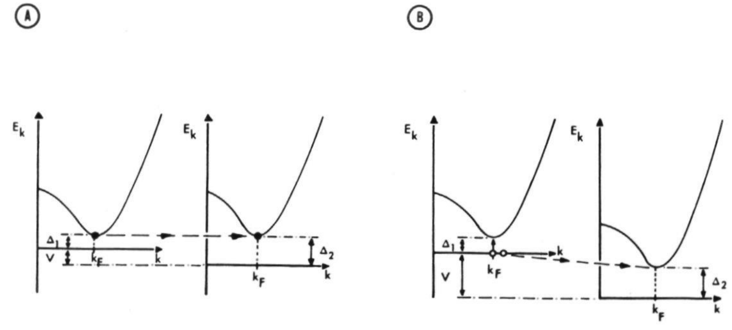

Fig.I.9 Tunneling between two different superconductors. (A) For a bias voltage $V = \Delta_2 - \Delta_1$. (B) For a bias voltage $V = \Delta_2 + \Delta_1$.

occur by first breaking a Cooper pair (located at zero excitation energy), one of the electrons becomes part of the normal fluid in S_1 and the other tunnels across. Again in this process energy is conserved.

The representation in E_k-k diagrams certainly depicts the real physical situation more correctly, but it is very complicated because both branches of the diagram need to be taken into account.

In this thesis we will use the semiconductor representation unless it causes misunderstanding.

I.3 Specific cases

I.3.1 The superconductor-insulator-normal metal(SN) junctions

We wish to evaluate numerically formulas derived in the previous paragraphs in order to be able to extract data such as $\Delta(T=0)$ from the measured curves in an unambigously way. First a few remarks should be made. The BCS theory is in essence a theory for 'bulk' material. As we are dealing with thin films with thicknesses of ≈2000 Å, one may ask if this will not lead to size effects in the superconducting parameters like $\Delta(T=0)$, T_c etc. However, as Anderson has shown in his theory (47) of dirty superconductors, the BCS theory is remarkable insensitive to various imperfections (with the exception of magnetic impurities), e.g. thickness, and in the dirty case, everything is isotropic.

There exist still some features which may affect the ideal behaviour. We mention just a few:

(i) Strain. If the substrate, on top of which the superconducting film is evaporated, is not uniform, it may cause strain in the evaporated films which leads to a smearing out of the gap.

(ii) Leakage currents. If the oxide layer is penetrated by metallic bridges ('pin-holes'), the tunnel junctions will be shorted via bridges and will carry a great deal of the current.

(iii) Edge effects. Due to the non-sharpness of the film edges, the parts of the film near the edge may have other properties then the bulk material (48).

(iv) Magnetic flux. Once a field has been applied, magnetic flux may be trapped in the film, causing normal regions in the films.

(v) Measuring current. If the current becomes too high, there will be Joule heating and the film may get normal regions. This effect is important for low impedance (mΩ) junctions where the current necessary to investigate structurs outside the gap region can be quite high (≈1A). Apart from the trivial heating-effect the gap may also depend on the transport current (49).

From (I.10) and (I.12) we have for a SN junction

$$I_{SN} = C_{NN} \int_{-\infty}^{+\infty} |E| / (E^2 - \Delta^2)^{\frac{1}{2}} \{f(E) - f(E+V)\} dE \qquad (I.32)$$

We have seen that for T=0

$$I_{SN} = 0 \qquad\qquad 0 \leqslant V < \Delta$$

$$I_{SN}(V) = C_{NN}(V^2 - \Delta^2)^{\frac{1}{2}} = I_{SN}(-V) \qquad V > \Delta \qquad (I.14)$$

$$dI_{SN}/dV = C_{NN} n_S(V). \qquad (I.15)$$

For T≠0 the solution of (I.32) can not be expressed in a closed form, but it is possible to compute the integral in the form of a series which converges rapidly for some limiting cases. One gets

$$I_{SN} = C_{NN}\Big[\int_{\Delta}^{\infty} dE(E)/(E^2 - \Delta^2)^{\frac{1}{2}}\{f(E)-f(E+V)\}+$$

$$+\int_{-\infty}^{-\Delta} dE(-E)/(E^2 - \Delta^2)^{\frac{1}{2}}\{f(E+V)\}\Big]$$

$$= \int_{\Delta}^{\infty} dE(E)/(E^2 - \Delta^2)^{\frac{1}{2}}\{f(E-V)-f(E+V)\},$$

using f(a)=1-f(-a). Introducing $x=E-\Delta$, one finds

$$I_{SN} = \int_0^{\infty} (x+\Delta)/[x(x+2\Delta)]^{\frac{1}{2}}\{f(x+\Delta-V)-f(x+\Delta+V)\}$$

Expanding the Fermi function f(a) (valid for a>0)

$$f(a) = \exp(-a)[1+\exp(-a)]^{-1} = \exp(-a)\sum_{m=D}^{\infty} \frac{(-1)^m}{m!}\exp(-ma)$$

we get after substituting for a: $x+\Delta\pm V=a$

$$I_{SN} = 2\sum_{m=0}^{\infty}(-1)^{m+1}\exp(-\frac{m\Delta}{kT})\sinh\frac{mV}{kT}\int_0^{\infty}\frac{x+\Delta}{[x(x+2\Delta)]^{\frac{1}{2}}}\exp(-\frac{mx}{kT})dx,$$

with the constraint that V<Δ. This integral is tabulated among the known Laplace transforms namely (50):

$$\int_0^{\infty}\frac{t+\alpha}{[t(t+2\alpha)]^{\frac{1}{2}}} e^{-pt}dt = \alpha\exp(p\alpha)K_1(mp\alpha),$$

where K_1 is the first order Bessel function of the second kind. Therefore, one finally has

$$I_{SN} = 2C_{NN}\,\Delta\sum_{m=0}^{\infty}(-1)^{m+1}K_1(\frac{m\Delta}{kT})\sinh(\frac{mV}{kT}). \qquad (I.33)$$

For V→0 this reduces to

$$\lim_{V\to 0} I_{SN} = 2C_{NN}\frac{V\Delta}{kT}\sum_{m=0}^{\infty}(-1)^{m+1}\, mK_1(\frac{m\Delta}{kT}).$$

If in addition T→0, we may use the asymptotic form of the Bessel function (51)

$$K_1(\alpha) \cong \left(\frac{\pi}{2\alpha}\right)^{\frac{1}{2}}\exp(-\alpha),$$

and finds, neglecting terms with $m > 1$,

$$\lim_{V,T\to 0} \frac{I_{SN}}{I_{NN}} = \left(\frac{2\pi\Delta}{kT}\right)^{\frac{1}{2}}\exp\left(\frac{-\Delta}{kT}\right) = F(T,\Delta(T)). \qquad (I.34),$$

This formula (which is of the same form as the one for the specific heat of a superconductor) gives an easy way to measure $\Delta(T)$. In the next section I.4 we will show explicit computer calculations for the current-voltage curves, which of course are not restricted to certain temperature or voltage ranges.

I.3.2 The superconductor-insulator-superconductor(SS) junctions

For the SS case, we have from (I.16) (I.35)

$$I_{SS} = C_{NN}\int_{-\infty}^{+\infty} dE\,|E-V|\,|E|\,/[(E-V)^2-\Delta_1{}^2]^{\frac{1}{2}}[E^2-\Delta_2{}^2]^{\frac{1}{2}}\{f(E-V)-f(E)\}.$$

In our experiment we are only dealing with junctions consisting of identical superconductors, i.e. $\Delta_1=\Delta_2$.

If we look again first at the formulas for T=0 K, the difference of the Fermi functions is

$$\begin{aligned} f(E-V)-f(E) &= 1 \qquad && 0 < E < V \\ &= 0 \qquad && E < 0,\ E > V. \end{aligned}$$

The limits of integration extend from Δ at the top of the gap at the right, to $V-\Delta$ at the bottom at the left, thus

$$\begin{aligned} I_{SS} &= 0 \qquad && V < 2\Delta \qquad && V < 2\Delta \\ I_{SS} &= C_{NN}\int_{\Delta}^{V-\Delta} dE\;E(V-E)/[(E-V)^2-\Delta^2]^{\frac{1}{2}}[E^2-\Delta^2]^{\frac{1}{2}} && && V \geqslant 2\Delta. \end{aligned}$$

Introducing $t = \frac{E-V/2}{\Delta-V/2}$,

$$I_{SS} = C_{NN}\int_{-1}^{1} dt[(V/2)^2-t^2(\Delta-V/2)^2]/(\Delta+V/2)(t^2-1)^{\frac{1}{2}}(\alpha^2t^2-1).$$

This expression can be written as a linear combination of the complete elliptic integrals (51) of the first and second kind respectively:

$$K(\alpha) = \int_0^1 dt(1-t^2)^{-\frac{1}{2}}(1-\alpha^2 t^2)^{-\frac{1}{2}}$$

$$E(\alpha) = \int_0^1 dt(1-\alpha^2 t^2)^{-\frac{1}{2}},$$

in the form(52)

$$I_{SS} = C_{NN}\{(2\Delta+V)E(\alpha)-4[\Delta(\Delta+V)/(2\Delta+V)]K(\alpha)\}, \qquad (I.36)$$

where $\alpha=(V-2\Delta)/(V+2\Delta)$. It should be noted that for $V\rightarrow 2\Delta$ (I.36) reduces to a finite value, that is, due to the singularity in the density of states at Δ, there is a discontinuity in the current. Because of (51)

$$\lim_{\alpha\rightarrow 0} K(\alpha) = \lim_{\alpha\rightarrow 0} E(\alpha) = \frac{\pi}{2},$$

this value of the current becomes

$$I_{SS}(T = 0, V = 2\Delta) = C_{NN}\frac{\pi}{2}\Delta = I_{NN}\frac{\pi}{4} \qquad (I.37)$$

This simple formula gives a good way to determine the value of the gap for a SS junction (53). For $T\neq 0$, one gets numerically for $V<2\Delta$, $\Delta\gg kT$

$$I_{SS} = (\Delta_1 = \Delta_2 \gg kT) \approx 2C_{NN}\exp(-\Delta/kT)[2\Delta/(V+2\Delta)]^{\frac{1}{2}}(V+\Delta)x$$
$$x \sinh(V/2kT)K_0(V/2kT),$$

where K_0 is a modified Bessel function of the second kind, (I.38) exhibits a slight negative region for $kT \lesssim 0.3\Delta$. This case will be treated in more detail in I.4.

I.4 Computer evaluation

I.4.1 SN case

As we have seen in the foregoing paragraph, it is possible to obtain analytic expressions for the tunneling current as a function of voltage, temperature and $\Delta(T)$ in certain limiting cases, e.g. $\Delta \gg kT$ etc. However, for practical purposes it is most useful to evaluate numerically the integral expressions for the tunneling current over the whole region. As before, we have

$$I_{SN} = C_{NN} \int_{\Delta}^{\infty} dE\ (E)/(E^2 - \Delta^2)^{\frac{1}{2}}\ \{f(E-V)-f(E+V)\}$$

In order to make all variables dimensionless, we choose new parameters as following:

(i) the temperature T is replaced by the reduced temperature $t=T/T_c$, T_c being the critical temperature.

(ii) $\Delta(T)$ is replaced by $\Delta(T)/\Delta(T=0)$.

(iii) eV, the bias voltage times the electronic charge is replaced by $U=V/\Delta(T)$.

(iv) a new integration parameter is chosen as $\phi = \mathrm{arctg}\ (e/E)$ where $\varepsilon=(E^2-\Delta^2)^{\frac{1}{2}}$

According to (iv) we have after some calculation

$$\varepsilon = \Delta \mathrm{tg}\phi/(1-\mathrm{tg}^2\phi)^{\frac{1}{2}}$$

Hence $dE(E/\varepsilon) = d\phi[-\Delta(T)(1-\mathrm{tg}^2\phi)^{\frac{1}{2}}]/(1-t^2\phi)^2\cos^2\phi$

Substituting $p=\mathrm{tg}\phi$, one gets

$$dE\ E/(E^2-\Delta^2)^{\frac{1}{2}} = dp\Delta(T)/(1-p^2)^{\frac{3}{2}}$$

From (I.32) we then obtain:

$$I_{SN} = C_{NN} \int_0^1 dp\Delta(T)/(1-p^2)^{\frac{3}{2}} \{f[c(1/(1-p^2)^{\frac{1}{2}}-U)] - $$
$$ - f[c(1/(1-p^2)^{\frac{1}{2}}+U)]\}, \qquad (I.39)$$

with $C=\Delta(T)/kT$. To use the reduced temperature t we make use of the calculations of Mühlschlegel (54). He calculated numerically $\Delta(T)/\Delta(0)$ as a function of $t=T/T_c$. In addition we need a relation between $\Delta(0)$ and T_c. For a weak coupling superconductor, we have according to BCS:

$$2\Delta(0) = 3.52kT_c$$

It is well known that this relation is accurate to at least 1% for aluminium (55). For other superconductors we may have to use instead of 3.52 another factor (e.g. in the case of lead, a strong coupling superconductor, one has $2\Delta(0)=4.3kTc$). For our case of aluminium we thus have

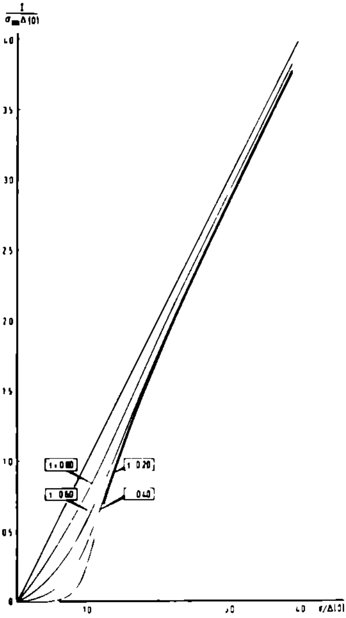

Fig.I.10 Theoretical curves of the current (I) versus voltage (V) of a SN junction for several temperatures $t = T/T_c$, as predicted by the BCS theory. The current and voltages are plotted on reduced (dimensionless) scales. σ_{NN} is the conductance of the junction for temperatures $T > T_c$.

$$c = \frac{\Delta(T)}{kT} = \frac{kT_c}{kT}\,\frac{\Delta(0)}{kT_c}\,\frac{\Delta(T)}{\Delta(0)} = 1.76\,\frac{W(t)}{t}$$

and

$$U = \frac{V}{\Delta(T)} = \frac{\Delta(0)\,V}{\Delta(0)\Delta(T)} = \frac{V}{\Delta(0)}\,W(t),$$

where W(t) is the array of the Mühschlegel numbers (54), which we will need in the computer programme. So (I.39) becomes:

$$I_{SN} = c_{NN}\Delta(0)\int_0^1 dp\; W(t)/(1-p^2)^{\frac{3}{2}}\{f[1.76t^{-1}\left(W(t)/(1-p^2)^{\frac{1}{2}}-V/\Delta(0)\right)] - f[1.76t^{-1}\left(W(t)/(1-p^2)^{\frac{1}{2}}+V/\Delta(0)\right)]\} \qquad (I.40)$$

We refer to the Appendix for the computer programme used to generate the curves shown in Fig.I.10.

Usually, the derivative of the current with respect to voltage is measured by means of a suitable AC modulation technique. In order to compare these curves with theory, we consider the derivative of (I.40) with respect to voltage. We obtain, with

$$\frac{d}{dx}\,f(x) = f(x)[\,f(x)-1]$$

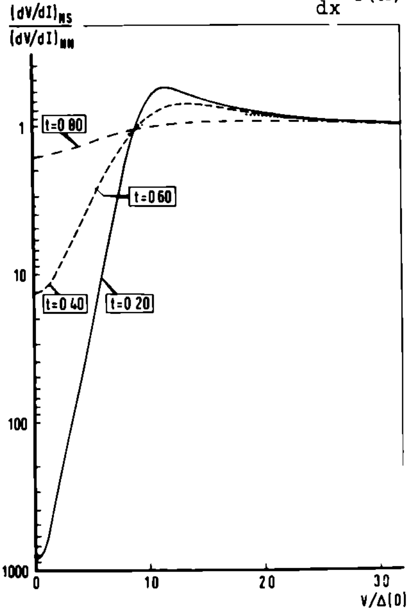

Fig.I.11 Calculated normalized dynamic resistance versus reduced voltage diagram of a SN junction, for different temperatures $t = T/T_c$

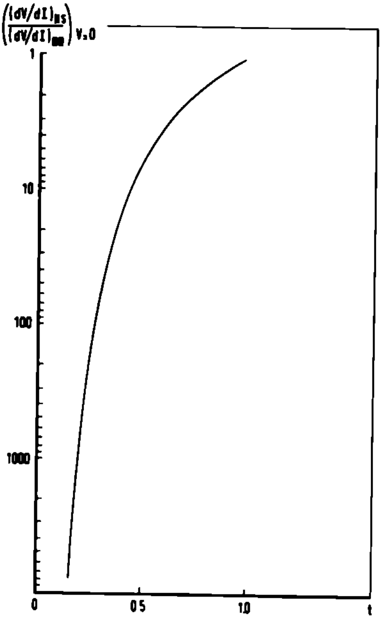

Fig.I.12 The normalized dynamic resistance at zero bias voltage versus $t = T/T_c$ for a SN junction. Note the strong temperature dependence.

$$\frac{d}{dV} I_{SN} = -c_{NN} 1.76 t^{-1} \int_0^1 dp\, W(t)/(1-p^2)^{\frac{3}{2}} \{F^-(F^- -1) + F^+(F^+ -1)\} \tag{I.41}$$

where: $F^{\pm} = f[1.76t^{-1} \left(W(t)/(1-p^2)^{\frac{1}{2}} \pm V/\Delta(0)\right)]$

A set of these curves for the same temperatures as in Fig.I.10 is plotted in Fig.I.11. On this scale it seems that all curves cross in one point, however this is not the case. To get an idea of the sensitivity of (I.41) as a function of temperature we also plot the derivative at V=0. We get

$$\left(\frac{d}{dV} I_{SN}\right)_{V=0} = -3.52\, c_{NN} t^{-1} \int_0^1 dp\, W(t)/(1-p^2)^{\frac{3}{2}} \times$$
$$\times\{[f(1.76t^{-1}W(t)/(1-p^2)^{\frac{1}{2}}]\ [f\left(1.76\, t^{-1}W(t)/(1-p^2)^{\frac{1}{2}}\right)-1]\} \tag{I.42}$$

If we plot this expression in Fig.I.12, we see that the normalized conductance changes by a factor of as much as 10^7 when the temperature has a range from T_c to $0.1T_c$. It is interesting for a check to compare the results from (I.42) with the approximate formula (I.33), which is only valid for $V>\Delta(T)$. We have from (I.33)

$$\left(\frac{d}{dV} I_{SN}\right)_{V=0} = 3.52\, c_{NN} \frac{W(t)}{t} \sum_{m=0}^{\infty} (-1)^{m+1} m K_1\left(m 1.76 \frac{W(t)}{t}\right) \qquad \text{(I.43)}$$

In the Appendix both programmes used to compute (I.41), (I.42) and (I.43) are given. The last two give identical results within 0.1%.

I.4.2 SS case

We will follow the same procedure as in I.4.1. We have from (I.35):

$$I_{SS} = c_{NN} \int_{-\infty}^{+\infty} dE_1 [\,|E_1|\,|E_2| / (E_1^2-\Delta_1^2)^{\frac{1}{2}}]\,\{f(E_1)-f(E_2)\}.$$

where $E_2=E_1+V$. Let us restrict ourselves to identical superconductors: $\Delta_1=\Delta_2$.

Again we will make all variables dimensionless in order to facilitate numerical integration. In addition to (i) and (ii) (cf. I.4.1), we have

(iii) V is replaced by $U=V/2\Delta(T)$.

(iv) a new integration parameter will be defined by $x=(\varepsilon_2-\varepsilon_1)/(E_2-E_1)$. Then

$$\varepsilon_1 = \Delta(q-Ux) \text{ and } \varepsilon_2 = \Delta(q+Ux),$$

where $q=[U^2+1/(x^2-1)]^{\frac{1}{2}}$. It follows that

$$E_1 = \Delta(xq-U) \text{ and } E_2 = \Delta(xq+U).$$

According to (56) these new parameters avoid singularities in the integrand. From $E=(E^2+\Delta^2)^{\frac{1}{2}}$ and $E_2=E_1+V$ it follows that

$$\frac{dx}{dE_1}=\frac{1}{V}\left\{\left(\frac{E_2}{\varepsilon_2}\right)-\left(\frac{E_1}{\varepsilon_1}\right)\right\}$$

or $\quad dE_1 = dx\ \varepsilon_1\varepsilon_2 V/E_2\varepsilon_1-E_1\varepsilon_2$

Hence the two root singularities cancel in the integrand. The new boundaries of the integration are given by Fig.I.13. We see that for $V<2\Delta$, x will vary between $(1+1/U)^{\frac{1}{2}}$ (corresponding to $E_1=\Delta$) and 1 (corresponding to $E_1\to\infty$). Hence the integral (I.35) becomes for bias voltage lower than 2Δ:

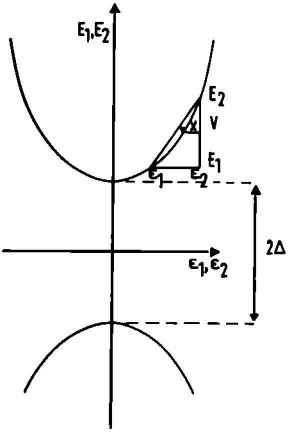

Fig.I.13 E_1, E_2 versus ε_1, ε_2 diagrams for a SS junction with $E_2 = E_1+V$ and $E_i = (\varepsilon_i^2+\Delta^2)^{\frac{1}{2}}$, i = 1,2.

$$I_{SS} = c_{NN}\int_{(1+1/u)^{\frac{1}{2}}}^{1} dx\,\frac{\Delta}{(1-x^2)}\left(x^2q^2-\frac{U^2}{q}\right)\{f[c(qx-U)]-f[c(qx+U)]\} \tag{I.44}$$

Because we use only the temperature dependance of the current-voltage for bias voltages lower than 2Δ this is sufficient for our purposes to evaluate (I.44).

Some current-voltage characteristics are shown in Fig.I.14. One recognises the steep portion of the curve for $V\lesssim kT$ or $cU=\frac{1}{2}$, which reflects the two BCS singularities in the density of states. It is easily seen from a Taylor expansion of the difference of the two Fermi functions that higher order terms may not be excluded when $\beta V\approx 1$. The negative resistance region is recognizable below $t\lesssim 0.40$ which is consistent with the result of I.3.2. Finally, in Fig.I.15 the calculated temperature dependence of the current for a fixed bias voltage is plotted.

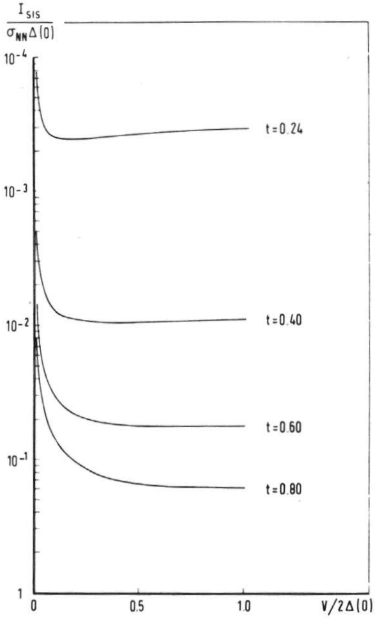

Fig.I.14 Theoretical curves of the current (I) versus voltage (V) of a SS junction for several temperatures $t = T/T_c$ for bias voltages smaller than 2Δ.

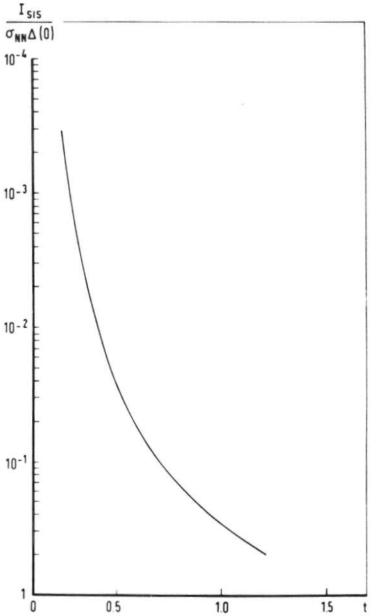

Fig.I.15 Temperature dependence of the mid-gap current $[I(V = \Delta(0))]$ for a SS junction.

In Chapter II we will see how actual SS junctions do not obey the predicted behaviour due to DPT (double particle tunneling) processes ((40), (41), (42),(57)) and because the two gaps of the two 'identical' superconductors are not strictly equal.

References

1 H. Kamerlingh Onnes, Comm. Leiden 122b, 124c (1911).

2 W. Meissner and R. Ochsenfeld, Naturwissenschaften 21, 787 (1933).

3 C.J. Gorter and H.B.G. Casimir, Phys. Z. 35, 963 (1934).

4 F. London and H. London, Proc. Soc. A 149, 71 (1935).

5 V.L. Ginzburg and L.D. Landau, Zh. Eksp. Teor. Fiz. 20, 1064 (1950).

6 A.B. Pippard, Proc. Roy. Soc. A 216, 547 (1953).

7 C.A. Reynolds, B. Serin, W.H. Wright and L.B. Nesbitt, Phys. Rev. 78, 487 (1950).
E. Maxwell, Phys. Rev. 78, 477 (1950).
H. Fröhlich, Phys. Rev. 79, 845 (1950).

8 J. Bardeen, L.N. Cooper and J.R. Schrieffer, Phys. Rev. 108, 1175 (1957).

9 L.N. Cooper, Phys. Rev. 104, 1189 (1956).

10 A. Brown, M. Zemansky and H.F. Boorse, Phys. Rev. 92, 52 (1953).

11 B.B. Goodman, Proc. Phys. Soc. (London) A66, 217 (1953).

12 R. Glover and M. Tinkham, Phys. Rev. 108, 243 (1957).

13 P.L. Richards and M. Tinkham, Phys. Rev. Letters 1, 318 (1958).

14 I. Giaever, Proc. VIIth Int. Conf. Low Temp. Phys., Toronto 1960 (University of Toronto Press, 1961), p.327.

15 W.L. McMillan and J.M. Rowell, Phys. Rev. Letters 14, 108 (1965).

16 I. Giaever and K. Megerle, Phys. Rev. 122, 110 (1961).

17 D.H. Douglass, Phys. Rev. Letters 7, 14 (1961).

18 J.L. Levine, Phys. Rev. Letters 15, 154 (1964).

19 N.V. Zavaritskii, JETP 16, 793 (1964).

20 F. Reif and M.A. Woolf, Phys. Rev. Letters 9, 315 (1962).

21 J. Millstein and M. Tinkham, Phys. Rev. 158, 325 (1967).

22 P.H. Smith, S. Shapiro, J.L. Miles and J. Nicol, Phys. Rev. Letters 6, 686 (1961).

23 J.J. Hauser, Phys. Rev. 164, 558 (1967).

24 D.M. Ginsburg, Phys. Rev. Letters 8, 204 (1962).

25 B.I. Miller and A.H. Dayem, Phys. Rev. Letters 18, 1000 (1967).

26 B.N. Taylor, J. Appl. Phys. 39, 2490 (1968).

27 A. Sommerfeld and H. Bethe, in 'Handbuch der Physik' Vol. XXIV, Part 2 (Julius Sprenger, Berlin 1933), p. 333.

28 R. Holm, J.Appl.Phys. 22, 569 (1951).

29 L. Esaki, Phys. Rev. 109, 603 (1958).

30 I. Giaever, H.R. Hart and K. Megerle, Phys. Rev. 126, 941 (1962).

31 B.D. Josephson, Adv. Phys. 14, 419 (1965).

32 J. Bardeen, Phys. Rev. Letters 6, 57 (1961).

33 M.H. Cohen, L.M. Falicov and J.C. Phillips, Phys. Rev. Letters 8, 316 (1962); Proc. VIIIth Int. Conf. Low Temp. Phys. 1962, (Butterworths, London, 1963), p. 178.

34 J. Bardeen, Phys. Rev. Letters 9, 147 (1962).

35 R.E. Prange, Phys. Rev. 131, 1083 (1963).

36 W.A. Harrison, Phys. Rev. 123, 85 (1961).

37 L. Schiff, in 'Quantum Mechanics' (Mc.Graw-Hill, New York, 1955), p. 92.

38 N.N. Bogoliubov, Nuovo Cimento 7, 794 (1958).
J.G. Valatin, Nuovo Cimento 7, 843 (1958).

39 B.D. Josephson, Physics Letters 1, 251 (1962).

40 B.N. Taylor and E. Burstein, Phys. Rev. Letters 10, 14 (1963).

41 C.J. Adkins, Phil. Mag. 8, 1051 (1963).

42 J.R. Schrieffer and J.W. Wilkins, Phys. Rev. Letters 10, 17 (1963).

43 L.D. Landau, JETP 5, 71 (1941), JETP 11, 91 (1947).

44 W.J. Tomasch, Phys. Rev. Letters 15, 672 (1965).

45 J.R. Schrieffer, in 'Tunneling Phenomena in Solids' (Plenum Press, New York, 1969), p. 289.

46 J.R. Schrieffer, D.J. Scalapino and J.W. Wilkins, Phys. Rev. Letters 10, 336 (1963). J.R. Schrieffer, in 'Theory of Superconductivity' (Benjamin, New York, 1964), p. 78.

47 P.W. Anderson, Phys. Chem. Solids 11, 26 (1959).

48 A.P. van Gelder, J.W. Hendriks and P. Wyder, Phys. Rev. B 4, 2950 (1971).

49 J.L. Levine, Phys. Rev. Letters 15, 154 (1965).

50 A. Erdélyi, 'Table of Integral Forms' Vol.I (McGraw-Hill, New York, 1954), p. 136.

51 Jahnke-Emde-Lösch, 'Tables of Higher Functions' (McGraw-Hill, New York, 1960).

52 I. Giaever, H.R. Hart and K. Megerle, Phys. Rev. 126, 941 (1962).

53 W.L. McMillan and J.W. Rowell, in 'Treatise on Superconductivity' Ch. 11 (Dekker, New York, 1969), p. 561. J.W. Rowell, in 'Tunneling Phenomena in Solids' (Benjamin, New York, 1969), p. 281.

54 B. Mühlschlegel, Z. Physik, 155, 313 (1959).

55 B.L. Blackford and R.H. March, Can. J. Phys. 46, 141 (1968).

56 A.P. van Gelder, Physica 55, 643 (1971).

57 L. Kleinman, B.N. Taylor and E. Burstein, Rev. Mod. Phys. 36, 208 (1964).

CHAPTER II APPLICATION TO THERMOMETRY - AN ABSOLUTE THERMOMETER IN THE 0.12 - 1.2 K RANGE

II.1 Outline of the experiment

It is one of the greater problems of low temperature physics to have primary thermometers for the temperature range below 1 K. For temperatures below the boiling point of liquid He^4, one often makes use of the vapour pressure of liquid He^4; experimentally, this spans the region between atmospheric pressure, corresponding to 4.2 K, and in the best case 0.4 mm Hg, corresponding to 1 K. Below 1 K, one usually uses the susceptibility of a paramagnetic salt, assuming that this salt obeys a Curie-Weiss law to a sufficient degree of accuracy. The most well-known and the most used of these salts is ceriummagnesiumnitrate (CMN). One usually writes for the susceptibility χ

$$\chi = c/T^{\star} \qquad \text{(II.1)}$$

For CMN $T^{\star}(T) = T$ above 0.1 K.

However, such a thermometer has to be calibrated for each experiment in the 4 - 1 K range against the vapour pressure of liquid He^4, in order to get the constant C. In addition, this thermometer has a large heat capacity, and therefore responds slowly to temperature changes. Moreover, as the heat capacity of the salt increases at lower temperatures while contact resistances (via glue, grease etc.) and spin-lattice relaxation time increase as well, the response time τ becomes very large at ultra-low temperatures. For instance one gets approximately for a single crystal CMN due to the long spin-lattice relaxation time

$$\tau_R \cong 100 \text{ sec. at } T = 0.1 \text{ K.}$$

As was pointed out in Chapter I, the expressions for the tunneling current through a superconducting tunnel junction are strongly temperature dependent via the Fermi factors which appear in the integrand. Therefore, tunnel junctions can be used as thermometers. As a thermometer, the superconducting tunnel junction has some important advantages. Thermal contacts between metal films and substrates are usually very good and the heat capacity of a 1 mm^2 junction is of the order of 10^{-10} J/K at 1 K which is extremely small. Hence the response time is orders of magnitude smaller than with the CMN thermometer, e.g.

$$\tau_R \cong 10^{-6} \text{ sec. at } T = 1 \text{ K}$$

$$\tau_R \cong 10^{-4} \text{ sec. at } T = 0.1 \text{ K.}$$

But of course the nicest feature of a junction thermometer is that it does not need any calibration against any primary thermometer.

The subject of this chapter is to describe to which degree of accuracy such a 'BCS-thermometer' can be used and in which temperature range it is most useful. Obviously, this range is limited because of the critical temperature T_c. But by using different superconductors with different T_c's, it should be possible to span the region from 20 K to 10^{-3} K with such a BCS-thermometer. For our experiments in a sort of feasibility study, we used Al ($T_c \approx 1.2$ K) which should be able to span the region from

0.12 K to 1.2 K. In order to enable comparison, we also used carbon-resistance thermometers, calibrated in the conventional way against CMN. These thermometers are mounted onto a ruby sample on which also the aluminium junction is deposited. The ruby, which contains paramagnetic Cr^{3+}-ions is used as a good thermal contact and as a cooling agent at the same time. By adiabatic demagnetization (1) the ruby was cooled down from 1.2 K to 0.08 K.

II.2 The use of ruby as a cooling agent

Chromium corundum, commonly called ruby, has a rhombohedral structure in which all Cr and Al atoms are at equivalent sites whose symmetry is trigonal; thus the crystalline field acting on the Cr^{3+}-ions has a trigonal symmetry around the crystalline c-axis. Therefore, the free Cr^{3+}-ion in a $^4F_{3/2}$ state is under the influence of a trigonal field. It has been pointed out (2) that due to spin-orbit coupling the lowest levels are spin doublets with quantum numbers ±3/2 and ±1/2, of which the ±3/2 level lies lowest.

Using a spin Hamiltonian for the $Cr^{3+}(S = 3/2)$ ion, it is possible (4) to calculate the partition function and therefore the susceptibility. It is possible to express the χ as a function of T in terms of a power series. For temperatures $T \gg \Delta$, where Δ is the zero-field splitting between the two spin doublets, it is possible to write χ in the form

$$\chi = c/(T-\Theta) \qquad \text{(II.2)}$$

where Θ is the Curie-Weiss constant, which can be calculated from (2). This well known standard procedure ignores the interactions between neighbouring Cr^{3+} spins, for example dipole-dipole interactions and antiferromagnetic exchange coupling(3). Hence, even the relation (III.2) may not hold above 1 K. It is difficult to calculate the influence of these interaction on the χ versus T relation. Also, because of these interactions,it is hard to predict the lowest temperature one can reach after demagnetization of a ruby with a given Cr^{3+}-ion concentration (4) (cf. Fig.II.1).

Despite the complicated behaviour of the susceptibility as a function of T, the relation $\chi(T)$ for ruby can be used as a thermometer, because the crystal is very stable; it is not hygroscopic like most of the commonly used paramagnetic cooling salts. In addition, for our experiments ruby has the important advantage that it can be polished to a very high degree (optical roughness of ~ 0.1 micron) so metal films can be deposited directly onto the ruby. Ruby has a high thermal conductivity which assures a good thermal equilibrium between evaporated films, the ruby and a resistance thermometer glued onto the ruby.

In our experiments (cf. II.5) we had at our disposal three rubies of Cr^{3+} content 0.01, 0.3 and 2%(atomic percentage), purchased from the Djéva Company (5). The different concentrations enables us to vary the heat capacity of the crystals. The lower the Cr^{3+} concentration, the lower the influence of the interaction amongst the Cr^{3+} spins which will lead to a lower final temperature, but also to a smaller heat capacity. The lowest temperature

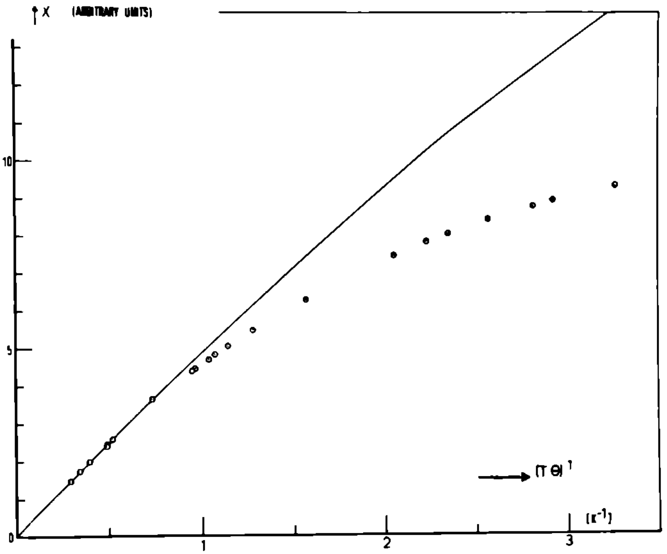

Fig.II.1 The deviation of the experimental points (⊚) from the theoretical susceptibility χ of ruby with 0.3Cr% (Ref. (2)). Interactions between Cr^{3+}-ions are not taken into account. χ obeys the Curie-Weiss relation (II.2) above 1 K.

attainable with the ruby of 0.3% is 80 mK, after demagnetizing from 12 kG. In principle it is possible to reach lower temperatures with a ruby of 0.01 Cr% content and with higher magnetizing fields, but the practical limit in our experiment is set by the reproducibility at the CMN calibrated thermometer (cf. II.3) which prohibits reliable measurements below 0.1 K.

II.3 Calibration of carbon thermometers

The use of carbon composition resistors as secondary thermometers is well established in cryogenic research. (6), (7), (8), (9). Some of the advantages are:

- small physical size.
- quick response due to the low heat capacity.
- high sensitivity, defined by $\frac{T}{R}\frac{dR}{dT}$.
- rather insensitive to magnetic fields.
- low cost.

A serious disadvantage is the lack of a theoretical resistance-temperature relation, which can be used for extrapolation with sufficient accuracy. Hence the thermometer needs to be calibrated accurately. Unfortunately, carbon-resistance thermometers are not ideally reproducible, which means that they change their characteristic every time they are warmed up to room temperatures. However, by careful handling, this disadvantage can be minimized.

For our investigations we used a Speer 470 Ω, 0.5 Watt (grade 1002) resistor as carbon thermometer. In order to reduce the heat capacity and to facilitate the heat contact, the resistor was ground off and polished to about half its size so as to provide a half cylinder. The rectangular carbon core which is then seen is isolated from external influences by coating with GE varnish (10). The leads made of copper plated niobium-titanium wire (11) are soldered to the remaining portion of the original copper leads which are embedded in the carbon core (12). The new leads are thermally anchored to the top of the resistor, which serves also to relief the stress and helps to improve the reproducibility. The resulting resistance is 1120 Ω at 300 K. When the thermometer is glued on top of a ruby crystal with Apiezon N grease, the leads are also anchored to the ruby; however the main thermal impedance of the resistor in the 0.1 K range lies in the carbon core itself (13). In order to prevent any heating up of the thermometer above the temperature of its surroundings, the power dissipated in the resistor must be kept very small, typically in the order of $\cong 10^{-9}T^3$ watt (14), (15). To measure the resistance, AC bridge techniques are preferred to avoid thermal and other emf's. The bridge will be described in II.4.3.

One of the main problems is Joule heating due to pick up of various sources. RF voltages can be induced in the leads by radio transmitters in the 10^8Hz range. It is usually sufficient to shunt the thermometer with a capacitor as close as possible to the resistor. We used a silvered mica capacitance of 2700 pF on top of the vacuum can inside the He II bath. With such a capacitance it is advisable to run the bridge at a low frequency, i.e. 80 Hz. All leads are twisted and shielded outside the crystal to avoid pick up and ground loops.

To calibrate the thermometer we use the Curie-law susceptibility of cerium magnesium nitrate (CMN) (16). The CMN sample and the carbon resistor are placed at the same sample holder (see Fig. II.7(G), (H). When measuring the mutual inductance of the coil set around the CMN sample (and the carbon resistor) one must keep the AC current low in order to avoid Joule heating of the resistor by the generated AC magnetic field especially in the resistor leads). Therefore we also removed as for as possible the original resistor leads.

For the temperature calibration of the resistors, above 1 K, the vapour pressure of liquid He (T_{58} scale) (17) was used as a primary thermometer; below 1 K, we used the susceptibility χ of the CMN sample. A typical calibration curve of the mutual inductance (which is proportional to χ) against T^{-1} in the liquid He temperature range is shown in Fig.II.2; from the slope, the calibration constant c is determined. After the calibration, the CMN is adiabatically demagnetized. During the warming-up, the susceptibility and the resistance of the carbon thermometer are determined simultaneously; assuming the relation (II.1) for CMN (which is well established in this temperature region (16)) and using c, one gets experimentally R(T). A typical R-T curve is plotted on a log scale in Fig.II.3.

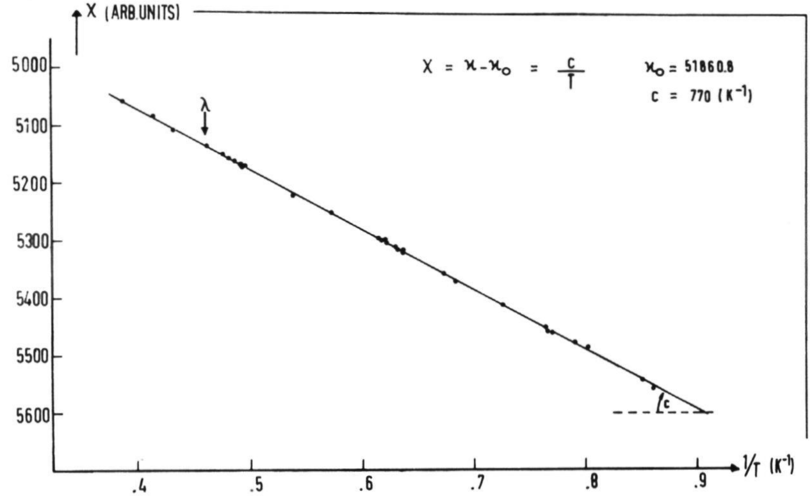

Fig.II.2 A calibration run of χ_{CMN} in arbitrary units against 1/T, where T is deduced from the vapour pressure of liquid He^4.

It is often useful to fit the data with an empirical formula (6), (18) of the form

$$T = \sum_{i=1}^{m-1} a_i \, (\log R)^{i-1} \qquad (II.3)$$

where m=4. The constants a_i are determined via a least mean square

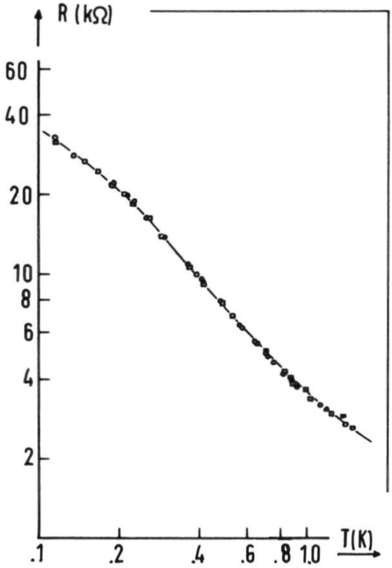

Fig.II.3 The calibrated Speer 470 Ω, 0.5 Watt resistor; 'O' corresponds to the first run. '□' is taken after recycling to room temperature.

fit. As shown in Fig.II.4, this fit is sufficient for interpolation purposes between calibration points. In the temperature range where the junction thermometer is being used (0.12-1.2 K), deviations from the calibration-formula are smaller than 0.2%. The reason for the large deviation below 0.1 K is partly due to the large scattering of the calibration points for the speer resistor, caused by bad heat contact or spurious heat leaks below 0.1 K.

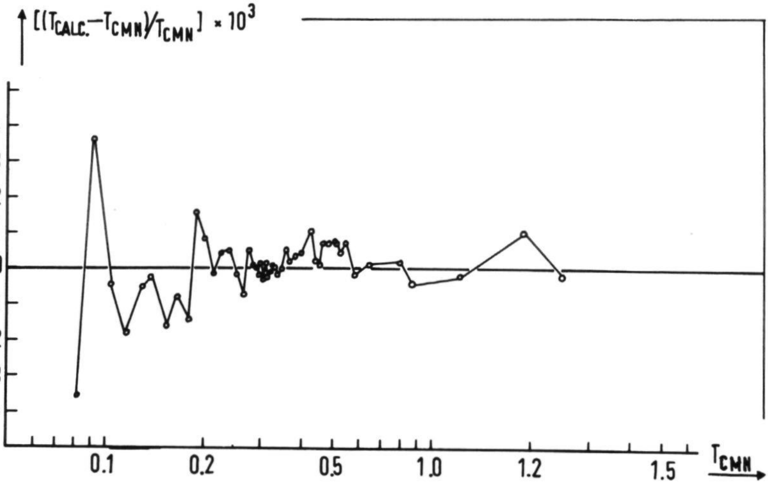

Fig.II.4 Deviation-plot between measured and calculated temperatures for a CMN-calibrated Speer resistor thermometer.

II.4 Experimental details

II.4.1 Preparation of junctions

As we have seen in Chapter I, a superconducting tunneling junction consists of two metals, separated by an insulating layer. In most cases, this insulating barrier consists of a natural grown oxide (of thickness ≅ 20Å) unfortunately this is however not always possible because not all metals oxidize very easily. Other possibilities are a very thin Al layer which is oxidized to completion (19) or evaporating some kind of organic layer like Formvar (20) or using Langmuir-films (21).

The geometry of a junction can also differ from experiment to

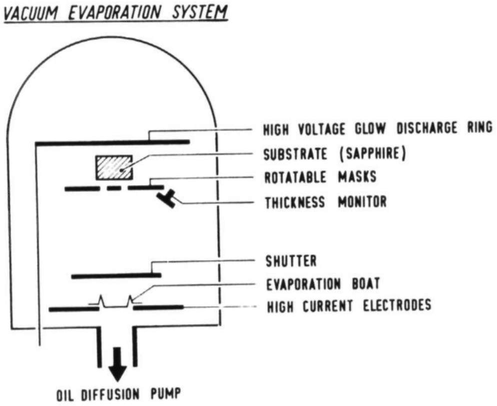

Fig.II.5 Vacuum chamber for evaporation. See text for further details.

experiment. The most established set-up is an arrangement of two thin strips of metal evaporated on top of each other separated by the barrier (22). But it is also possible to use point contacts (23), especially if one is interested in preparing Josephson type junctions. In most of our experiments we used a strip of aluminium of about 10 mm long, 1 mm wide and a few thousand Å thick.

The conventional evaporator consists basically of a vacuum chamber with a typical pressure of 5×10^{-6} mm Hg during evaporation (Fig.II.5). Contamination by diffusion pump oil is greatly reduced by a large liquid nitrogen trap. By passing a suitable current through a tungsten filament loaded with Al threads of high (99.9995%) purity (24), the material will melt and eventually evaporate (25), (26). When the evaporation rate is high enough - as measured by a quartz crystal monitor - a shutter between filament and substrate is removed and closed again when the film is thick enough. One then isolates the vacuum chamber from the pump and vent the system with laboratory air. This is sufficient to oxidize the Al film in a reproducible way. The oxidation time varies between 5 and 15 minutes and gives rise to a resistance of 10 to 100 Ω per mm^2 junction area. After the oxidation process, the junction is completed by changing masks and evaporating another film on top of the first one. (Fig.II.6).

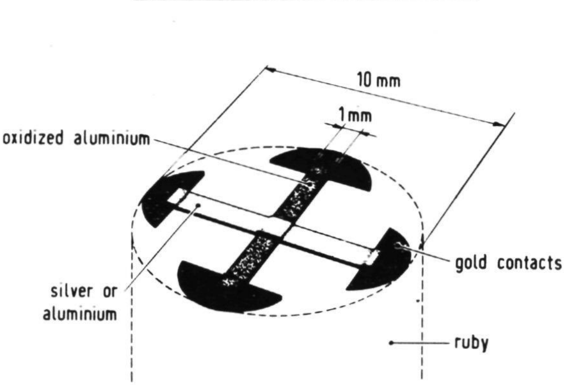

Fig.II.6 A completed junction on the top-face of a ruby crystal.

There are some important points with respect to the substrate which should be mentioned. Of course, the surface should be free of scratches, pits or foreign particles, and least optically polished (to a few 0.1 μ). In addition the substrate should be as clean as possible in the chemical sense, otherwise, the films will not stick and tend to peel off. Old metal films can easily be removed from the ruby with the help of a mixture of HCl and HNO_3 (3:1). The ruby is thereafter thoroughly rinsed with destilled water. To remove any grease, oil etc. the sample is treated in an Alconox solution(23), rinsed again with destilled water and pure alcohol or aceton. Then it is dried quickly with hot air to prevent drying marks. In the vacuum chamber itself follows an ionic glow discharge at a pressure of 100 micron Hg before evaporation. This procedure gives reasonable good cleaning qualities (26).

It is rather difficult to make electrical contacts to a film evaporated onto a ruby. On ordinary glass substrates it is possible to solder with In after evaporation, due to the low thermal conductivity of the glass, In the case of ruby (or sapphire, see Chapter III) one would have to heat the whole sample in order to be able to make contacts because of the high thermal conductivity. Some of contacts were made before evaporation (because otherwise the junction would be destroyed by the heating), others with mechanical contacts via miniature gold plated bellows (28). Both methods turned out to be reasonable safe. In the case of Al junctions, the sample has to be put into the vacuum system of the dewar as soon as possible (see II.4.2), otherwise the Al junction detoriates fairly fast because the junction impedance gets intolerably high. Our experience is that the lower the 'starting' impedance, the slower the increase in impedance. On the other hand, a fresh made junction of 1 k Ω can have an impedance of 100 k Ω in few hours.

II.4.2 Cryogenic part of the apparatus

The cryogenic part of the experiment consists of a simple standard adiabatic demagnetization set-up. One has a paramagnetic

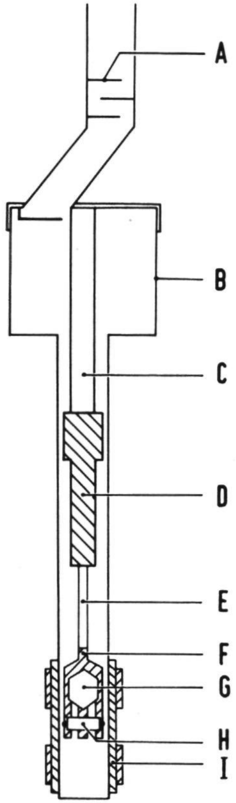

Fig.II.7 Vacuum can with sample holder for calibration of thermometers. (A) Heat shields (B) stainless steel can (C) nylon support (D) buffer salt pill (E) graphite rod (F) brass fork (G) CMN salt (H) resistance thermometer (I) mutual-inductance coil set.

sample, of which the heat contact with its surroundings can be broken in some way (e.g. exchange gas-vacuum), and an external magnetic field which serves to direct the spins, thus lowering the entropy of the system. This technique is reviewed extensively in the literature (1).

In Fig.II.7 a schematic drawing of the sample chamber is shown. In the version which was used to calibrate the carbon thermometer against CMN. This is essentially a vacuum can of thin walled stainless steel which can be pumped down to pressure $< 10^{-6}$ mm Hg by means of an oil diffusion pump with a liquid nitrogen trap. In the pumping line bellows are included to prevent heating by vibration and in the part of the line inside the dewar shields are mounted to prevent heating by room temperature radiation from above. The can and a large part of the pumping line is immersed in a 1.2 K He bath. The sample holder is a brass fork (to reduce eddy current heating), and the CMN plus thermometers are glued onto it with Apiezon N grease. The electrical leads of the thermometers are thermally anchored on the brass holder with GE varnish (10). The brass holder is screwed onto a graphite (29) rod, known for its very low thermal conductivity (30) especially in the lower temperature region below 1 K, whereas above this temperature it has higher than the commonly used nylon. This type of graphite is hard enough to be machined, although the threading suffers severely when used frequently. Between the graphite and the top of the can is a nylon support rod with a low thermal conductivity and a thermal guard, which again absorbs heat coming from above. The thermal guard is made of a mixture of small paramagnetic crystals ($\phi \approx 1\ mm^3$) of chromium potassium-alum (CrKA) and epoxy with a filling factor of about 70%. It is well known that most epoxys crack at low temperature; therefore we used a two-component-epoxy where one of the components remains elastic a little bit at He temperature (31). It can be applied for other low temperature applications as well (32). One has to let start the hardening process for about one hour and then add the paramagnetic salt, because otherwise crystal water is extracted from the CrKA and the hardening process stops. Thermal guards of this type can be machined very easily, and only the crystals at the immediate surface will detoriate after awhile if they remain at room temperature. The temperature of the guard is monitored by a carbon thermometer, and the leads coming from the brass sample holder are thermally anchored with Apiezon N grease, before going to the electrical feedthrough of the can. To measure the temperature of the CMN sample mutual inductance coils are wound onto the exterior of the lower end of the vacuum can. They consist of a primary coil and a balanced set of secondary coils wound in opposite directions. As the sample is positioned in one of the secondary coils, this arrangement measures the mutual inductance which is proportional to the sample susceptibility χ.

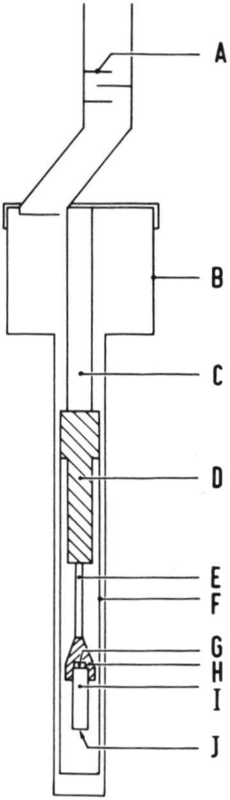

Fig.II.8 Vacuum can with sample holder for ruby demagnetization. (A) Heat shields (B) stainless steel can (C) nylon support rod (D) buffer salt pill (E) graphite rod (F) heat shields at buffer salt temperature (G) CMN calibrated thermometer (H) nylon holder (I) ruby crystal (J) evaporated tunnel junction.

The other version of the sample holder used for ruby-measurements is similar (Fig.II.8), the ruby being clamped in a nylon holder. On top of the ruby the CMN-calibrated thermometer is glued with Apiezon N grease and on the bottom the tunnel junction thermometer is evaporated. Due to the good thermal conductivity of ruby a good thermal equilibrium between the two thermometers is assured. A somewhat wider can in order to have an additional heat shield of copper connected to the thermal guard was used. The magnetic field was either a 12 kG conventional electromagnet with 12 inch polepieces, or a superconducting solenoid with a nominal field of 23 kG. The superconducting coil can be pulled upwards after demagnetization, thereby removing the remanent field from the paramagnetic samples.

II.4.3 Electronic circuitry

The electronic equipment consists mainly of three parts:

(i) The AC resistance bridge.

(ii) The mutual inductance bridge.

(iii) The tunneling apparatus.

(i) The AC bridge for monitoring the resistance thermometer or the zero bias resistance of a junction consists basically of a wheatstone bridge. A circuit diagram is shown in Fig.II.9. An oscillator of 80 Hz drives the bridge via an audio transformer (29). The two 10k Ω resistances are matched. In order to compensate for the varying capacitance of the resistance thermometer a variable laminar capacitor C is shunted parallel to the decade resistance box D. A low noise high impedance differential amplifier feeds the error signal to a commercial lock-in amplifier (30). Careful shielding and grounding of the leads is of utmost importance. The attenuator has to increased as the temperature goes down to avoid Joule heating. At 0.1 K the AC voltage across the thermometer is $\lesssim 10^{-5}$ Volt, which corresponds to a power input of $\cong 10^{-16}$ Watt.

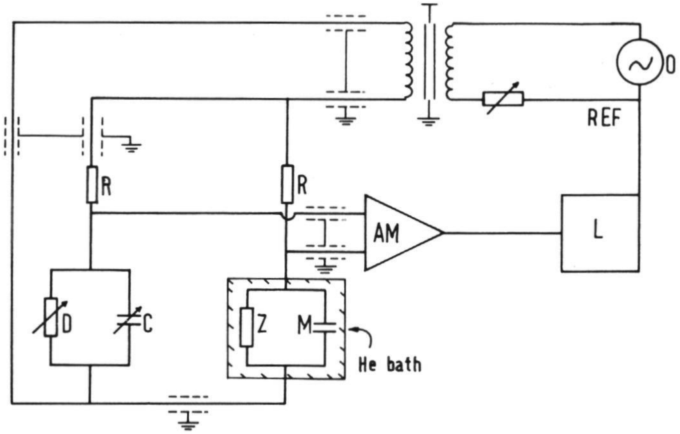

Fig.II.9 AC wheatstone bridge for resistance monitoring. (O) Oscillator (A) attenuator (T) transformer (R) pair of matched resistors (D) decade resistance box (C) variable capacitance (Z) unknown impedance (M) compensating capacitance (AM) high impedance differential amplifier (L) lock-in amplifier.

(ii) As CMN has a relatively small magnetic susceptibility the mutual inductance bridge should be stable and should have a good resolution. The original Hartshorn bridge (35), (36) makes use of a variable mutual inductance which can be compared to the unknown inductance. A serious problem are intracircuit capacities, especially of the variable mutual inductance, because the effective capacitance depends on the setting of the inductance. There are several ways to circumvent the problem (37), (38), (39), but the combination of a fixed mutual inductance with a voltage divider has found the most acclaim (37). The voltage divider is a variable ratio transformer with a high input impedance compared to the

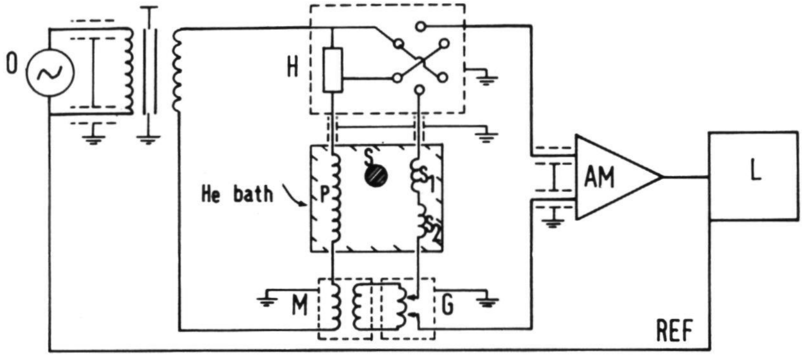

Fig.II.10 Modified Hartshorn bridge.(O) Oscillator (T) transformer (H) 1 Ω helical potentiometer (P) primary coil (S) sample (S1), two secondary coils wound in opposite directions (M) fixed mutual inductance (G) ratio transformer (AM) differential amplifier (L) lock-in amplifier.

secondary of the fixed mutual inductance at the driving frequency. The circuit diagram is given in Fig.II.10. The low frequency high voltage ratiotran of GERTSCH (40) has a high ratio accuracy and a low phase shift, their Model RT-9R has an impedance of 1M Ω at 60 Hz. Again this bridge is very sensitive to pick-up, so both magnetic and electrostatic shielding must be adequate.

The helical potentiometer P, which serves to compensate for intrinsic phase shift between primary and secondary circuit, can be isolated from the primary circuit by means of an additional transformer if one wishes to reduce the capacitive problem further(41).

(iii) Numerous techniques have been developed to measure current-voltage characteristics of tunnel junctions (42), (43), (44), (45). To resolve more structure in the I-V curve it became useful to develop equipment which could give the derivatives $\frac{dV}{dI}$ and $\frac{dI}{dV}$ as well as $\frac{d^2V}{dI^2}$ and $\frac{d^2I}{dV^2}$. As we have seen in Chapter I, at very low temperatures the tunneling density of states of the superconductor is directly proportional to $\frac{dI}{dV}$. For instance the influence of the phonon spectrum on the I-V characteristic can be shown easily if the junction is connected as a four terminal probe in a high accuracy AC bridge which can yield the second harmonic, i.e. the second derivative (46).

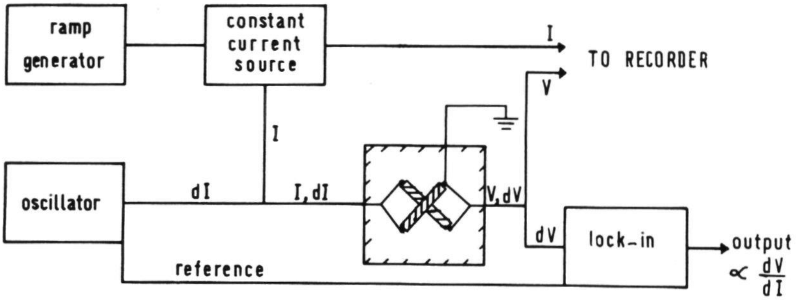

Fig.II.11 Block diagram of tunneling apparatus.

A block diagram of the apparatus we use is shown in Fig.II.11. It consists basically of a ramp generator which drives a constant current source. The current is swept slowly from minus to a positive current value, thus yielding a symmetric characteristic on the X-Y recorder. The junction is used as a four terminal probe through one pair of terminals the current is flowing. The voltage across the other pair is plotted on the X-Y recorder versus the current.

To measure derivatives, one superimposes on the DC current a constant AC current via an oscillator of 460 Hz. The corresponding voltage changes dV are measured with a lock-in amplifier where the output gives the dynamical resistance. One must be very cautious to measure junction impedances. Because the resistance of the junction is unknown at first and may be high ($\approx$ 1k Ω) the oxide layer is readily burnt through by applying a current, unless the sample is in direct heat contact with the He bath. In measuring the first derivative, the modulation current must have an amplitude which is small compared to the gap value and also to kT at the working temperature (kT $\approx$ 86 μeV at 1 K, Δ(aluminium) $\approx$ 200 μeV). With this modulation gap-'smearing' is ruled out. Because the AC current modulation must be constant, the impedance of the junction must be low compared to the current source. One remark should be made about the grounding. Because some junctions are easily destroyed by unwanted currents, it is advisable to connect a proper grounding to the junction itself.

II.5 Experimental results

The results presented here have partly been published elsewhere (47), (48), (49). We will give here most of the details and some additional material.

In the first phase (47) the experiment was performed with a ruby crystal of 0.3% Cr content (atomic percentage); the adiabatic demagnetization was accomplished with a field of 12 kG. At a later stage (48), (49), this field was increased to 23 kG, and we had three rubies of chromium content 0.01, 0.3 and 2% (cf. II.2) at our disposal.

In a typical run, the temperature of the ruby was 0.14 K immediately after demagnetization. During the next hour the temperature goes down slowly to 0.08 K, then rises slowly in two hours to reach 0.6 K. At that moment the buffer salt between the ruby sample and the top of the can is rapidly warming up, because of non-condensed He^4 exchange gas, so the ruby will then soon (within 5 minutes) reach the bath temperature.

We want to derive the absolute temperature from the measured current-voltage characteristics, or from the derivatives of these curves. As we saw in Chapter I there exist for the current I through the junction a relation of the type

$$I = I(T, \Delta(0), \Delta(T), I_{NN})$$

for any superconducting tunnel junction, SS or NS; a similar relation holds for $(dV/dI)_{NS}$. From the measurements one can extract data like I_{SS}, I_{NS}, I_{NN}, $(dV/dI)_{NS}$ as a function of V directly. From the BCS-theory, it is possible to calculate (50) $\Delta(T)/\Delta(0)$ as a function of $t = T/T_c$, and in addition, we have for aluminium in the BCS-weak-coupling limit (51):

$$2\Delta(0) = 3{,}52\ kT_c.$$

Therefore, there are only two unknown parameters T and $\Delta(0)$ (or T and T_c) left in (II.4). As we do not want any temperature-calibrations (i.e. T_c-measurements, which are, due to some smearing out, rather inaccurate),we have to use a method which can determine

$\Delta(0)$ to a sufficient accuracy. Once we know $\Delta(0)$, it is possible to derive the absolute temperature T from the measured current-voltage characteristic, or from the derivative measurement.

We will now treat in detail the procedure used to derive T from the measurements on (i) superconducting SS and (ii) superconducting NS junctions.

(i) A typical set of I-V curves for an Al-Al$_x$0$_y$-Al junction is shown in Fig.II.12. For a SS junction we have (cf. expression (I.37)).

$$I_{SS}\left(T = 0,\ V = 2\Delta(0)\right) = C_{NN}\,\frac{\pi}{2}\,\Delta(0) = \frac{\pi}{4}\,I_{NN}$$

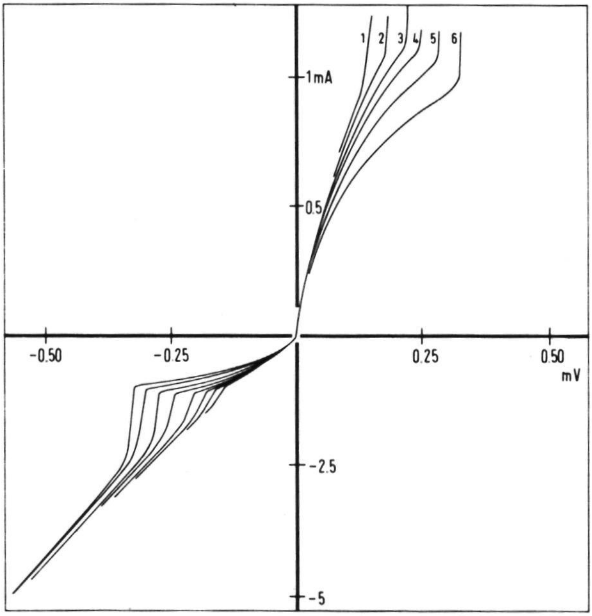

Fig.II.12 Experimental current-voltage characteristics for a Al-Al$_x$0$_y$-Al junction for different temperatures. The positive current scale is expanded five times. The numbers correspond to decreasing temperature.

This formula can be used to construct $\frac{\Delta(0)}{e}$ for a measured I-V

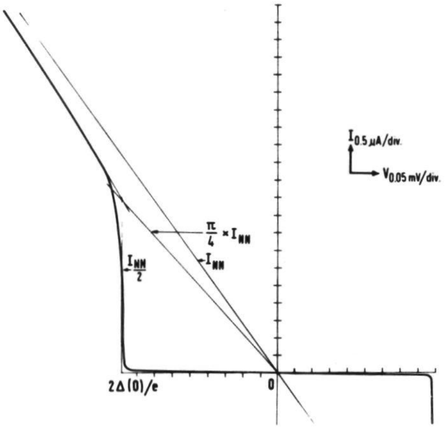

Fig.II.13 Construction of $\Delta(0)$ for a SS junction.

curve with a very good precision (52). The construction is shown in Fig.II.13; $\frac{2\Delta(0)}{e}$ is the voltage where the current is half its value extrapolated from voltages just greater than $\frac{2\Delta(0)}{e}$. The size of the jump in the current at $\frac{2\Delta(0)}{e}$ has to be $\pi/4$, which is a good check whether a good gap value has been chosen or not. I_{NN} can be found when the junction is normal (which is accomplished by applying a magnetic field). The voltage-axis of the measured curve can now be divided into units of $V/2\Delta(0)$, and the current-axis can be divided into units of $I_{SS}/\sigma_{NN}\Delta(0)$, where σ_{NN} is the normal state conductance of the junction. It is then possible to compare the measured curve with the set of computer generated curves seen in Fig.I.14. One can deduct $t = T/T_c$ immediately and because of (II.5) and the determined value of $\Delta(0)$ we can immediately calculate T_{BCS}:

$$T_{BCS} = t\Delta(0)/1.76k_B$$

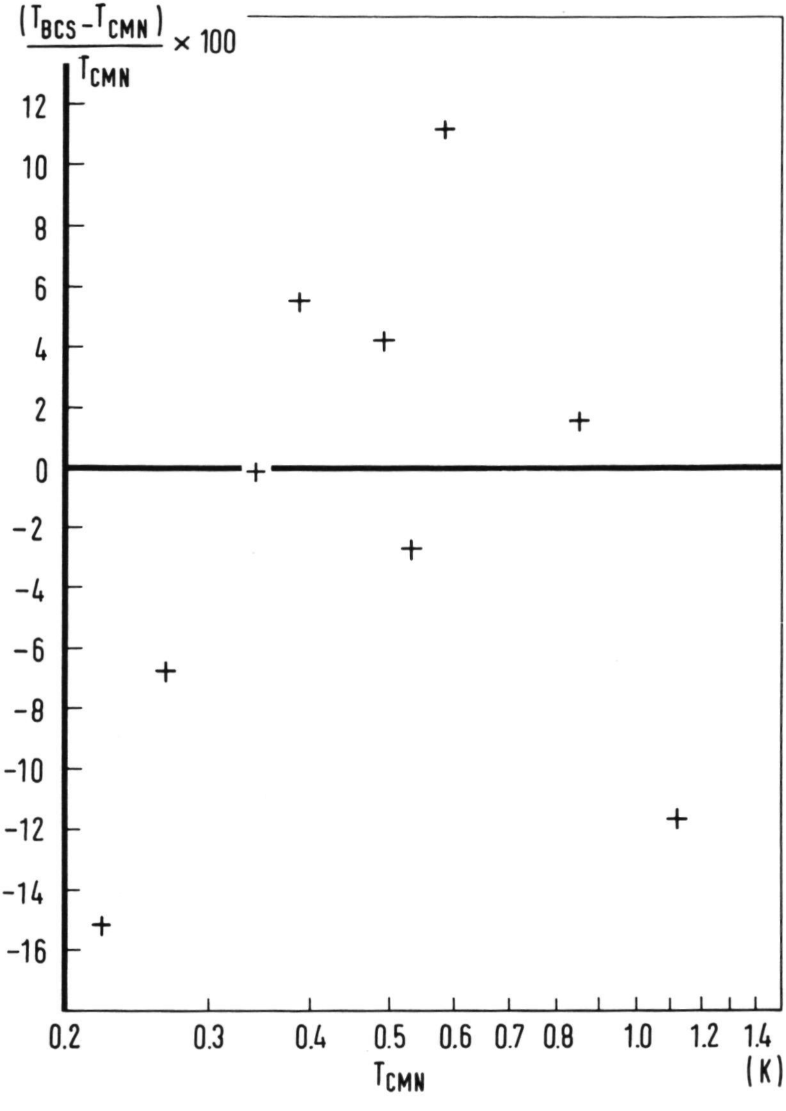

Fig.II.14 Comparison between the temperatures derived from a calibrated thermometer T_{CMN} and from the SS tunnel junctions (T_{BCS}). The indicated points are corrected for a temperature independent part, with $T_{BCS} = T_{CMN} = 0.34$ K (see text).

The temperature derived in this way show a rather large systematic deviation of T_{CMN}, where T_{CMN} is the temperature of the carbon thermometer, calibrated with CMN (see II.3); the deviation $\left((T_{BCS}/T_{CMN})-1\right)x10^3$ ranges from +8% to +36%. The reason for this deviation lies in the effect of double particle tunneling (cf. reference (40), (41), (42) and (57) of Chapter I) which gives a temperature independent part of the tunnel current below 2Δ. In order to check this assumption, we can assume $T_{BCS} = T_{CMN}$ for a certain T (where the temperature independent part becomes important) and we can compare the theoretical current (from the computer generated curve) with the actual measured current. The difference between the two is then taken as the temperature independent part and can be subtracted from all the other measured curves. Using this method, the agreement between T_{BCS} and T_{CMN} is improved, however the measured points still scatter appreciably (Fig.II.14). This rather large scattering may be due to the fact that the lower and upper film comprising the junction do not have identical gaps, large errors are introduced in the determination of Δ(0). We believe that the large deviations in Fig.II.14 are caused mainly by measuring at non-identical superconductor junctions (S_1S_2) and we still use the computer generated curves for a SS junction with identical superconductors.

(ii) For SN junctions there is unfortunately no unambiguously way to determine Δ(0) directly. The calculated I_{SN}/I_{NN} versus V/Δ(0) curves can be derived from Fig.I.10 and are shown as solid lines in Fig.II.15. By measuring the current-voltage characteris-

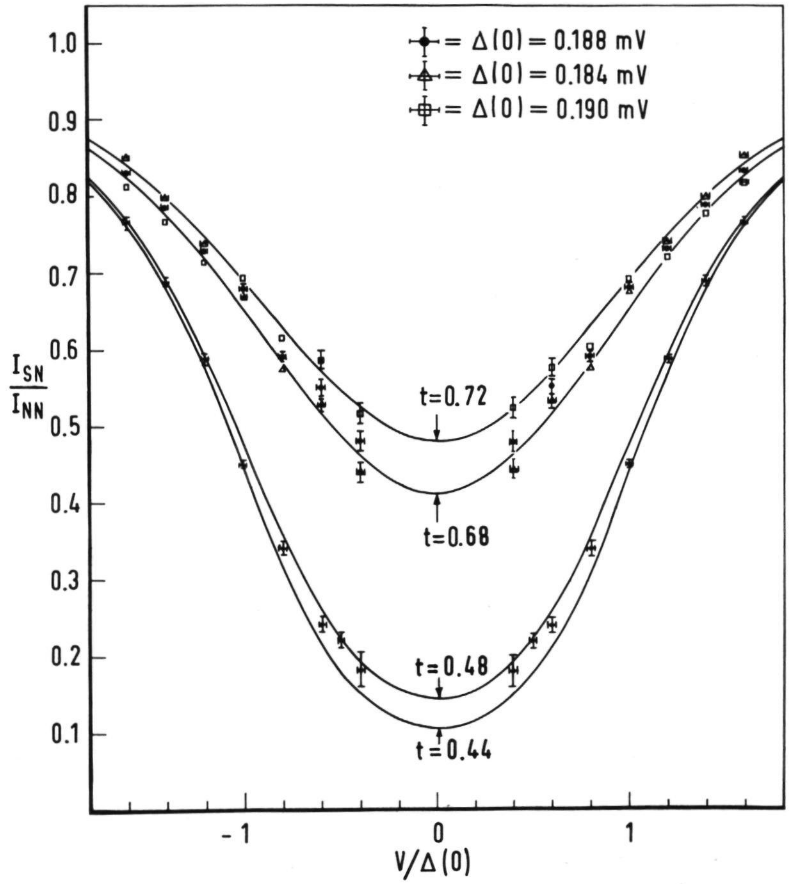

Fig.II.15 Computer calculated curves (solid lines) of I_{SN}/I_{NN} versus V/Δ(0), where t is the reduced temperature parameter. The figure shows that for a gap of 0.188 meV the experimental points lie between the solid lines. For bias voltages > 1, the experimental errors are comparable to the size of the indicated points.

tic when the SN junction is normal, it is possible to divide the current-axis of one measured curve into units of I_{SN}/I_{NN}. By comparing this curve with the computer generated solid lines, Δ(0) and T can be deduced simultaneously. By choosing a certain value for Δ(0), for example Δ(0) = 0.184 meV, it is seen in Fig.II.15

that the measured points deviate above (for $V/\Delta(0) > 1$) and below (for $V/\Delta(0) < 1$) the solid lines. Only when $\Delta(0)$ is chosen correctly, i.e. $\Delta(0) = 0.188$ meV, the measured points lie in between solid lines. This procedure has a resolution of ±1%. Once $\Delta(0)$ is found, all other measured curves can be compared to the theoretical curves of Fig.II.15, and t is deduced directly. T_{BCS} is calculated from (II.6).

An alternative method is to determine the dynamic resistance $(dV/dI)_{NS}$ at $V = 0$, when $\Delta(0)$ is determined by the method described above. The temperature is then found by measuring $(dV/dI)_{NN}$ and comparing the measured normalized dynamic resistance $[(dV/dI)_{NS}/(dV/dI)_{NN}]_{V=0}$ to the theoretical curve shown in Fig.I. 12. From t, T_{BCS} can be calculated again. For temperatures near T_c this derivative-method should be more reliable than the direct I-V-method, because a small deviation from linearity causes a large drop in the dynamical resistance (Fig.II.16). The temperature derived by these methods (T_{BCS}) is compared with the CMN temperature (T_{CMN}) in Fig. II.17. The average deviation is considerably smaller than in the SS case.

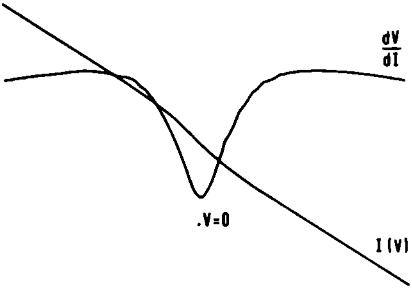

Fig.II.16 The derivative of a current-voltage characteristic for a SN junction slightly below T_c.

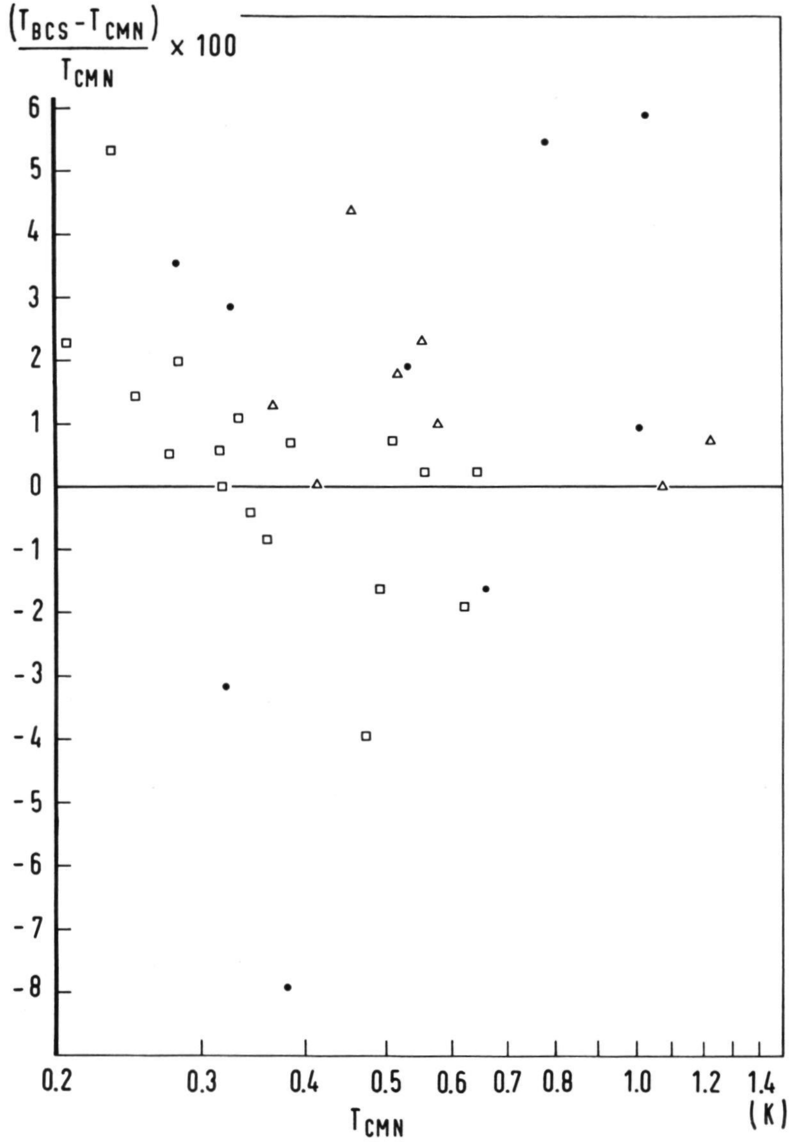

Fig.II.17 Comparison between the temperatures derived from a calibrated thermometer (T_{CMN}) and from the SN tunnel junctions (T_{BCS}). Dots: $(dV/dI)_{V=0}$ measurements, triangles and squares: I versus V measurements. These measurements were done on three different SN junctions.

II.6 Discussion

There are some intrinsic limitations on the use of the junctions as thermometers. Apart from the specific problems in the SS case, in almost all junctions a small normal leakage current exists, which means that we can consider the junction as consisting of an ideal junction in parallel with a resistance. This resistance is caused by small metallic bridges which penetrate through the oxide layer; the dimensions of these bridges are so small that they remain normal due to high current density even at low currents. Although it may be possible to determine the value of the equivalent parallel resistor, at low temperatures the contribution of the leakage current to the total current becomes so large that the junction is no longer suitable as a thermometer anymore. The estimated limit caused by a leakage current for junctions is about 0.1 T_c, e.g. for aluminium 0.12 K. An other superconductor, such as cadmium (T_c = 0.54 K), has then to be used to measure temperatures below 0.1 K.

A second problem for SN junctions is the increase in $(dV/dI)_{NS}/$ $/(dV/dI)_{NN}$ at temperatures below 0.5 t. The value of the dynamic resistance at V = 0 may become so high that the influence of the capacitance of the junction (~ 0.1 nF) can no longer be neglected. In addition, when the dynamic resistance is very low, too much power will be dissipated in the junction. We will calculate the dissipated power in a typical junction. For an Al-Al_xO_y-A_g junction with a normal resistance of 50 Ω, the dissipated power during a tracing from 0 to 400 μV($2\Delta/e$) varies from 0 to 3×10^{-9} Watt. A reasonable expression for the heat transfer from the junction into the ruby is of the form (53)

$$\dot{Q} = 10^{-2}A(T_j^4 - T_s^4),$$

where $\dot{Q}$ is the heat flow per second from the junction to substrate in Watts. 'A' is the junction area in cm^{-2} and T_j and T_s are the junction and substrate temperatures, respectively. From this expression it follows that for temperatures lower than 0.16 K a power dissipation of 3×10^{-9} Watt can cause a temperature difference of 1%. Therefore, below 0.16 K the bias voltage should not exceed 400 μV.

When the temperature is derived from the dynamic resistance at zero bias voltage, the applied voltage should be kept small to prevent smearing. The dynamic resistance (Fig.I.11) becomes more sharply peaked as the temperature gets lower. This would suggest that the lower temperature, the lower the AC voltage of the derivative technique should be. On the other hand, as Fig.I.12 shows, the dynamic resistance becomes a very strong function of the temperature which allows to have a large uncertainty in $(dV/dI)_{NS}$. If we want to know the temperature with an accuracy of 1%, it can be deduced from Figs. I.11 and 12 that a AC modulation voltage of 10 μV should be used in nearly the whole temperature range.

The resolution can be much higher than 1%; e.g. at 0.24 K and using a null detector with 10 nV resolution, the temperature resolution is 0.01%. The dissipated power is extremely low with a measuring voltage of 10 μV; it varies from 10^{-12} Watt at 1 K to

3×10^{-16} Watt at 0,2 K.

We have to remark that the remaining systematic deviation in Fig.II.17 can be due to an error in the determination of $\Delta(0)$ or to non-ideal behaviour of the junction. Although the absolute accuracy might be due to specific junction deviations, the resolution is very high: the dynamic resistance varies as much as 10^7 when the temperature changes from T_c to $0.12T_c$.

Donaldson and Band (54) have used an alternative method to derive the temperature from tunnel junctions, which circumvents the problem of an accurate determination of $\Delta(0)$. Unfortunately, this method is only useful in a very limited large: $t < 0{,}5$ and $2kT \leqslant eV \leqslant \Delta - 1{,}5kT$. For this range it is possible to show that (cf. Ref. (30) of Chapter I):

$$I_{SN} = I_{NN}\, A(\Delta, T)\, \exp(eV/kT)$$

The temperature is then given directly by the slope in a $\ln I_{SN}$ versus V plot.

It should be emphasized that the 'BCS-thermometer' is really a primary thermometer in the sense that no calibration points against any other thermometer are needed.

References

1 For a general review see e.g. H.B.G. Casimir in 'Magnetism and Very Low Temperatures' (Dover Publications Inc., New York, 1961). D. de Klerk in 'Handbuch der Physik', Vol XV (Editor S. Flügge, Springer Verlag, Berlin, 1956) p. 38.

2 H.L. Davis, Phys. Chem. 16, 213 (1958).

3 J.G. Daunt and K. Brugge, Z. Physik Chem. 16, 203 (1958). J.G. Daunt, D.O. Edwards, M. Kreitman, R.C. Pandorf and J.W. Snider, Proc. VIIth Int. Conf. Low Temp. Phys., Toronto 1960 (University of Toronto Press, 1961) p. 96.

4 R.F. Blunt, G.A. Candela, R.A. Forman, A.H. Kahn and B.W. Mangum, J. Appl. Phys. 42, 3058 (1971).

5 Hrand Djévahirdjian S.A., Monthey, Switzerland.

6 J.R. Clement and E.H. Quinnell. Rev. Sci. Inst. 23, 213 (1952).

7 H.H. Plumb and M.H. Edlow, Rev. Sci. Inst. 30, 376 (1959).

8 H. Weinstock, R.A. Guenther and R.W. Schleider, Cryo. Tech. 6, No. 2, 7 (1970).

9 A.S. Edelstein and K.W. Mess, Physica 31, 1707 (1965).

10 Low Temperature varnish N 7031, made by the General Electric Company.

11 Type T48B, supplied by Norton International Inc., Massachusetts 01760, U.S.A.

12 J.E. Robichaux and A.C. Anderson, Rev. Sci. Inst. 40, 1512 (1969).

13 A.C. Anderson in 'Temperature, Its Measurement and Control in Science and Industry' (Instrument Society of America, Pittsburg, 1972) Vol. 4, part 2, p. 273.

14 J.P. Harrison, Rev. Sci. Inst. 39, 145 (1968).

15 C.R. Brown and P. Matthews, Rev. Sci. Inst. 39, 616 (1968).

16 W.A. Steyert in 'Temperature, Its Measurement and Control in Science and Industry' (Instrument Society of America, Pittsburg, 1972) Vol. 4, part 2, p. 1253.

17 'The 1958 He^4 scale of temperatures' National Bureau of Standards Monograph 10, U.S. Department of Commerce.

18 S.A. Friedberg in 'Temperature, Its Measurement and Control in Science and Industry' (Rheinhard Publishing Company, New York, 1965) Vol. 2, p. 370.

19 C.J. Adkins, Phil. Mag. 8, 1051 (1963).

20 G. Faraci, G. Giagninta, N.A. Mancini and J.F. Quercia Proc. XIIth Int. Conf. Low Temp. Phys. (E. Kanda, Ed., Keigaker Publishing Co. Ltd., Tokyo, 1971) p. 423.

21 C.J. van Gurp and A.P. van Gelder, Philips Res. Repts. 19, 400 (1964).

22 I. Giaever, Phys. Rev. Letters 5, 464 (1960).

23 H.J. Levinstein and J.E. Kunzler, Phys. Letters 20, 58 (1966). Proc. Xth Int. Conf. Low Temp. Phys. (M. Malkov, Ed., Vinity, Moskva, 1967) p. 241.

24 Supplied by Billiton-Kawecki Industries, P.O. Box 38, Arnhem, The Netherlands.

25 L. Holland in 'Vacuum Deposition of Thin Films' (J. Wiley & Sons, Inc., New York, 1961).

26 L. Maissel and R. Glang in 'Handbook of Thin Film Technology' (McGraw-Hill Inc., New York, 1970).

27 Alconox, cleaning agent, trademark of Alconox Inc, New York. Distributed in Holland by Pleuger, Amstelveen.

28 Supplied by the Servometer Corporation, Clifton, New Yersey 07012, U.S.A.

29 Grade AGOT Nuclear Graphite, Union Carbide Corp., Carbon Products Division, New York 10017, U.S.A.

30 D.O. Edwards, R.E. Sarwinski, P. Serigmann and J.T. Tough, Cryogenics 8, 392 (1968).

31 Ciba epoxy CY230 and elastic component CY208 with hardener HY951.

32 H. van Kempen, F.H. Mischgofsky and P. Wyder, Rev. Sci. Inst. 43, 1209 (1972).

33 Autotransfomer G-10, made by TRIAD, division of Litton Precision Products Inc., Indiana 46750, U.S.A.

34 Princeton Applied Research lock-in amplifier type HR-8

35 L. Hartshorn, J. Sci. Instr. 2, 145 (1925).

36 H.B.G. Casimir, W.J. de Haas and D. de Klerk, Physica 6, 241 (1939).

37 E. Maxwell, Rev. Sci. Instr. 36, 553 (1965).

38 W.L. Dillinger, P.S. Jastrum and J. Daunt, Rev. Sci. Inst. 29, 159 (1958).

39 A.C. Anderson, J. Appl. Phys. 39, 5878 (1968).

40 GERTSCH subsidiary of Singer Company, metrics Division, Los Angeles 16, U.S.A.

41 A.C. Anderson, R.E. Peterson and J.E, Robichoux, Rev. Sci. Instr. 41, 528 (1970).

42 I. Giaever, H.R. Hart and K. Megerle, Phys. Rev. 122, 1101 (1961).

43 J.S. Rogers, J.G. Adler and S.B. Woods, Rev. Sci. Inst. 35, 208 (1964).

44 D.E. Thomas and J.M. Rowell, Rev. Sci. Instr. 36, 1301 (1965).

45 A. Langacre, Jr., Rev. Sci. Instr. 41, 448, (1970).

46 J.G. Adler and J.E. Jackson, Rev. Sci. Instr. 37, 1049 (1968).

47 J.W. Bakker, H. van Kempen and P. Wyder, Phys. Letters 31A, 290 (1970).

48 J.W. Bakker, H. van Kempen and P. Wyder, Proc. IIIth Int. Cryogen. Eng. Conf., (Iliffe Publications Ltd., Berlin, 1970) p. 217.

49 J.W. Bakker, H. van Kempen and P. Wyder in 'Temperature, Its Measurement and Control in Science and Industry' (Instrument Society of America, Pittsburg, 1972) Vol. 4, part 2, p. 273.

50 B. Mühlschlegel, Z. Physik 155, 313 (1959).

51 B.L. Blackford and R.H. March. Can. J. Phys. 46, 141 (1958).

52 J.W. Rowell in 'Tunneling Phenomena in Solids' (Plenum Press, New York, 1969) p. 281.

53 D.A. Neeper and J.R. Dillinger, Phys. Rev. 135, A1028 (1964).

54 G.B. Donaldson and W.T. Band, Bull. Inst. Int. Froid, annex 1970-2, 27 (1970).

CHAPTER III. A NEW PHONON-SPECTROSCOPY IN THE VERY HIGH FREQUENCY REGION (10^{11} Hz)

III.1 Introduction

Most of the relevant energies of solid state physics correspond to temperatures in the region from, say, 1 K to 1000 K (i.e. Debye-temperatures). The energies involved are in the meV region (which corresponds to frequencies of 10^{11}Hz), where a variety of interesting phenomena should occur. Unfortunately, it is rather difficult to get energy-quanta (phonons, photons etc.) for this energy region; for instance using electromagnetic radiation as a source and suitable detectors, both far-infrared and microwave techniques become tedious at the frequency range of 10^{11}-10^{13}Hz, and until a few years ago, it was almost impossible to get monochromatic phonons in this frequency region.

However, recently new techniques have been developed to generate and detect (in)coherent monochromatic phonons in the Tera-Herz (THz) region (1), (2). It is the subject of this chapter to illustrate the use of some of these methods as a spectroscopic tool. As an example, the energy gap of most known superconductors correspond to frequencies above 50 GHz. It may be revealing to study energy gaps, as well as other characteristics of superconductors, by means of high frequency elastic waves. The electrons are strongly coupled to the phonons with energies of some meV and the direct examination of this coupling energy via elastic waves should be useful in expanding our knowledge of superconductivity as well as facilitating more sensitive detection of sound at very high frequencies. Similarly,the vast assortment of impurities and defect centers found in insulating and semiconductor crystals gives rise to numerous magnetic,vibrational and electronic spectra which correspond to thermal phonon frequencies. Selection rules governing such transitions often favor phonon excitation over electromagnetic excitation. Hence, apart from the difficulties in reaching this energy range conventional electromagnetic methods are sometimes excluded. Moreover, ultrasonic experiments carried out in the 10^{11}-10^{13}Hz range could accurately determine thermal phonon lifetimes and dispersion relations (ω versus k).

Of course, $\omega(k)$ can also be obtained from neutron- or X-ray scattering measurements; however, these methods are unfortunately not able to give e.g. directly the frequency dependence of the group velocity. Sound dispersion measurements in the THz-frequency region in quantum liquids such as liquid He II would also be of great interest.

Let us review the different methods which are used to generate and detect THz phonons. Generation and detection of sound waves by piezo-electric or magnetostrictive devices is limited up to frequencies of 10^{10}Hz, because irregularities of a surface prohibits propagation of phonons with wavelengths much smaller than 1000 Å. Brillouin scattering of photons at a crystal lattice generates phonons, but the frequency is not tuneable.

By application of heat pulses it is possible to generate phonons with frequencies up to 10^{13}Hz. For example, if an evaporated metal film is Joule heated by passing through a pulsed current,a thermal pulse is generated which consists of a superposition of a wide band of randomly phased frequencies approximately centered around 3 kT/ħ. If the phonon mean free path in the crystal is long enough, the heat pulse will be transmitted as such and can for example be detected after some 'flight-time' by a superconducting bolometer. This type of 'time resolved' thermal conductivity experiment is sketched in Fig.III.1.

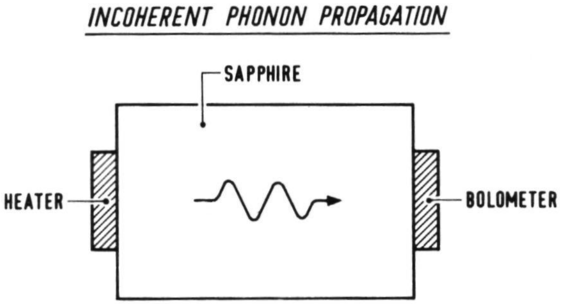

Fig.III.1 Generation and detection of incoherent phonons.

This arrangement of heater and detector was known for some time in second sound studies in liquid helium (3) but as the velocity of sound in helium is three orders of magnitude smaller than in dielectric crystals, much slower heaters and detectors (carbon thermometers) can be used. It is only recently that this type of 'time of flight' thermal conductivity experiments have been performed on solids (6), taking advantage of the fact that superconductors have much faster response times than the conventionally used carbon thermometers.

To really study resonant scattering processes with phonons, this method of thermal pulses is not very well suitable because the spectral resolution of this type of experiment is limited to something like ~ kT (6).

It will be shown in the next paragraph that superconductors are able to generate incoherent monochromatic phonons, and also that they can act as frequency-selective detectors.Since the paper by Eisenmenger and Dayem (7) where these ideas were presented for the first time, quite some time elapsed until other people were able to use this technique due to many technical difficulties. However, in the last two years, superconductors have found wide usage as generators and detectors for monochromatic phonons in the THz region.

There are a few other devices which are able to generate and detect THz phonons. The spin-phonon spectrometer of Anderson and Sabisky (8) makes use of splitting of paramagnetic spin levels by a magnetic field. The need for this field rules out the use of fast superconducting bolometers or tunnel junctions and is limited to the use of relatively slow 'avalanche' semiconductors (9). Renk and Deisenhofer(10) make use of the optical transition in ruby (29 cm^{-1}) to detect phonons of this energy. In addition, a great number of alternative methods for generation and detection has been proposed very recently, neither of which has however already led to experiments (11,12, 13, 14).

III.2 Phonon processes in superconductors

In the decay of electronic excitations in superconductors, phonons play the most important role. Tewordt (15) has shown, that for T = 0 the decay of excitations with energies above the gap can be analysed on basis of the BCS theory in terms of a two step process, during which incoherent phonons are emitted. In a first step, the excitations relax to the gap edge, under emission of a 'relaxation' phonon, characterized by a relaxation time τ_{rel}; after a time τ_{rec} two excitations will then combine to a Cooper pair from the gap edge to the ground state under emission of a monochromatic phonon.

During relaxation, two-phonon emissions are negligible compared to single phonon emission (15). Photon emission can also occur, but this has a probability which is 10^{-4} times smaller than the probability for phonon emission (15), (16). There are indications that this has been confirmed experimentally (17).

The situation is not much changed if the theory is generalized to finite temperatures (15). Thus, superconductors can be used as quantum-phonon-generators. The emitted phonon spectrum consists of a continuous relaxation spectrum with an energy range from 0 to a cut-off energy, determined by the quasi-particle with the highest energy above the gap. In addition, monochromatic phonons with a frequency equivalent to 2Δ are emitted. It has to be noted that even at T = 0, this monochromatic peak will be smeared out due to anisotropy and spatial variation of the gap (these effects are not accounted for in (15).

If superconductors are to be used as practical phonon-generators, the emitted spectra should be reasonably well defined, i.e. τ_{rel} and τ_{rec} must be sufficient large, because of the uncertainly principle ($> 10^{-10}$ sec). On the other hand, because of the used pulse widths in the experiment, τ_{rel} and τ_{rec} must be smaller than 10^{-7} sec (cf. III.6). Experimental information on τ_{rec} has been obtained from tunneling measurements on lead and aluminium (18), (19), (21), (22), and from phonon spectroscopy measurements on Sn (23); until now, only one experiment has given information on τ_{rel} (19) and indicates, that τ_{rel} is extremely small (10^{-9} sec). The first theoretical investigations were carried out by J.R. Schrieffer and D.M. Ginsberg (16); assuming a spherical Fermi surface and an average electron-phonon coupling constant derived from high temperature resistivity, they calculated a value of the order of 10^{-8} sec for τ_{rec} for Pb at 1.4 K. In these calculations, it was assumed that the number of the injected quasi-particles in a tunneling experiment (18) can be neglected compared with the thermally excited quasi-particles. Rothwarf (24) pointed out, that this assumption may easily be invalid, and he found that τ_{rec} was one order of magnitude larger (10^{-7} sec). He derived a temperature dependence for τ_{rec} for low temperatures where τ_{rec} varies as $T^{-\frac{1}{2}} \exp(\Delta/kT)$ and is roughly inversely proportional to the number of thermally excited quasi-particles present. In thin films, the thickness may also be a parameter which influences τ_{rec} (25) due to boundary effects. When the thickness is smaller than a certain critical value d_0 (for Al d_0 = 175 Å), only phonons with wave vectors in the plane of the film can be emitted in the recombination process. This means that for experiments where we want the phonons to travel from the superconductor to the substrate, the film thickness should be larger than d_0, e.g. for Sn the films should be at least 500 Å thick.

Measurements on the weakly coupled superconductors (Al, Sn) tend to give results for τ_{rec} which are at least one order of magnitude smaller than in the case of lead (19), (21), (22). A value of 10^{-7} sec for Sn at 1.2 K agrees with all measurements hitherto.

However, it has been shown recently (23), (26) that a correction must be made with respect to the simple two-step decay process as suggested by Tewordt. Let us consider a relaxation process, in which an excited quasi-particle emits or absorbs a phonon of energy $\hbar\omega$ in a transition to a level $E \pm \hbar\omega$ where E is the quasi-particle energy measured from the Fermi-level. A recombination process can follow in which two excited quasi-particles of energy $E_1(\geqslant \Delta)$ and $E_2(\geqslant \Delta)$ form a Cooper pair, emitting a phonon of energy $(E_1 + E_2) \geqslant 2\Delta$. The relaxation process is slow for small values of $\hbar\omega$ because both the phonon density of states and the coherence factor in the superconductor are small for small $\hbar\omega$, especially near the gap edge, where the coherence factor tends to zero. In fact, a finite energy range exists in the vicinity of Δ, where $\tau_{rec} < \tau_{rel}$. It is this range which is responsible for the width of the phonon peak at 2Δ in the emitted spectrum (5). If one plots Δ/kT as a function of E/Δ(27), one gets an asymptotic behaviour of the curve which describes the equal probability of relaxation and recombination. For $E/\Delta = 1$ (and $\Delta/kT \rightarrow \infty$) recombination is dominant ($\tau_{rec} < \tau_{rel}$), and for $E/\Delta \rightarrow \infty$(and $\Delta/kT \rightarrow 0$) relaxation is dominant

($\tau_{rel} < \tau_{rec}$).

It is possible (5) to calculate the emitted phonon spectrum of a superconductor by taking into account properly the fact, that excitations do not decay to a single level, but do decay to the continuous distribution of available states. Taking arbitrarely 40 different excited states above the gap with equidistant separation of 0.05Δ, the resulting spectrum is shown in Fig.III.3. A few salient features of this important plot should be indicated. The spectrum consists indeed of a continuous re-

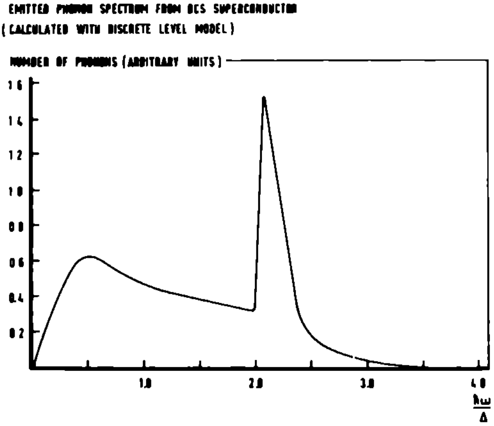

Fig.III.3 Emitted phonon spectrum from a BCS-superconductor after injection of quasi-particles, (For the calculation, 40 equidistant discrete levels above the gap were used (5)).

laxation part from zero to about $\hbar\omega/\Delta = 3$, and a 'monochromatic' peak is superimposed at $\hbar\omega/\Delta = 2$. As expected, the number of relaxation phonons goes to zero as $\hbar\omega/\Delta \to 0$. The probability of a relaxation phonon of energy $\hbar\omega \geqslant 3\Delta$ to be emitted from the superconductor becomes very low, because the reabsorption of the emitted high energy relaxation phonons becomes important. The reabsorption process will ultimately lead to a build up of 2Δ recombination phonons and of relaxation phonons of relatively low energy, which leads to the maximum in the relaxation spectrum at $\hbar\omega/\Delta \approx 0.5$.

So far, we have only considered the generation of phonons in a superconductor. However, as indicated above in the reabsorption process, high energy phonons of energy $\hbar\omega \geqslant 2\Delta$ have short lifetimes in a superconductor. They are able to break up Cooper pairs, thus increasing the number of excitations. If this increase of the number of excitations could be monitored, superconductors will be able to serve as quantum detectors. The attenuation of sound was already attacked by BCS (28) who calculated the absorption in the low frequency region. If $\hbar\omega \ll 2\Delta(T)$ one has

$$\alpha_s/\alpha_n = 2f(\Delta) \qquad \text{(III.1)}$$

where α_s and α_n are the absorption coefficients in the superconducting and normal states, respectively, and 'f' is the Fermi function. If however $\hbar\omega$ is not small compared to $2\Delta(T)$, the simple relation (III.1) does not hold anymore and an integral expression has to be evaluated, which apart from the appearance of the coherence factor is similar to the tunneling formulas

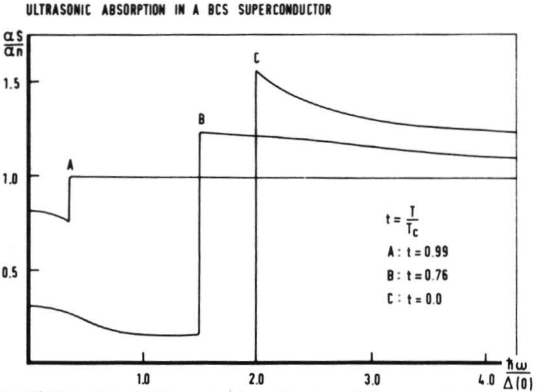

Fig.III.2 Theoretical curves of ultrasonic absorption in a BCS-superconductor for three different temperatures as a function of the phonon frequency (4).

(cf. Chapter I). One part of this integral gives only a contribution to α_s/α_n when $\hbar\omega \geqslant 2\Delta(T)$; this is the so called pair breaking term, and has the physical significance of breaking a Cooper pair by a phonon with an energy $\hbar\omega \geqslant 2\Delta(T)$.

Bobetic (4) has evaluated the integral; the results are shown in Fig.III.2. We note the large discontinuous change in absorption when $\hbar\omega = 2\Delta(T)$. The infinite slope of the edge arises from the square-root singularities in the BCS density of states (cf. expression (I.10))and is in contrast with the lineair rise in absorption at the corresponding energy treshold in electromagnetic absorption (29). The height of the drop in absorption decreases as $t = T/T_c \rightarrow 1$, due to the additional absorption of thermally excited quasi-particles. Nevertheless, even at $t \leqslant 1$ there is an infinite sharp treshold at $\hbar\omega = 2\Delta(T)$.

For Pb and Sn, the change of α_s at the gap edge corresponds to a change of 10^4 to 10^3 in the phonon mean free path. The absolute magnitudes of α_s/α_n are difficult to estimate because the lack of a precise value of α_n. To indicate the order of magnitude, one can extrapolate (30) the ultrasonic absorption measurements of Mason et al. (31) for the longitudinal mode to a frequency of 300 GHz($\approx 2\Delta$ of tin), and the result is a mean free path of the order of 1000 Å.

III.3 Generation of phonons

III.3.1 Phonon generation with a SS junction

In a superconducting SS-tunnel junction, quasi-particles are injected in one of the superconductors comprising the junction under the influence of an applied bias voltage (cf. Chapter I). In the foregoing paragraph we saw that the subsequent deexcita-

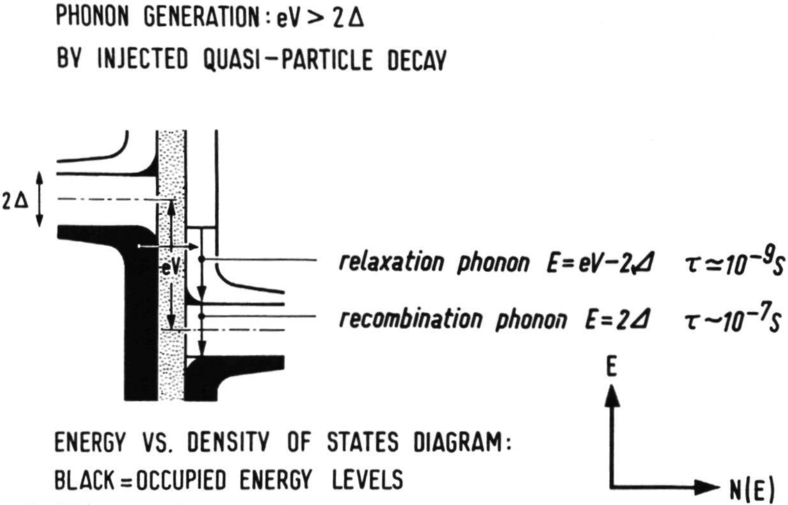

Fig.III.4 Generation of relaxation- and recombination-phonons by a SS junction.

tion of the quasi-particles is accompanied by the emission of monochromatic incoherent phonons.

We can illustrate phonon generation by a superconducting [illegible] junction most easily with the help of the semiconductor diagram (cf. Chapter I). From Fig.III.4, it is seen that after applying a bias voltage for which $V > 2\Delta$, injected quasi-particles have an energy range from Δ to $V-2\Delta$ with respect to the Fermi level. Thus, the continuous relaxation spectrum extends from $\hbar\omega = 0$ to a cut-off energy $\hbar\omega = V-2\Delta$. The succeeding recombination of the quasi-particles results in emitting recombination phonons of energy 2Δ.

When $V < 2\Delta$ and $T = 0$ K, there are no available states at the right, so there will be no emission of phonons. When $T \neq 0$, thermally excited quasi-particles may tunnel and give rise to relaxation and recombination phonons. If however the temperature is low ($T \leqslant 0.3\ T_c$) this effect is negligible.

For $2\Delta < V < 4\Delta$, the intensity of the monochromatic 2Δ peak rises linearly with generator current, because all injected quasi-particles contribute to one recombination phonon of energy 2Δ. When $V \geqslant 4\Delta$, we may expect a non-linear increase in the 2Δ phonons for two reasons:

(i) When $V \geqslant 4\Delta$, additional 2Δ phonons are created because the cut-off of the relaxation spectrum ($V-2\Delta$) extends beyond 2Δ.

(ii) Significant reabsorption of phonons of energy $\geqslant 2\Delta$ will take place by pair-breaking followed by the creation of additional 2Δ phonons when the secondary quasi-particles recombine to form Cooper pairs. That reabsorption is important in a tunnel junction has been pointed out by Kinder et al. (32).

Because relaxation phonons have a continuous energy distribution between 0 and V-2Δ, they must be emitted in pairs of total energy V-2Δ by energy conservation. This, plus the recombination energy 2Δ adds up to the total energy V supplied by the tunneling of one electron. Therefore, in first order we may expect a ratio of relaxation to recombination phonons of two (7), (33).

Above a bias voltage V = 6Δ, a second quantum step is expected; the situation is more complicated compared to the 4Δ step, because it is possible that two phonons of energy 2Δ are being emitted instead of one relaxation phonon with energy 4Δ.

As explained in III.2, the emitted spectrum consists not of a uniform distribution of relaxation phonons and a monochromatic peak of 2Δ recombination phonons. Instead the spectrum is altered somewhat due to - amongst other reasons - the actual phonon density of states of the superconductor (5), (34). However, the overall features of the spectrum depicted in Fig.III.2 are explained by the simplified semiconductor description.

III.3.2 Phonon generation by means of a fluorescence film

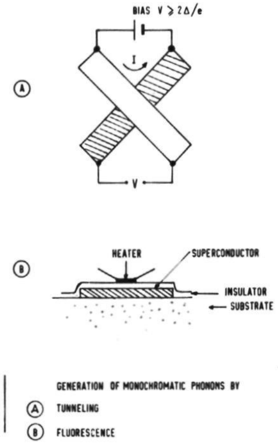

Fig.III.5 Two methods of phonon generation. (A) Via injection of a quasi-particle-current (I) with a bias voltage ≥ 2Δ/e (B) via pumping of the superconductor with a heat pulse (fluorescence).

For the excitation of very high frequency phonons, it is possible to use superconductors in other configurations then in tunneling junctions. One of these other possibilities is the use of a heat pulse in combination with a superconducting 'filter' (fluorescence film). In Fig. III.5 the tunneling method and the fluorescence method are sketched. In (A), excitations are generated by injection of quasi-particles, as described in III.3.1. In (B), a heat pulse is generated by applying an electrical pulse to a thin metal film, for example constantan. If the film has a temperature which is much less than the Debye temperature, phonons will be generated due to the electron-phonon interaction and more important, due to inelastic collisions of electrons with impurity atoms (35). The resulting phonon spectrum is Stephan-Boltzmann in character (36) and has a maximum at $\hbar\omega \approx 3kT$, where T is the heater temperature. The metal film is isolated electrically from the superconductor, which shields the black body heater from the underlying sample. The phonons of energy $\hbar\omega \geqslant 2\Delta$ which escape the heater and reach the superconductor, have a high scattering rate for pair breaking. The resulting quasi-particles excited above the gap edge will emit a relaxation phonon plus a recombination phonon of energy 2Δ. If the relaxation phonons have energies greater than 2Δ, they will be reabsorbed and break Cooper pairs. In much the same way as in III.3.1, the repeated quasi-

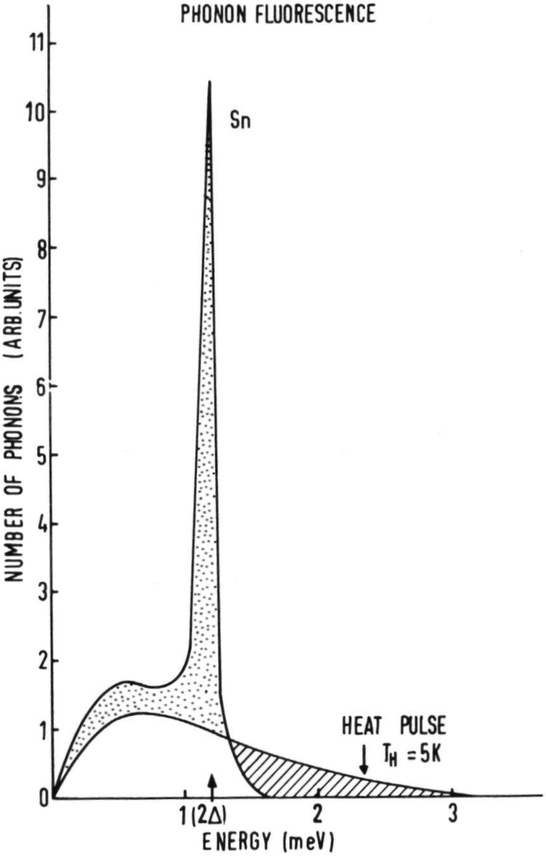

Fig.III.6 Calculated frequency 'down' conversion of a heat pulse of energy 5 K by superconducting tin (1).

particles relaxations and their subsequent recombinations with other quasi-particles to form Cooper pairs will result in a non-linear build-up of 2Δ phonons. Narayanamurti(1) has calculated the resulting emitted phonon spectrum, shown in Fig.III.6. The similarity with Fig.III.2 is striking. For the calculations, an ambient temperature of 0 K (i.e. no thermally excited quasi-particles are present) is used; further it is assumed that the superconducting film is black, i.e. all phonons of energy $\hbar\omega \geqslant 2\Delta$ are absorbed. These assumptions should certainly be valid when $T \lesssim 0.3\ T_c$. It is worthwile mentioning that pulsed laser light can also be used to generate heat pulses (37), thus circumventing some of the electronic problems (cf. III.5.2) encountered in phonon spectroscopy.

III.4 Detection of phonons

As was pointed out in III.2, the lifetime (and the related mean free path l) of phonons with energies $\hbar\omega \geqslant 2\Delta$, is extremely short in superconductors ($l \approx 1000$ Å for Sn). The increased number of quasi-particles, caused by the breaking of Cooper pairs via phonon absorption, can be detected by a superconducting tunnel junction in a complementary way to the generation of phonons in such a junction. If the junction is biased in the voltage range of thermal quasi-particle tunneling $0 < V < 2\Delta$ (cf. Fig.III.7), incident phonons of energy $\hbar\omega > 2\Delta$ are strongly absorbed by brea-

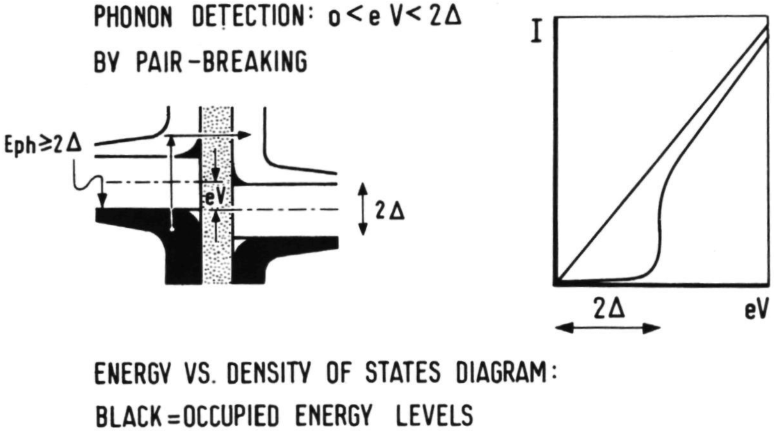

Fig.III.7 Detection of phonons with energies $\geq 2\Delta$ by a SS junction.

king Cooper pairs. The increase of quasi-particles by the extra 'superthermal' excitations leads to an increase in current, which in turn causes a large drop in the voltage for a constant current biased junction, which then can be detected easily. For $T = 0$ K, the absorption disappears for phonons with $\hbar\omega < 2\Delta$.

It is evident from Fig.III.2 that for $T \neq 0$ K, e.g. $t = 0.5$, there will be still some absorption for energies $< 2\Delta$, amounting to about 0.05 of the normal state value (4), and a small shift in the position of the discontinuous absorption increase corresponding to the temperature dependence of the energy gap $2\Delta(T)$. The phonons of energy $\hbar\omega < 2\Delta$ will only interact with the excited quasi-particles (they are not able to break Cooper pairs) and therefore will not contribute in the increase of the tunnel current. For film thicknesses (1000 Å) and temperatures ($T \lesssim 0.3\ T_c$) we used,the detector junction can be assumed to be perfectly black for phonons $\hbar\omega \geq 2\Delta$, and transparant for phonons $\hbar\omega < 2\Delta$, while the width of the absorption edge is mainly determined by the gap anisotropy (1). The phonon detectors described above are quantum detectors, i.e. they are frequency selective. This is in contrast with superconducting bolometers, where the superconductor is simply heated up and its resistive transition is used as the signal generator; they behave like broadband detectors (38). The response time of a junction with a surface of ≈ 1 mm^2 is typically of the order of 10 nsec, thus enabling time resolved phonon spectroscopy (time-of-flight measurements).

For detection, the junction is biased in a region beneath 2Δ, where the current-voltage curve is roughly linear. For small incoming phonon radiation, the response of the junction can be con-

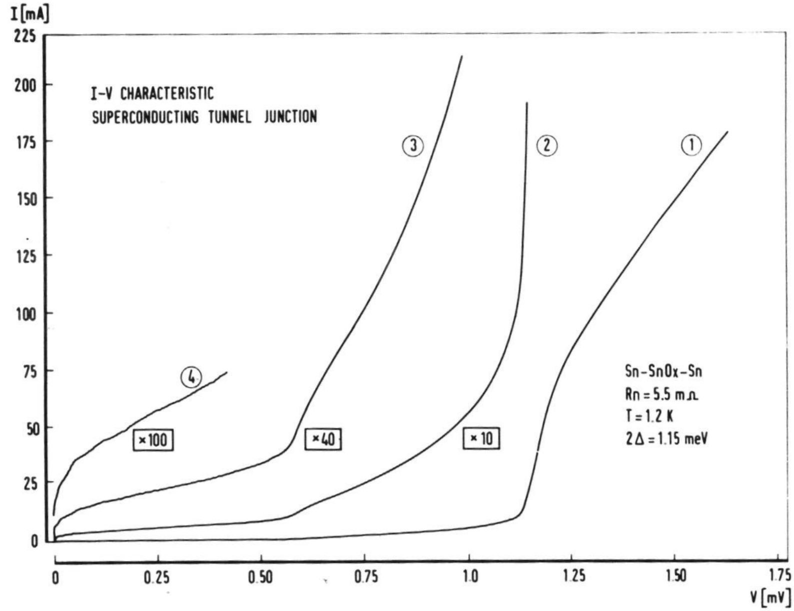

Fig.III.8 The current-voltage characteristic for a tin SS junction. The current scale has been magnified by factors 10, 40 and a 100 to show various details of the curve (see text).

sidered as linear. In Fig.III.8 a typical I-V curve is shown for bias voltages $V \lesssim 2\Delta$. The curve is linear for $V \approx 1.6\Delta$. It has been magnified to show some interesting phenomena, some of which has already been mentioned in Chapter I and II. The following effects can clearly be seen:

(i) Temperature independent double particle tunneling, beginning at $V = \Delta$ (cf. II.5, SS case).

(ii) DC-Josephson effect, i.e. a DC supercurrent is flowing at zero bias (39).

(iii) Fiske (40) steps between $V = 0$ and $V = \Delta$ at constant voltage intervals, arising from the interaction of AC-Josephson radiation with the modes of the electromagnetic cavity, formed by the junction.

Josephson- and related effects ((ii) and (iii)) can easily be suppressed by applying a small magnetic field of 20 G. However, if supercurrents persist at higher magnetic fields, they are attributed to small shorts penetrating in the oxide layer; the net current consists then of a supercurrent portion plus a 'true' tunneling portion. It was found that a junction with an intolerably large shortage current, i.e. amounting to $I(V = 0.1\Delta)$, did not detect phonons in a reproducible manner.

III.5 Experimental details

III.5.1 Sample preparation

The methods to clean the ruby sample have adequately been described in II.4.1. The same procedure holds for the sapphire. The sapphire single crystal is of a high quality synthetic material with a low dislocation density of 10^2-10^3 cm^{-2} (41). The cylindrical axis is parallel to the c-axis within ±1°. The polished faces were plane and parallel to 1/20 of the sodium light wavelength, as specified by the supplier (42) (43).

In Chapter II we were dealing with tunnel junctions consisting of at least one aluminium film. For the phonon generation and detection we restricted ourselves to Sn as superconductor, because then at 1 K, $T \approx 0.3\ T_c$. Tin barely forms a natural grown oxide layer, which has the advantage that these tunnel junctions can be stored at room temperature in an excicator for at least half a year without detoriation, but it is difficult to prepare Sn junctions with a thick oxide layer as barrier. We have found it necessary to initiate an ionic glow discharge of O_2 inside the vacuum chamber (cf. Fig,II.5) at an oxygen pressure of 100 micron Hg. After oxidation for one hour using this method and completion of the second Sn layer (without opening the bell-jar) the impedance varies between 0.1Ω and a few mΩ per mm^2.This wide range may be attributed to different humidity conditions and evaporation rates of the films - both of these factors are known to influence the growth of oxide layer severely (cf. Ref. (26) of Chapter II). However, when two tunnel junctions are made shortly after each other at opposite surfaces of a sample, the two impedances are in the same order of magnitude. As an illustration, Fig.III.9 shows an evaporated junction with gold contacts on a sapphire crystal.

Fig.III.9 An evaporated junction on a cylindrical sapphire crystal.

A remark should be made about the tin we used in the evaporation boats. It turns out that junctions are of consistently bad quality (i.e. a large shortage current) if one uses tin made in the form of small diameter (~ 1 mm) wire as starting material for the evaporation. Contamination is less if one uses bulky tin wire of diameter 3-4 mm, and 90% of the resulting junctions, if oxidized for about one hour, are of good quality.

A fluorescence film consists of successive layers of a superconductor, an insulating layer and a heater (see III.3.2). The insulating layer is made of silicon dioxide, an extremely difficult material to evaporate in the conventional way by resistive heating. We followed an ingenious recipe due to Nesh (44). A tungsten filament is dipped several times into a colloidal solution of SiO_2 in water. A thin layer of SiO_2 is then formed on the filament after the water is evaporated. Because of the intimate heat contact between filament and the colloidal SiO_2 it is possible to evaporate the SiO_2 with modest currents through the filament. The resulting films are pinhole free and are roughly 3000 Å thick.

The heater is made of constantan, an alloy of 60% Cu and 40% Ni. There exist methods to evaporate alloys in a precise and well determined composition, for example flash evaporation of small pellets, where the evaporated film has the same composition as the pellets. However, for our experiment we simply need a heater of 50 Ω and the composition of the heater is of no importance. We used small threads of constantan wire wound on a tungsten filament. When using a fairly high evaporation rate (100 Å/sec), the film is then roughly made of the same mixture as the constantan wire. The resistance was monitored outside the vacuum chamber during evaporation and it takes roughly 5 seconds to reach 50 Ω. A fluorescence generator is shown in Fig.III.10. We would like to be sure that heat is only dissipated in the constantan heater, so we used evaporated superconducting Sn leads as contacts to the heater.

Fig.III.10 A fluorescence film on a cylindrical sapphire crystal. The little square seen in the centre is the constantan heater.

III.5.2 Electronic circuitry

The measuring methods used to investigate phonon generation and detection are of two different types: (i) the pulsed time-of-flight method, and (ii) the AC modulated DC method. We will treat both methods successively and indicate the different experimental situations in which a specific method should be used.

(1) The 'time-of-flight' method.

With this method, the generator is excited during a short time, in our case via an electrical pulse applied to the junction generator or the fluorescence generator. The pulse width should be larger than τ_{rec}; i.e. $> 10^{-7}$ sec. The generated phonons will partly cross the metal film-sapphire interface (the transmission factor is ≈ 85% (35)) and propagate through the sapphire with the specific velocity corresponding to the polarization of the phonon modes. After the transmission through the crystal, the modes will be separated (if the pulse widths are short enough compared to the transit time) and successively be detected by the detector, which is a constant current biased junction. After amplification, the signal is fed into a boxcar integrator (45). The boxcar integrator is ideally suited for this type of measurement as it samples with a chosen rate, the signal with a small gate which can be varied in width. The information is stored in an analog way in capacitor circuits and is read out on a X-Y recorder during a sweep of the detector signal. The output signal is fed to the Y-axis of the recorder, and the sweep is fed to the X-axis. A plot is then obtained of the detector signal versus time. It is also possible to use the gate fixed in the time, e.g. at a time corresponding to a specific detector pulse, for instance the transversal phonon mode. In this way one can measure the amplitude of the detected phonon pulse as a function of another parameter, for example the magnetic field (cf. III.5.3).

A block diagram of the electronics involved in the time flight method is shown in Fig.III.11. A very important problem is impedance matching, which is always needed for the detector and also for the generator, if a tunneling junction is used and not a fluorescence film. As both the output impedance of the pulse-generator and the input impedance of the pulse amplifier are 50 Ω, we have to match this impedances to the low impedance (< 1 Ω) of the superconducting junction (50 Ω impedance junctions are excluded because the junction response time - as calculated from the equivalent resistor and capacitor in parallel - becomes too large.

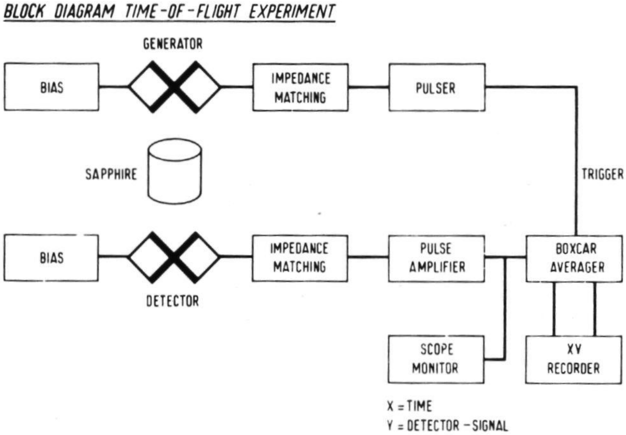

Fig.III.11 Block diagram of a time-of-flight experiment, which gives the detector signal against time.

for submicrosecond detection). Unfortunately, at liquid He temperatures no suitable transformer material is available (46); all ferrites suffer from a severe decrease in the permeability. Therefore, the impedance matching has to be done at room temperatures outside the cryostat. A low impedance cable (strip-line) was made of printed circuit material, which consists of two thin copper layers (80μ thickness) separated by a polyamide insulator (30μ thickness). This cable, which guides the pulses to the top of the cryostat, was mounted as near as possible to the sample with the help of short superconducting leads. Outside the cryostat, a resistor of 1 Ω in series with the secondary of a pulse transformer was used to terminate the strip-line. The self-made pulse transformer (50) was a small ferrite core with diameter of 10 mm; the primary was made of 21 windings of Cu-wire, the secondary consisted of three layers of Cu-foil, covering the primary completely and thus enhancing the coupling between the two. (When a fluorescence film was used as generator, no impedance matching was needed because the constantan film could be made directly 50 Ω by controlling the evaporation). Apart from the strip-lines, all leads in the cryostat were made of miniature 50 Ω coaxial cable (47).

On the other two terminals of the junctions, a DC-current bias could be superimposed. The detector junction is operated at a bias voltage of about 0.8 mV ($\approx$ 1,5Δ, which leads to voltage pulses for the detection of phonons. After impedance matching, these pulses are amplified through a very wide-band, low-noise pulse preamplifier (48). Further amplification (in total typically up to 70 dB) followed and the resulting pulse was fed into the boxcar integrator (45).

Electromagnetic crosstalk from the generator directly into the detector circuit gives the exact moment, when a pulse was shot into the crystal, but it can cause severe problems. Both the leading edge and the trailing edge of the input pulse cause their own ringing. If the 'ringing' persists for a long time, the detector pulses will be obscured. By adjustment of the rise- and fall-time of the pulse, (typically $\lesssim$ 50 nsec) the two effects can be compensated. In addition proper grounding is very important, as is the way in which the superconducting leads from the sample to the strip-line, i.e. the current loop of the generator circuit should be as far away as possible from the current loop of the detector circuit.

(ii) The 'modulated DC' method.

In this method, a variable DC bias is applied to the generator. junction with an AC current modulation superimposed. The modulation current has an amplitude of typical 25 mA and the frequency was 100 Hz. The detector bias voltage is again at 0.8 mV (as in (i)), the impedance matching is accomplished by the strip-line in series with the primary of a commercial low-impedance transformer-coupled preamplifier (49). The detector signal is then fed into a lock-in amplifier.

The DC bias current of the generator is slowly swept from zero to a current value which corresponds to $I \gtrsim I(6\Delta)$, while the AC current amplitude remains constant. Since only pulse signals from the detector are amplified, the DC background of phonon radiation does not show up in the output of the lock-in amplifier, which is tuned to the frequency of the modulation current. In terms of the semiconductor model (cf. Fig.III.4) this experimental condition roughly corresponds to the injection of a constant number of quasi-particles in the range of maximum energy, the latter being determined by the bias dependent DC voltage drop across the junction. In this way, the output of the lock-in amplifier is equal to the derivative of the detector signal with respect to the generator DC current. The slowly swept DC generator current is fed to the X-axis of the X-Y recorder, as shown in the block diagram Fig.III.12.

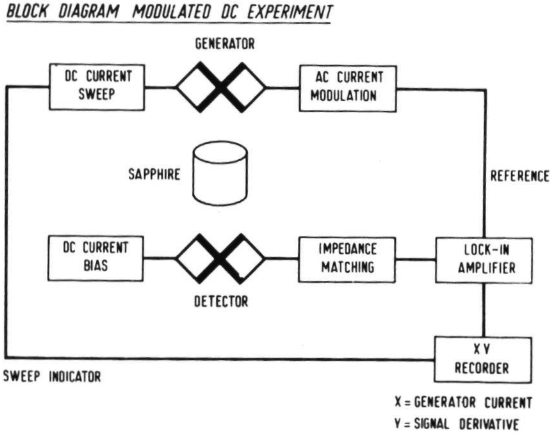

Fig.III.12 Block diagram of the modulated DC experiment, which gives the derivative of the detector signal with respect to generator current.

When the generator consists of a fluorescence film, one is limited to (i); when the generator is a superconducting tunnel junction both methods are in principle possible but it depends on the experimental situation which method should be used. In general, (i) is excluded for thin samples ($\approx$ 1 mm), because the velocity of sound for most samples is of the order of 10^6 cm/sec and this means that detector pulses would be obscured by ringing (for an input pulse of 100 nsec width, the crosstalk lasts for $\approx 0.5\ \mu$sec). For long samples, both methods can be used. It has to be noted that (ii) does not distinguish between the different phonon modes (longitudinal and transversal). Therefore, if one is interested in differences in the behaviour of such modes, one is limited to (i).

Apart from the experimental situation, it is our experience that method (ii) is more sensitive compared to (i). The limiting factor is set by the possible overall heating of the system by the slowly swept DC generator current, which quite easily may be $\gtrsim$ 1A for a low impedance junction. The heating would alter the I-V characteristic of both the generator and the detector. Therefore, if a high injection rate of quasi-particles is needed in the generator, one is limited to (i), which injects high power levels for short periodes of time without heating the entire system up.

III.5.3 A local magnetic field

In order to do real phonon spectroscopy, one should be able to tune the frequency of the phonons by some external means. One of the methods which can be used to alter in a reproducible way the energy gap of a superconductor and thereby changing the frequency of the emitted recombination phonons is to apply a magnetic field parallel to a thin film (20). In our experiments (cf. III.6), the generator and the detector are usually at distances of 25 mm apart from each other. Thus, in order to vary the gap of either the generator or the detector, without varying the gap of the other, we need a magnetic field which falls off from a certain value (typically of the order of 15 kG, the critical field of a thin film superconductor in a parallel field) down to zero within 25 mm.

We constructed a magnet with a diameter of 50 mm(in order to fit into the dewar) with a closed mild steel core, in which a cylindrical bore of diameter 10.8 mm is drilled. The interior consists of two coned pole pieces with a cone angle of 60° leaving a gap of 11 mm wide and 9 mm long inside the magnet, where the magnetic field should be reasonable uniform for our purpose. A schematic view and a photograph of this magnet is shown in Fig.III.13. Coils of superconducting wire (Ref. 11 of Chapter I) are carefully wound around the two coned pole pieces. Each coil consists of 300 layers. Note that the coils are also conical shaped at the inner diameter.

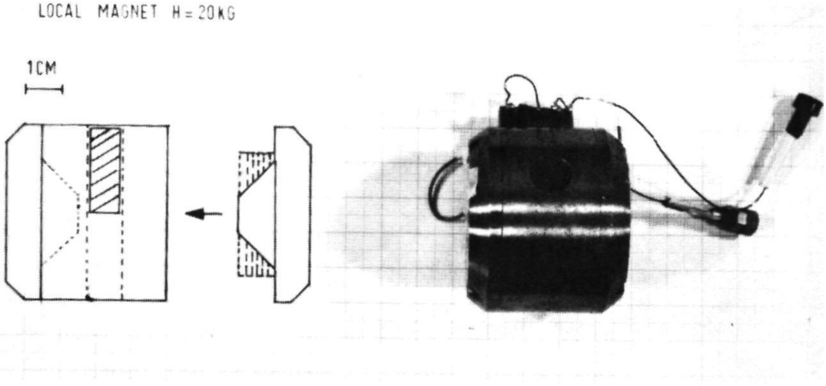

Fig.III.13 The magnet used to produce a local field in the area of either the generator or the detector. The maximum field at the centre was 20 kG. The diagram on the left shows one of the two pole-pieces with its coil removed from the core, which contains a cylindrical crystal of diameter 10 mm and length 25 mm. The photograph on the right shows the assembled magnet with superconducting leads.

When due to some accident the superconducting coils should become normal, the dissipated power would cause rapid evaporation of the helium inside the magnet. Therefore, to enable exhaust of the gas, the coils are only partially impregnated with varnish. The flat polished surfaces of the core, and the two halves with the pole pieces are held together via screws in combination with springs.

The calibration of the magnet was accomplished with a special miniature low temperature InAs Hall probe with a sensitive area of 3x1.5 mm (51). The maximum field which can be maintained without quenching is ≈ 20 kG.A typical magnetic field profile for a current through the coil of 4A (which gives a maximum field of 15 kG) is shown in Fig.III.14. The field is reasonable flat with-

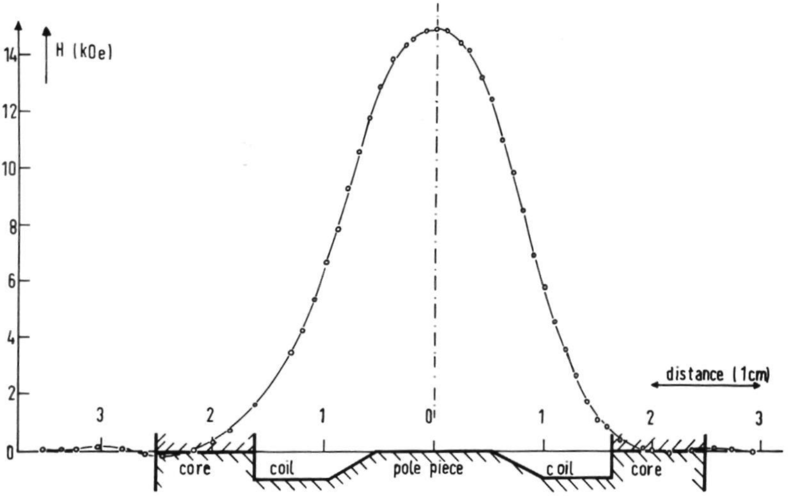

Fig.III.14 The magnet field profile along the axis of the cylindrical bore of the magnet core (Fig.III.13). The geometry of the magnet is indicated below.

in 2 mm in the centre of the gap between the pole-pieces. Note that the magnetic field goes through zero just within the core. The ideal situation would therefore be to have one film of the sample at the centre and the other one at the zero field position. We were unable to detect any component of the magnetic field in the longitudinal direction with our transverse Hall probe. Such a component would however immediately show up in the tunneling experiments as thin superconducting films are very sensitive to perpendicular magnetic fields. We have seen no effect in the derivative of a tin SS junction placed 1 mm within the core.

III.6 Experimental results on sapphire and ruby

In this Chapter, we will describe results on monochromatic phonon transmission through sapphire and ruby. The experiments on sapphire have been performed with the time of flight method and the modulated DC method (see III.5.2) The transmission through ruby is investigated with the phonon fluorescence generator and an attempt is made to tune the frequency of the generated phonons by applying a magnetic field (see III.5.3).

III.6.1 Monochromatic phonons in sapphire

Sapphire (Al_2O_3) is a dielectric solid with a high thermal conductivity (52); in a very pure sample it is possible that the phonon mean free path Λ of the phonons is mainly determined by the sample dimensions so the phonons will flow right through. In order to be sure that the available samples are of sufficient quality, the crystals were investigated by X-ray topography which revealed some internal stress inside the crystal (53). In addition a conventional heat conductivity experiment was carried out at 1 K in order to measure the phonon mean free path Λ directly.

If the temperature is well below the Debye temperature Θ_D, the thermal conductivity λ of a crystal is given by Casimir's relation

$$\lambda = \frac{1}{3} C v \Lambda, \qquad \text{(III.2)}$$

where C is the specific heat and v is the velocity of sound. At liquid He temperatures, in Al_2O_3(Θ_D = 900 K) only phonons with small $\vec{k}$-vectors are present; therefore Umklapp-processes can be neglected and the mean free path of the phonons is limited by impurities and boundary scattering:

$$\Lambda^{-1} = l^{-1}_{\text{imp}} + d^{-1}, \qquad \text{(III.3)}$$

Here d is the crystal diameter and l^{-1}_{imp} is the mean free path due to impurity scattering alone. The temperature dependence of λ is then given by the dependence of C only, which goes as T^3 for a Debye-insulator. Using the known literature value for C we get from our conventional heat conductivity experiment for a cylindrical crystal with a diameter d = 10 mm and a length L = 20 mm, an impurity limited mean free path of the order of 10 mm (54). Therefore, phonons generated at one side of a sample with L ≈ 10 mm should reach the detector without being scattered, except on the walls.

If we consider a sapphire crystal with two identical evaporated tin tunnel junctions opposite to each other, we have then in essence a monochromatic system: the generator emits phonons of energy 2Δ and a lower energy tail of relaxation phonons (cf. III.2.1) and the detector is only sensitive to phonons with $\hbar\omega \geqslant 2\Delta$. When using the time of flight method, the pulse width used at the generator and must be wide enough to establish a steady state situation which gives a lower limit to the pulse width of 10^{-7} sec. The upper limit is given by the transit time of the different polarization modes of the phonons through a given sample. As longitudinal and transversal phonon have different sound velocities, they are separated in the crystal and will reach the detector at different times. In order to separate well the longitudinal from the transversal phonon pulses at the detector, the generator pulse width should be smaller than $5x10^{-7}$ sec. for a c-cut crystal of 5 mm long; here we have used the low-frequency ultrasonic sound velocity data for a sapphire along the c-axis (54).

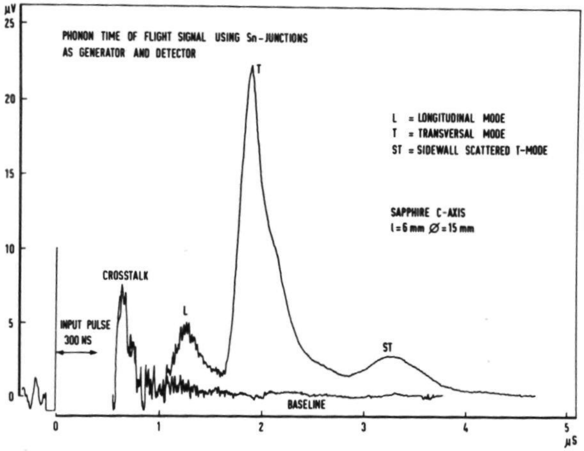

Fig.III.15 Detector signal showing the separation of the phonon modes after transmission through a sapphire crystal.

For an input pulse of 300 nsec width, a typical resulting detector signal versus time is shown in Fig.III.15 . The beginning of the direct electromagnetic feedthrough ('crosstalk') coincides with the very moment at which the electrical pulse is injected at the generator which marks the zero of the time base. After transmission through the crystal (6 mm long) longitudinal and transversal phonon pulses are detected. A baseline is indicated, corresponding to the response of the detector circuit at zero detector bias. For the velocities, one gets

$$v_l = (1.18 \pm 0.03) \times 10^6 \text{ cm/sec}$$

for the longitudinal mode, and

$$v_t = (0.79 \pm 0.02) \times 10^6 \text{ cm/sec}$$

for the transversal mode. These results agree within 3% with previously published low frequency data (55). It should be noted that for sapphire, the transverse waves are degenerate with respect to the relevant crystal orientation (c-axis). (If the cylindrical axis coincides with the a-axis, a fast and a slow transverse wave can be observed). In addition to the longitudinal and the transversal mode a broadened pulse with a maximum at 3.2 μsec can clearly be seen. This is due to diffusively scattering of the transverse mode at the fine-ground side walls of the crystal. A similar but much weaker effect due to diffusively scattering of the longitudinal mode can barely be seen in the trailing edge of the transversal pulse. Due to the severe mismatch between film and sample, both at the generator and at the detector end, and due to some scattering at impurities or lattice defects, it can not be expected, that the rectangular input pulse is reproduced as such in the detector pulse (56).

A striking feature of the detector signal is the much weaker longitudinal mode compared to the transversal mode. We found experimentally that the amplitudes of the longitudinal mode (L) compared to the transversal mode (T) goes roughly as a function of the sound velocities in the crystal, i.e.

$$L/T \cong \frac{1}{v_l^2} \Big/ \frac{2}{v_t^2} \qquad \text{(III.4)}$$

For the detector signal of Fig.III.15 we find L/T = 0.23, whereas $(1/v_l^2)/(2/v_t^2)$ gives 0.20. The ratio was different for one given sapphire crystal and different generators and detectors (i.e. different thickness and impedance). It is difficult to distinguish in L/T the contributions of generator, sapphire and detector.

Since phonon detection is possible only for phonon energies exceeding the gap energy, a voltage dependence of the generator spectrum as expected for relaxation phonons can be seen by measurements of signal amplitude as a function of generator voltage. To investigate this we apply the sensitive modulated DC method described in III.5.2. In Fig.III.16 two curves are simultaneous-

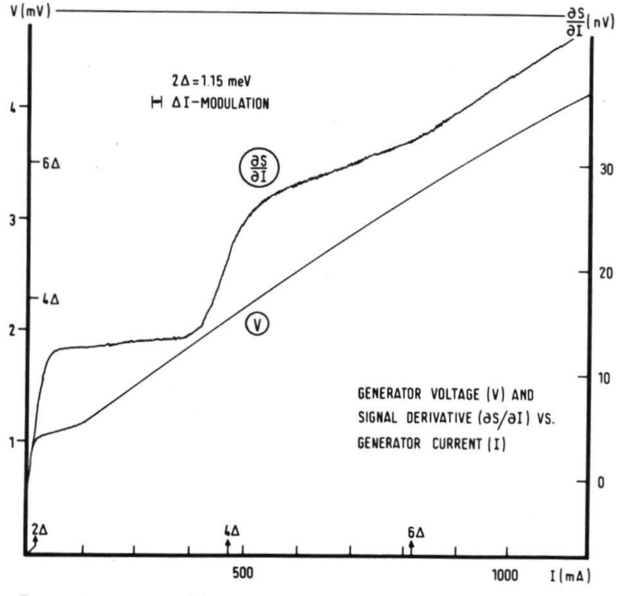

Fig.III.16 The generator voltage (V) and the derivative of the detctor signal (∂S/∂I) versus the generator current (I) in a sapphire crystal. Note the steps at 4Δ and 6Δ.

ly plotted, namely the current-voltage characteristic of the generator, and the dependence of the derivative of the detector-signal (with respect to the generator current) against generator current. Arrows on the horizontal current axis indicate the values for which the bias voltage is 2Δ, 4Δ, and 6Δ. Distinct kinks in the $(\partial S/\partial I)$ curve for multiples of 2Δ can be seen, which are intimately related to the quantum behaviour of the generator and the detector. At $V < 2\Delta$, the signal is due to recombination phonons of thermally excited quasi-particles in the generator. For a voltage $2\Delta < V < 4\Delta$, the signal is linearly rising ($\partial S/\partial I$ is constant) as V is exceeding the range of thermally excited quasi-particle tunneling, and the rate of recombination phonon emission is directly proportional to the single particle tunneling current. The additional rise at $V = 4\Delta$is due to the voltage dependence of the upper energy limit for relaxation phonons, i.e. $\hbar\omega_{max} = V-2\Delta$; if $V \geqslant 4\Delta$, relaxation phonons contribute also to the detector signal as relaxation phonons of energies $\geqslant 2\Delta$ are emitted. As pointed out in III.3.1, there are twice as many relaxation phonons as recombination phonons - after relaxation of a quasi-particle, another quasi-particle is needed to recombine and emit a recombination phonon. The relative step height at 4Δ agrees reasonably well with the theoretical value of two.Theoretical investigations (1), (34), (57) show that the step should actually consist of a narrow singularity, which reflects the BCS density of states at the gap edge. Unfortunately, our experimental conditions are not appropriate enough to investigate this singularity in detail:the temperature of 1.2 K we work at is not low enough, which means that there are still too many thermally excited quasi-particles present; in addition, the modulation current as indicated in Fig. III.16 gives certainly some smearing out of any detailed structure. In the bias range $4\Delta < V < 6\Delta$, the slow continuous rise of the detector signal is due to reabsorption of phonons with $\hbar\omega > 2\Delta$ within the generator, which ultimately yields additional 2Δ recombination phonons. For $V > 6\Delta$, additional channels for the emission of 2Δ phonons are opened as it becomes energetically possible to produce two relaxation phonons of energy 2Δ. This increased signal is reflected in the rise of $(\partial S/\partial I)$ at $V = 6\Delta$.

A similar curve for another junction is shown in Fig.III.17.

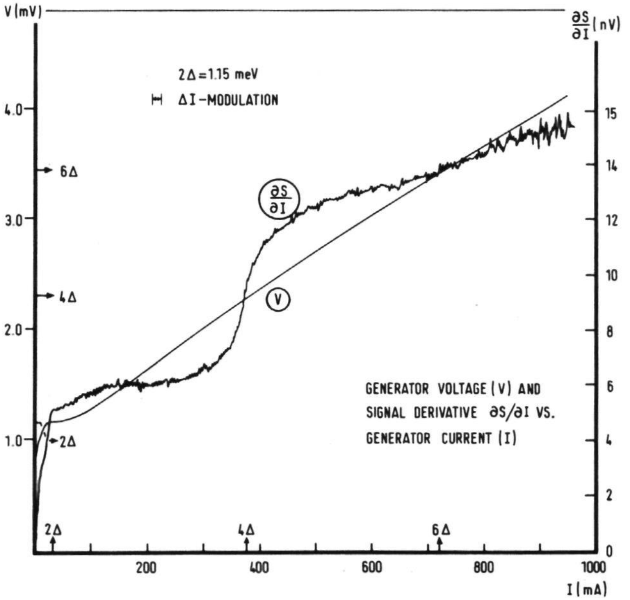

Fig.III.17 The same plot as in Fig.III.16 for a different junction, with a barely visible local maximum in $(\partial S/\partial I)$ at $eV = 2.3\Delta$ (see text).

A barely visible local maximum is seen in the region $2\Delta < V < 4\Delta$. It might be possible that this is due to recombination of quasiparticles just above the gap of the generator, leading to a finite width of the recombination phonon peak (cf. III.2). Theoretical investigations (5) show that a local maximum in the detector signal beyond $I = I(2\Delta)$ should occur, due to the enhanced probability of recombination compared to relaxation for levels just above the gap. Assuming this model, our recombination peak would have a width of $(2.3-2)\Delta = 0.3\Delta$. We would like to emphasize once again that the behaviour of the detector can certainly not be understood with the assumption of a black body generation of phonons (i.e. a spectrum which obeys a Planck distribution). The above measurements strongly indicate the quantum behaviour of tunnel junctions as generators and detectors of monochromatic phonons.

III.6.2 Monochromatic phonons in ruby

We will now consider the propagation of monochromatic phonons through ruby. Instead of using a tunnel junction as generator, a fluorescence film was employed. With the 'time of flight method', we get a similar curve as Fig.III.15 which is shown in Fig.III.18. The sample was a cylindrical ruby of 0.01 Cr% (atomic percentage) and the cylindrical axis made an angle of 30° with the c-axis; the length is 25 mm and the diameter 10 mm. Unfortunately, there are no previously published data of the sound velocities for ru-

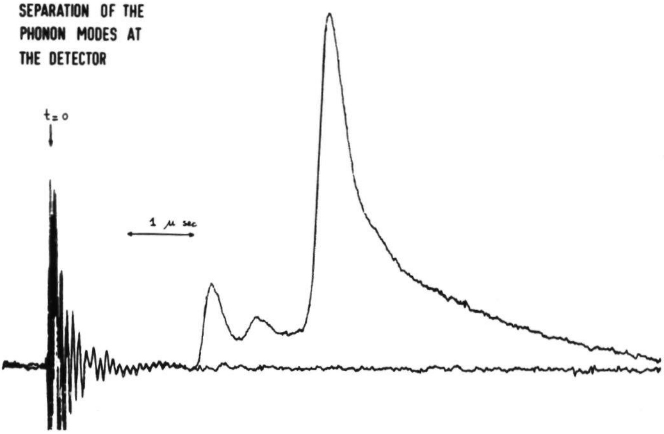

Fig.III.18 A similar plot as in Fig.III.15 for a ruby crystal as written on the x-y-recorder.

by for this crystal orientation. Note that because the transverse wave is not degenerate in this direction, a weak fast transverse pulse is observed followed by a strong slow transverse wave. From the experiment, the calculated velocities are:

$$v_l = (1.10 \pm 0.04)\times 10^6 \text{ cm/sec}$$
$$v_{t,f} = (0.77 \pm 0.04)\times 10^6 \text{ cm/sec}$$
$$v_{t,s} = (0.57 \pm 0.02)\times 10^6 \text{ cm/sec}$$

Another difference from the results on sapphire is the long tail in the trailing edge of the slow transversal wave, where one may suspect the appearance of two kinks. As opposed to the case of sapphire, the walls of the ruby sample are highly polished, so specular reflection of phonons at the walls is more likely than diffuse scattering. This then would tend to give contributions to the received signal in the trailing edge, as the transit times of the phonons involved are slightly higher (≈ 4%) after being reflected against the wall (only reflections in the mid-region of the crystal will contribute).

III.6.3 Frequency tuning of monochromatic phonons

The problem of the behaviour of a superconducting film in a parallel magnetic field H was first considered by Ginzburg and Landau (58) in terms of a phenomenological theory for the 'order parameter' ψ. They showed that if the thickness d of the film is less than the London penetration depth λ, then the order parameter goes continuously to zero as the field is increased, going through a second order phase transition at the critical field H_{cf}. If, on the other hand $d > \lambda$, then ψ decreases continuously to a critical value ψ_c (which may also be a function of the position within the film) at which point it abruptly drops to zero in a first order phase-transition. Gorkov (59) rederived the phenomenological results from the microscopic theory of superconductivity and showed that under certain conditions the order parameter ψ is proportional to the energy gap Δ of the BCS theory.

The complicated problemof a full and explicit theory of superconductors in the presence of a time-reversal breaking interaction (thin films in parallel magnetic field, exchange field of Pauli terms, magnetic impurities, type II superconductors close to H_{c2}, proximity effects etc.) has been attacked first by Abrikosov and Gorkov (60) and then has been solved in full glory by Maki (61). It was shown that a magnetic field can cause 'gapless' superconductivity, i.e. the order parameter remains finite over a certain region of fields and at finite temperatures, while the energy gap gets smaller and smaller and finally being zero with superconductivity still present. For dirty films, this gapless situation starts at a field H_{gl} given by $(H_{gl}/H_{cf})^2 = 0.91$. In addition, the density of states is no longer BCS-like but broadens out in a manner shown in Fig.III.19, where theoretical curves of the density of states are plotted as a function of energy for thin films in a parallel magnetic field for several values of the electronic mean free path (20). The behaviour of superconducting films according to this model has been quantitatively verified by Millstein and Tinkham (62). For our purpose, it is sufficient to use the fact that Δ(H) decreases monotonically with the applied magnetic field. It is important to note that even in the dirty limit the gap edge remain reasonably sharp and decreases monotonically (cf. Fig.III.19). The maximum in the density of states remains close to the zero-field BCS-value. Thus, the phonons which are 'converted down' by a dirty superconducting fluorescence film may still possess a reasonably well defined frequency peak.

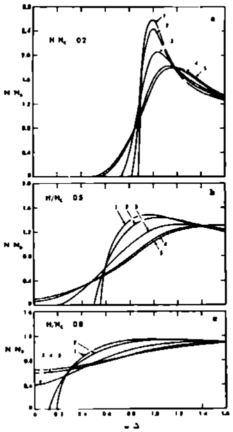

Fig.III.19 The calculated density of states of a thin film in a parallel magnetic field as a function of energy for several values of the electronic mean free path l (ξ_0 is the coherence length) [1:l = 0,2 l = $(\pi/10)\xi_0$, 3 l = $\pi\xi_0$, 4:l = $10\xi_0$, 5:l = ∞](20).

In order to investigate the tuneability of the generated phonons, we mount the ruby crystal with a fluorescence generator inside the local magnet (cf. III.5.3).The detector tunnel junction (Sn) is positioned at zero field, while the fluorescence generator (Sn) is placed at maximum field which is then positioned parallel with the fluorescence film. Our fluorescence film has a thickness $d \approx 1200$ Å $(d > \lambda)$, which means that by applying a magnetic field, the order parameter $\Delta(H)$ is first monotonically reduced to a value $\Delta(H_c) < \Delta_{BCS}(H = 0)$, and then abruptly jumps to zero in a first order phase transition during which the superconducting film becomes normal. The critical field H_c of the fluorescence film was determined electrically with a two point DC experiment and was found to be 1.4 kG, which is reasonable for a film of this thickness in a nearly parallel magnetic field.

From the theoretical calculation (63) it is to be expected that for such a film, the order parameter decreases slowly as a function of the applied magnetic field up to about $H/H_c \approx 0.7$, and then goes rather rapidly to zero at H_c. This means, that the order parameters of the generator and detector are no longer equal as soon as the magnetic field is applied to the fluorescence film. This 'detuning' will become noticable at around $H/H_c \approx 0.7$, and at $H/H_c \geqslant 1$, the fluorescence film will be normal, the phonons will no longer be 'monochromatic' but distributed thermally in frequency according to Planck's law.

This behaviour can qualitatively been seen in Fig.III.20. Up to around 1 kG $(H/H_c \approx 0.7)$, the detector signal is only slight-

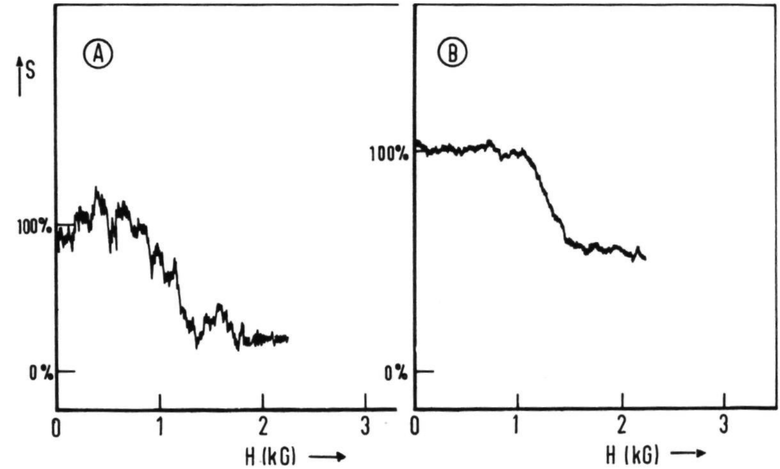

Fig.III.20 The detector signal of the transverse phonon mode as a function of the local magnetic field on the fluorescence generator (see text). (A) Input power on the generator is 0,5 mWatt, (B) input power on the generator is 2 mWatt.

ly reduced, while between 1 kG and 1.4 kG ($H/H_c \approx 1$) it goes down drastically, and above 1.4 kG it stays constant. The ratio of the detector signal for monochromatic phonons ($H = 0$) to the signal with thermal phonons ($H \geqslant H_c$) will obviously depend strongly on the input power into the generator: if this power is low (Fig. III.20(A)), very few thermal phonons will be present for which $\hbar\omega \geqslant 2\Delta$, and if this input is high (Fig.III.20(B)), the fraction of thermal phonons will be appreciable.

To our knowledge, this 'tuneable' phonon generation experiments are the first unambiguous proof, that a fluorescence film in combination with a tunneling junction can be used as quantum generator and detector for phonons.

III.7 Phonons and heat pulses in Helium

III.7.1 Introduction

The generation and detection of heat pulses in He^4 in the liquid as well as in the gas phase has received considerable interest over the last couple of years (64), (65), (66), (67), (68), (69). The problem of heat transfer between a solid and liquid Helium (Kapitza resistance) is still basically unsolved, and the exact form of the excitation spectrum of HeII is one of the most attractive subjects to be investigated with ultra high frequency phonons because of the fact that the theory still lacks experimental evidence (70), (71).

Unfortunately, in the vapour pressure range of liquid He, the phonon mean free path Λ in the liquid He is very small; at 1 K one gets $\Lambda \approx 10^{-5}$ cm. For larger mean free paths one has to work at ultralow temperatures which usually needs the aid of dilution refrigerators. Around 0.4 K the phonon mean free path is rapidly increasing, reaching a value of a few mm at o.1 K. Below that temperature, phonons should propagate purely as ballistic phonons with velocities determined solely by the dispersion relation, independent of the temperature. Above 0.1 K, due to collisions, the phonons will be thermalized and the velocity is a function of both the phonon generator energy and the temperature. It should be noted that in the superfluid HeII, temperature variations can propagate in the form of second sound.

From the discussion above, it is clear that at temperatures of ≈ 1 K ballistic flow of phonons is excluded. Very recently, ballistic flow of phonons in HeII has been observed at 0.1 K (70), while ballistic flow of 'hot' He atoms in He^4 gas was observed earlier and starts below 0.5 K (75).

In order to investigate the behaviour of heat pulses in He, experiments were initiated to generate and detect heat pulses with the aid of small metallic heaters as generators and superconducting tunnel junctions as detectors. This gives a considerable improvement in the interpretation of experimental results as the fast risetime and small dimensions of the generator and the detector enables the use of short pulses and small distances between generator and detector. In older experiments, (72), (73), (74), where much slower and larger carbon generators and detectors were used, results were sometimes dubious because of the specular and diffusive reflections of phonons at the walls of the sample chamber.

III.7.2 Secound sound propagation in HeII

In our experiments in liquid HeII at 1 K, we observed second sound propagation, which is a travelling temperature fluctuation (76). The geometry used for the study of propagation of second sound (as well as for shock waves (cf. III.7.3)) is shown in Fig. III.21. This set up looks similar to the experimental situation of III.6; the dielectric crystal is replaced by liquid HeII or

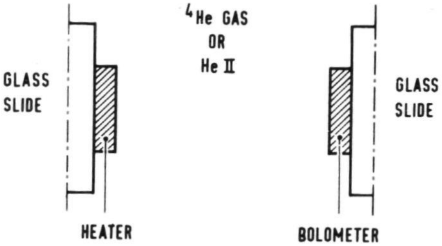

Fig.III.21 Geometry for shock wave-propagation in He-gas and second-sound-propagation in He II.

He^4 gas. When we apply a rectangular pulse of 260 nsec width and 0.2 $Watt/mm^2$ energy in the constantan heater, a temperature fluctuation is generated which propagates with the second sound velocity. The tunnel junction, acting as a bolometer, detects the increase in temperature and this results in voltage pulses for a constant current biased junction. The 'time-of-flight' method as described in III.5.2 was used to generate and detect the pulses.

A typical response signal of the detector is seen in Fig. III.22. A second sound pulse is seen at approximately 30 μsec. With the distance d = 0.23 cm between heater and junction, this corresponds to a velocity of 20.3 m/sec at 1.7 K, in agreement with previously published data (72), (76). At multiples of the second sound pulse, several echos can be observed.

The detector pulses have a very specific shape which most clearly can be seen from the second sound echo at 150 μsec. Two distinct pulses with opposite sign are visible. If we would make the input pulse broader the two pulses would already show up in

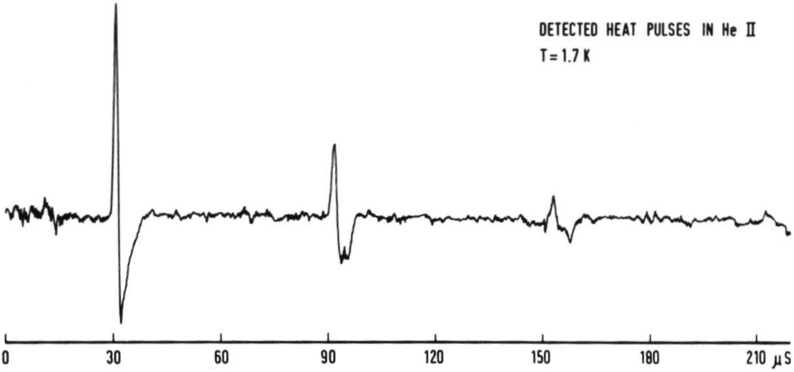

Fig.III.22 Second sound-pulses in He II. Note the echos.

the second sound pulse, as for example can be seen in Fig.III.24 of III.7.3. The shape resembles the time derivative of the rectangular input pulse. This is a well known effect in transmission of second sound pulses through HeII (77); we will show in III.7.3 that it exists equally well in the gas phase. Following (77), we have for the driven wave equation for second sound in first order approximation,

$$\nabla^2 T' - \frac{1}{c_2^2} \frac{d^2}{dt^2} T' = - \frac{1}{\rho C c_2^2} \frac{d}{dt} P. \qquad \text{(III.5)}$$

Here, T' is the disturbance of the temperature from an equilibrium temperature T, ρ is the density, c_2 is the second sound velocity, $C_p \approx C_v = C$ is the specific heat for HeII and P is the power dissipated in the point heat source. The solution of (III.5) in an <u>unbounded</u> region is given by

$$T'(\vec{r},t) = \int_0^{t^+} dt' \int d\vec{r}' [\frac{d}{dt} P(\vec{r},t')/4\pi\rho C c_2^2] \times$$

$$\times [\delta\left(t-t'-(|\vec{r}-\vec{r}'|/c_2)\right)/|\vec{r}-\vec{r}'|]. \qquad \text{(III.6)}$$

Hence it follows that the signal is proportional to the time derivative of the power input. It can be shown (77) that in the case of reflecting walls, the detector pulse is similar in shape to the input pulse and not to this derivative - due to the large dimensions of the sample holder, carbon generator and detector the observed detector pulses in older measurements were rectangular (72), (73), (74).

III.7.3 Explosion of a Rollin film

The superfluid HeII is known to form a thin creeping film going upwards from the bath on walls, pumping tubes etc.. This film is known as the Rollin film (76). For a vertical creeping film, a thickness of 200 Å is given in literature (76), while the creep velocity is of the order of 30 cm/sec (76).

During the experiments on heat pulse propagation in liquid HeII, we observed a very interesting effect due to the explosion of a Rollin film. As the HeII level gets lower, the moment is reached at which the lower end of the heater and the detector get just out of the HeII bath. But there is still a creeping superfluid film of the HeII covering the generator and the detector. By applying a pulse to the generator, the dissipated heat will evaporate partly or totally the superfluid HeII film. The evaporated 'hot' He atoms will propagate with a velocity determined by the energy contained in the generator pulse. When the 'hot' He-atoms arrive at the detector, the kinetic energy of the He-atoms will be dissipated in the HeII film covering the junction, thereby raising the temperature which results in a voltage pulse in a similar way as in III.7.1 (again the 'time-of-flight' method was employed). If the pulse repetition frequency is not too high the generator can recover and the HeII film is restored. Note that doubling the pulse amplitude has the same effect on the dissipated energy of the heater as broadening the pulse width with a factor 4.

A typical detector pulse is shown in Fig.III.23 for an input energy of 0.17 Watt/mm^2 in the heater. We note that the velocity in the gas phase is larger than the velocity of the second sound pulse. As in the case of second sound, the detector pulse consists in fact of two pulses with opposite sign, but due to a large overlap this effect is obscured. If we make the pulse broader, the two pulses are effectively separated as in Fig.III.24. In

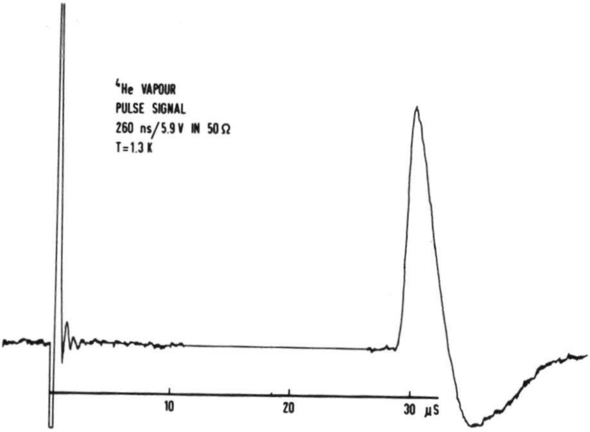

Fig.III.23 A typical detector-pulse caused by the arrival of a shock wave in He-gas.

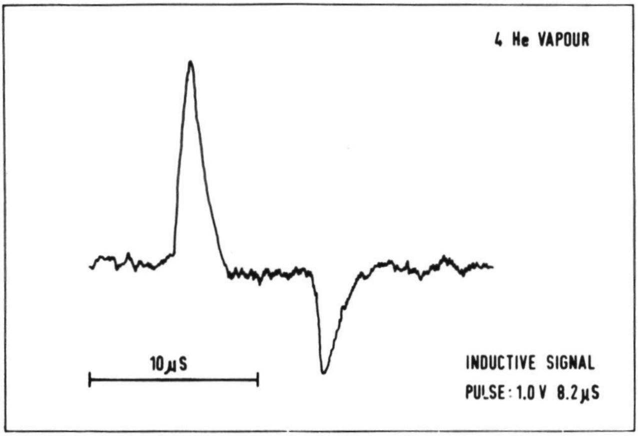

Fig.III.24 The inductive effect in the detected pulses (see text).

analogy with the second sound pulses (see III.7.2), this can be understood in terms of a driven wave equation. Here, we have a rapid evaporation of a Rollin film and therefore an injection of atoms in the ambient vapour. If M is the injected mass, p' the resulting disturbance of the pressure and c_1 the ordinary sound velocity, the appropriate wave equation is in analogy to (III.5) given by

$$\nabla^2 p' - \frac{1}{c_1^2}\frac{d}{dt^2}\, p' = -\frac{d}{dt} M. \qquad \text{(III.7)}$$

Under the usual isentropic conditions for sound, a temperature disturbance T' given by

$$T' = \frac{p'}{C_p \rho} \qquad \text{(III.8)}$$

will accompany the pressure pulse making it 'visible' to the junction which is used as a detector. The signals to be expected from a square input pulse of atoms will then be identical in form to those present in second sound. As (III.6) is a solution for an unbounded region, the observed pulse shape in Fig.III.24 is a proof that we do not have wall reflection in our experimental geometry (cf. Fig.III.21).

When the repetition frequency of the generator gets too high, the helium film will not be able to cover the generator again entirely within the time between two pulses. Thus, by raising the frequency, a limit will be reached above which the amplitude of the detector signal will decrease. From this limit and the heater dimensions (1.5 x 1.5 mm) the recovery speed of the film can be calculated. It is found to be 39 cm/sec,so it is roughly the same as the creep speed of 30 cm/sec (76).

By increasing the amplitude of the applied electrical pulse, more and more of the HeII film will be evaporated during the pulse. Eventually, the dissipated power is high enough to explode the entire film within the pulse period. From thereon, the detector signal will not rise any further. This saturation behaviour occurs in our geometry for an input energy of E_c = 2.82 erg. Assuming that the heat of evaporation is the same as that for the bulk liquid (i.e. 82 J/mol), it is possible to calculate the thickness of the Rollin film from E_c and the known dimensions of the heater. The thickness found in this way is 240 Å. This must be considered as an upper limit, because not all of the energy is necessarily dissipated in the film; yet this agrees reasonably well with the literature value of 200 Å for a vertical Rollin film (76).

III.7.4 Shock waves in He gas

Shock waves have been thoroughly treated in literature (78). When in gases the velocity of the gas becomes comparable or exceeds the velocity of sound, effects due to the compressibility of the gas become of prime importance. If the velocity v is greater than the sound velocity c (supersonic region), a discontinuity in, for example, the density, can propagate as a shock wave. A strong shock wave can cause a considerable increase in temperature. In a shock wave the velocity varies as the square root of the pressure behind the wave front, and increases with increasing energy. The form of the shock wave is a steep leading edge with a relatively slowly decaying trailing edge.

When the Rollin film is heated (cf. III.7.3) with a low energy ($\lesssim 0.1$ erg), it can be assumed that the film will evaporate slow-

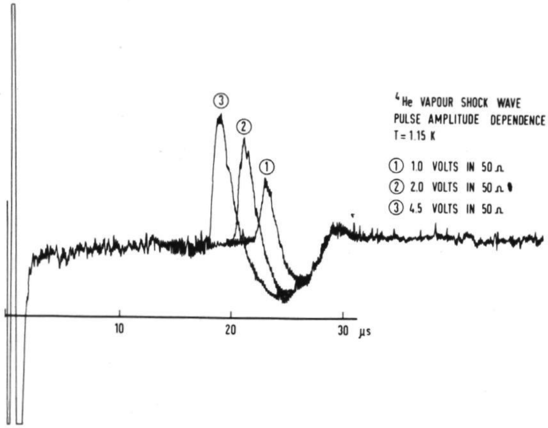

Fig.III.25 The increase of the velocity of the shock wave as a result of higher input power at the generator.

ly. In that case, the velocity distribution of the propagating He atoms corresponds to a Maxwell-Boltzmann distribution (79), (80), with a maximum velocity v_m of the gas atoms. However, for energies one order of magnitude higher ($\gtrsim$ 1 erg), the velocity distribution gets more and more sharply peaked around the maximum velocity v_m (79), which is already found in experiments with carbon generators and detectors (75). In our experiments, using this sort of high input energies, we were able to detect unambiguously pulses with the typical shape indicating shock wave propagation, as shown in Fig.III.25. We can recognize the sharp rise and the slowly decaying tail, in sharp contrast to triangular second sound signals (cf. Fig.III.22). Even more striking is the increase in the velocity if the power into the heater is increased. Thus we believe to have proved experimentally that the density fluctuation propagating with a velocity greater than the normal sound velocity, c_1, behaves like a shock wave. We will illustrate and summarize the typical shock wave features, as detector pulse shape and the increase for higher input power in the heater, in four oscilloscope tracings in Fig.III.26 and 27. The input pulse in Fig.III.26 (A), (B) is the bright spot above the noise at the left of the display. For (B) the input amplitude is twice as high as in (A). Note the shorter travelling time of the pulse in (B).

In Fig.III.27 the saturation effect as discussed in III.7.3 is visible: for high enough energies, the amplitude and the velocity of the detected signal will not increase any more.

UPPER TRACE:
ARRIVAL OF SHOCK WAVE IN He GAS

LOWER TRACE:
VELOCITY INCREASE AT HIGHER ENERGY

Fig.III.26 Oscilloscope displays showing the same effect as in Fig.III.25.

UPPER TRACE:
SATURATION OF DETECTOR SIGNAL

LOWER TRACE:
FOUR ECHOS AFTER SHOCK WAVE ARRIVAL

Fig.III.27 Oscilloscope displays showing in the upper trace saturation of the detector signal (see text), and in the lower trace several echos of the shockwave.

Fig.III.28 shows the velocity and the amplitude of the shock wave as a function of the input energy. From this plot we clearly see the saturation effect in the velocity and the amplitude at roughly the same energy value $E_c = 2.82$ erg.

Below E_c there seems to be an almost lineair relation between the shock wave velocity and the square root of the input energy. This can be explained by assuming that the energy E is so high that E is proportional to T^4_{heater} (this holds for situations where $T_{\text{heater}} \gg T_{\text{ambient temperature}}$(1)). Hence the final temperature of the heater at the end of the pulse is given by $E^{\frac{1}{4}}$. For short pulses, the temperature reached by the He-film should be of the order

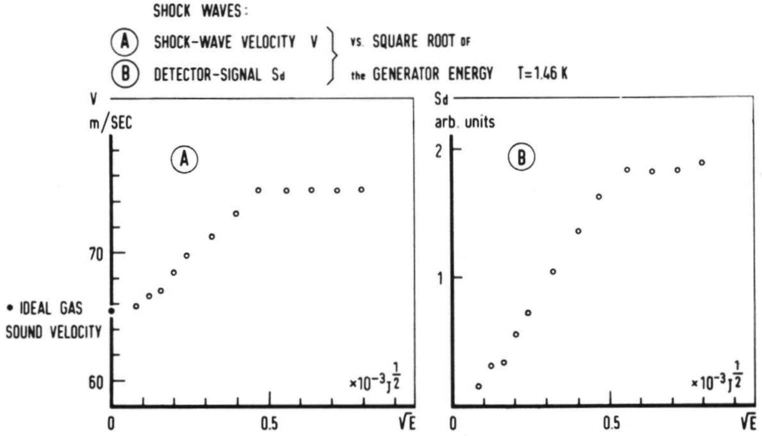

Fig.III.28 Shock waves in He-gas. (A) Shock wave velocity versus square root of the generator energy (B) detector pulse amplitude versus square root of the generator energy.

of the final heater temperature. Hence the kinetic energy of the atoms will be roughly proportional to $E^{\frac{1}{4}}$, which means that $v \propto E^{\frac{1}{2}}$, which is what we observe.

When the input energy E approaches zero, the shock wave velocity should approach the ordinary sound velocity c_1. From Fig. III.28 (A) we get at T = 1.46 K a sound velocity in the He gas of c_1 = 63 m/sec. Unfortunately, there are no reliable ordinary sound velocity measurements available at this temperature. In order to make a comparison, c_1 can be calculated assuming an ideal gas behaviour. For the propagation of an adiabatic wave, one has

$$c_1 = \left(\gamma \frac{kT}{m}\right)^{\frac{1}{2}}, \qquad \text{(III.9)}$$

where $\gamma = C_p/C_v$. For He one has $\gamma = 5/3$ and for T = 1.46 K one finds c_1 = 65.5 m/sec in striking agreement with the experimental results. In order to be sure that the above formula for the sound velocity is applicable, one has to be sure that one is within the hydrodynamic regime, i.e. $\Lambda \ll L$, where Λ is the mean free path and L is the distance between generator and detector. (L = 0.23 cm). From simple kinetic gas theory, one gets for the mean free path

$$\Lambda = kT/(2^{\frac{1}{2}}4\pi r^2 p) \qquad \text{(III.10)}$$

where r, the radius of the He atom, is roughly equal to 1.1×10^{-8} cm(75) and p is the pressure of the He bath with temperature T. At T = 1.46 K we find $\Lambda = 1.2 \times 10^{-4}$ cm, thus $\Lambda \ll L$ and our assumptions are justified.

It is interesting to note that our method is able to measure sound velocities at temperatures where the classical resonance methods can no longer be used because of the high losses involved at 1 K, as opposed to the situation at 4 K (81). Another method, based on Schlieren photography techniques, was used by Gulyaev (82) at temperatures of 1.3 K. He finds sound velocities which are slightly higher than the calculated values, but his method is intrinsically much less precise than ours.

To investigate the losses, we have also measured the attenuation. Two mechanisms are contributing to the decrease of the signal as a function of distance: energy dissipation in the shock wave front, and geometrical spreading of the wave front. Experimentally, the detector signal shows an exponential decrease as a function of the distance between generator and detector, with a characteristic decay length of about 3 mm (69). This exponential dependence on distance suggests a strong collimation of the shock wave. However, by studying experimentally the angular dependence of the propagation characteristics of the shock wave within a couple of degrees around the position with both generator and detector parallel, we are unable to make any conclusive statements.

III.8 A proposal for a phonon spectroscopy experiment

In order to investigate the feasibility of the quantum phonon generators and detectors described in this Chapter, and to use them for a real spectroscopic experiment, it would be interesting to find a medium where phonon induced transitions exist and where the energies involved are already known from other independent measurements.

Such a medium would be KCl doped with a small amount ($\approx 10^{18}$ cm^{-3}) of ^{6}LiCl. In this alkali-halide crystal, the K^+ ion is replaced by the much smaller $^6Li^+$ ion. From thermal conductivity experiments (83), (84) it is known that a dip in the curve of the thermal conductivity around 0.62 K can be well understood by assuming that the $^6Li^+$ ion is tunneling between eight potential minima in the <111> directions, with a frequency of about one hundredth of the Debye frequency of the host. In addition, it was shown (84) that the tunneling states undergo a stark effect; under the influence of an electric field $\vec{E}(/\!/<111>)$ the energy difference between the lowest energy level and the maximum level is increasing from $\hbar\omega \approx 160$ GHz, corresponding to $|\vec{E}| = 0$, to $\hbar\omega \approx 320$ GHz corresponding to $|\vec{E}| = 26$ kV/cm. This is illustrated in Fig.III.29, where the splitting is calculated for $\vec{E} /\!/ <111>$ and

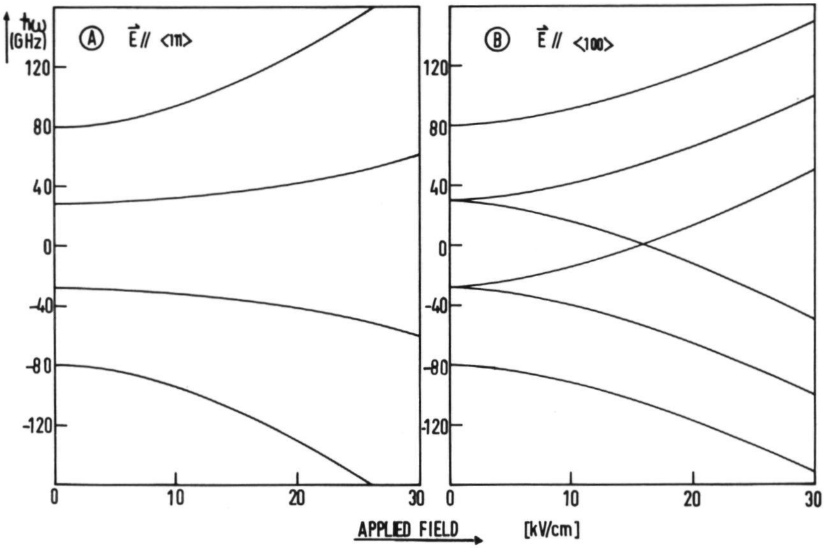

Fig.III.29 Change of the energy of the tunneling states in KCl:^{6}Li in an applied electric field. (A) $\vec{E}$ // <111> (B) $\vec{E}$ // <100>.

// <100>.

Direct evidence for phonon resonance scattering at the individual states was obtained by Walton (6). It appeared that phonons do indeed couple to all tunneling states with about equal strength. Unfortunately, it is impossible to deduce from thermal conductivity experiments which transition between tunneling states contributes to the deviation in the KCl:^{6}Li sample, as compared with the undoped KCl. The resolution of these experiments is limited to kT (6). Therefore, KCl : ^{6}Li would be very interesting to investigate with monochromatic phonons, especially if, in addition, an electric field could be applied. If two identical tunnel junctions are used on opposite faces of a thin KCl : ^{6}Li sample (where at 1 K it is possible to have a mean free path of ≈ 3 mm) one has in essence a monochromatic system. The detector signal should have a decrease when the electric field is high enough to induce a transition. For Sn junctions with a frequency of ~ 300 GHz one would need 25 kV/cm for $E \parallel \langle 111 \rangle$. Instead of Sn, other superconductors such as aluminium ($2\Delta \sim 98$ GHz) could be used.

References

1 R.C. Dynes and V. Narayanamurti, Phys. Rev. B6, 143 (1972).

2 K.F. Renk, in 'Advances in Physics - Festkörperprobleme' (Pergamon Vieweg, 1972, Ed. O. Madelung, Marburg) XII, 107 (1972).

3 For example J.C. King and H.A. Fairbank. Phys. Rev. 93, 21 (1954).

4 V. Bobetic, Phys. Rev. 136, A1535 (1964).

5 A.H. Dayem and J.J. Wiegand, Phys. Rev. B5, 4390 (1972).

6 J.P. Morton and H.M. Rosenberg, Phys. Rev. Letters 8, 200 (1962);

D. Walton, Phys. Rev. Letters 19, 305 (1967).

7 A. Dayem and W. Eisenmenger, Phys. Rev. 18, 125 (1967).

8 C.H. Anderson and E.S. Sabisky, Phys. Rev. Letters 21, 987 (1968).

9 C.H. Anderson, in 'Physical Acoustics' (Academic Press, London, 1971, Ed. W. Mason) Vol. VIII, ch. I, p. 1.

10 K. Renk and J. Deisenhofer, Phys. Rev. Letters 26, 764, (1971).

11 H.J. Schötzan, R. Crettal, E. Grieshaber and F. Kneubrühl, from Proc. Symposium on Submillimeter waves, Brooklyn (1970). p. 431.

12 L.A. Vredevoe, Solid State Comm. 10, 243 (1972).

13 J.R. Sandercock, Phys. Rev. Letters 29, 1735 (1972).

14 P.L. Richards, Y. Shen, K. Yang, J. Appl. Phys. 44, 1417 (1973).

15 L. Tewordt, Phys. Rev. 127, 371 (1962); Phys. Rev. 128, 12 (1962).

16 J.R. Schrieffer and D.M. Ginsberg, Phys. Rev. Letters 8, 207 (1962).

17 E. Burstein, D.N. Langenberg and B.N. Taylor, Phys. Rev. Letters 6, 92 (1961).

18 D.M. Ginsberg, Phys. Rev. Letters 8, 204 (1962).

19 B.I. Miller and A.H. Dayem, Phys. Rev. Letters 18, 1000 (1967).

20 S. Strässler and P. Wyder, Phys. Rev. 158, 319 (1967).

21 J.L. Levine and S.Y. Hsieh, Phys. Rev. Letters 20, 994 (1968).

22 K.E. Gray, A.R. Long and C.J. Adkins, Phil. Mag. 20, 273 (1969).

23 A.H. Dayem and J.J. Wiegand, preprint.

24 A. Rothwarf and B.N. Taylor, Phys. Rev. Letters 19, 27 (1967).

25 A. Rothwarf, Phys. Rev. Letters 23, 468 (1969).

26 A. Dayem, J. Physique 33, Colloque C-4, 21 (1972).

27 A.R. Long and C.J. Adkins, Phil. Mag. 27, 865 (1973).

28 J. Bardeen, L.N. Cooper and J.R. Schrieffer, Phys. Rev. 108, 1175 (1957).

29 M. Tinkham, in 'Low Temperature Physics', Les Houches Lectures (Gordon & Breach, New York, 1962).

30 W.P. Mason, 'Physical Acoustics and the Properties of Solids' (D. van Nostrand, New York, 1958), p. 323 ff.

31 W.P. Mason and H. Bommel, J. Acoust. Soc. Am. 28, 930 (1956).

32 H. Kinder, K. Lassmann and W. Eisenmenger, Phys. Letters 31A, 475 (1970);
H. Kinder, Phys. Rev. Letters 28, 1564 (1972).

33 W. Eisenmenger, in 'Tunneling Phenomena in Solids' (E. Burstein ed., Plenum Press, New York, 1969), p. 371.

34 A.H. Dayem, B.I. Miller and J.J. Wiegand, Phys. Rev. B3, 2949 (1971).

35 H.J. Maris, J. Physique 33, Colloque C-4, 3 (1972).

36 O.Weiss, Z.Angew. Phys. 26, 325 (1969).

37 W.H. Parker and W.D. Williams, Phys. Rev. Letters 29, 924 (1972).

38 R.J. von Gutfeld, in 'Physical Acoustics' (W. Mason Ed., Academic Press, New York, 1968), Part V, Ch. 6, p. 233.

39 J.M. Rowell and P.W. Anderson, Phys. Rev. Letters 10, 230 (1963).

40 M. Fiske and D. Coon, Phys. Rev. 138A, 744 (1965).

41 The sapphire crystals were made with two methods: the Verneuil (42) and the Czochralski (43) growong technique. From the literature, the latter should have a lower dislocation density. However, no difference in behaviour in the experiment was observed.

42 Hrand Djévahirdjian S.A., Monthey, Switzerland.

43 Union Carbide, Crystal Products Division, San Diego, California 92123, U.S.A.

44 F. Nesh, Rev. Sci. Instr. 34, 1437 (1963).

45 Boxcar integrator model 160, Princeton Applied Research.

46 Some magnetic rare earth compounds, such as EuS may be suitable as written in a preliminary article: S. Tansal and H. Sobol, Rev. Sci. Instr. 34, 1075 (1963).

47 Miniature coaxial cable, ϕ 3 mm, serie F supplied by Radiall, Rotterdam, The Netherlands.

48 Pulse amplifier model AV-9T, Avantek, Projecto N.V, Amsterdam, The Netherlands.

49 Preamplifier type B, Princeton Applied Research.

50 The cooperation of Prof. F.L. Stumpers is gratefully acknowledged.

51 Siemens transversal Hall probe RHY 17, supplied by Oxford Instruments, Osney Mead, Oxford, England.

52 R. Berman, E.L. Foster and J.M. Ziman, Proc. Roy. Soc. (London), A231, 130 (1955).

53 The cooperation of Prof. J. Bloem of this Faculty is gratefully acknowledged.

54 Doctoraalscriptie H. Salemink, University of Nijmegen, 1973.

55 B.T. Bernstein, J. Appl. Phys. 34, 169 (1963).

56 R.J. von Gutfeld, J. de Physique 33, C4-1 (1972).

57 V. Narayamurti and R.C. Dynes, Solid State Comm. 12, 341 (1973).

58 V.L. Ginzburg and L.D. Landau, JETP 20, 1064 (1950).

59 L.P. Gorkov, JETP 9, 10 (1963); JETP 29, 333 (1963); JETP 29, 603 (1963); JETP 31, 731 (1964).

60 A.A. Abrikosov and L.P. Gorkov, JETP 12, 1243 (1961).

61 K. Maki, in 'Superconductivity' (Dekker, New York, 1969) p. 1035.

62 J. Millstein and M. Tinkham, Phys. Rev. 158, 325 (1967).

63 D.H. Douglass, Phys. Rev. Letters 7, 14 (1961); D.H. Douglass and L.M. Falicov in 'Progress in Low Temperature Physics' (North-Holland, Amsterdam, 1964) Volume IX, p. 97.

64 P.R. Roach, J.B. Ketterson and M. Kuchnir, Phys. Rev. Letters 25, 1002 (1970); Phys. Rev.A 5, 2205 (1972).

65 H,J. Maris and W.E. Massey, Phys. Rev. Letters 25, 220 (1970); H.J. Maris, Phys. Rev. Letters 28, 277 (1972).

66 R.W. Guernsey, Jr. and K. Luszcynski, Phys. Rev,A 3, 1052 (1971).

67 A. Molinari and T. Regge, Phys. Rev. Letters 26, 1531 (1971).

68 R.C. Dynes, V. Narayamurti and K. Andres, Phys. Rev. Letters 30, 1129 (1973).

69 J.W.M. Bakker, H. van Kempen, H.W.N. Salamink and P. Wyder, Phys. Letters 42A, 193 (1972).

70 V. Narayamurti, K. Andres and R.C. Dynes, Phys. Rev. Letters 31, 687 (1973).

71 H. Haug, Phys. Letters 45A, 170 (1973).

72 A. Dessler and W.M. Fairband, Phys. Rev. 104, 6 (1956).

73 H. Kramers, T. van Peski-Tinbergen, J. Wiebes, F.A. W. van den Burg and C.J. Gorter, Physica 20, 743 (1954).

74 R.D. Maurer and M.A. Herlin, Phys. Rev. 82, 329 (1951).

75 D.T. Meyer, H. Meyer, W. Halliday and C.T. Kellers, Cryogenics 3, 150 (1963).

76 J. Wilks 'The Properties of Liquid and Solid Helium' (Clarendon Press, Oxford, 1967).

77 R.W. Guernsey, K. Luszcynski and W. Mitchell, Cryogenics 7, 110 (1967).

78 L.D. Landau and E.M. Lifshitz, Course of Theoretical Physics, Volume VI (Pergamon Press, Oxford, 1959), Chapter IX.

79 K. Andres, R.C. Dynes and V. Narayamurti, to be published.

80 W.D. Johnston, Jr. and J.G. King, Phys. Rev. Letters 16, 1191 (1966).

81 G. Cataland and H. Plumb, J. Res. NBS 69A, 531 (1965).

82 A.I. Gulyaev, JETP 30, 34 (1970).

83 H.P.P. Harrison, P.P. Peressini and R.O. Pohl, Phys. Rev. 171, 1037 (1968).

84 P.P. Peressini, J.P. Harrison and R.O. Pohl, Phys. Rev. 180, 926 (1969).

APPENDIX

In this Appendix straightforward computer programs (Fortran language) are presented, which were used to compute numerically the expressions (I.40), (I.41), (I.43) and (I.44). The array W(K) denotes the Mühlschlegel numbers (cf. I.4).

```
10 FORMAT('1SPT/SIN')
11 FORMAT(1X,F10.2,F10.2,E20.7,E20.7,E20.7)
13 FORMAT(1X,F4.2)
   WRITE (6,10)
   DIMENSION W(21)
   W(1)=1.0000
   W(2)=0.9999
   W(3)=0.9994
   W(4)=0.9982
   W(5)=0.9957
   W(6)=0.9915
   W(7)=0.9850
   W(8)=0.9760
   W(9)=0.9641
   W(10)=0.9488
   W(11)=0.9299
   W(12)=0.9070
   W(13)=0.8796
   W(14)=0.8471
   W(15)=0.8089
   W(16)=0.7640
   W(17)=0.7110
   W(18)=0.6480
   W(19)=0.5715
   W(20)=0.4749
   W(21)=0.3416
   DI=1.0
   DVOLT=0.1
   TEMP=0.16
   DO 1 K=1,21
   WRITE (6,13) TEMP
   C=1.76*W(K)/TEMP
   VOLT=0.0
   DO 2 I=1,40
   U=VOLT/W(K)
   UU=U*U
   IF (U-1.0) 4,4,5
 5 T1=SQRT(1.0-1.0/UU)
   GO TO 6
 4 T1=1.0
 6 DT=0.005*T1
   T=0.5*DT
   S=0.0
   DO 3 J=1,200
   Y1=1.0/SQRT(1.0-T*T)
   Y2=Y1*Y1*Y1
   Y3=C*(Y1-U)
   Y4=1.0/(1.0+EXP(Y3))
   Y5=C*(Y1+U)
   Y6=1.0/(1.0+EXP(Y5))
   Y7=Y2*(Y4-Y6)*W(K)
   S=S+Y7
 3 T=T+DT
   S=S*DT
   S2=0.0
   IF (U-1.0) 7,7,8
 8 DTT=0.002*(1.0-T1)
   TT=T1+0.5*DTT
   DO 9 J=1,500
   Y1=1.0/SQRT(1.0-TT*TT)
   Y2=Y1*Y1*Y1
   Y3=C*(Y1-U)
   Y5=C*(Y1+U)
   IF (Y3-20.0) 14,14,15
14 Y4=1.0/(1.0+EXP(Y3))
   Y6=1.0/(1.0+EXP(Y5))
   GO TO 16
15 Y4=EXP(-Y3)
   Y6=EXP(-Y5)
16 Y7=Y2*(Y4-Y6)*W(K)
   S2=S2+Y7
 9 TT=TT+DTT
   S2=S2*DTT
 7 CURR=S+S2
   WRITE(6,11)U,VOLT,CURR,S,S2
 2 VOLT=VOLT+DVOLT
 1 TEMP=TEMP+0.04
   STOP
   END
```

The program above calculates the current ('CURR') as a function of V/Δ(0) ('V') (cf. Fig.I.10).

```
10 FORMAT('1SPT/SIN')
11 FORMAT(1X,F10.2,F10.2,E20.7,E20.7,E20.7)
13 FORMAT(1X,F4.2)
   WRITE (6,10)
   DIMENSION W(21)
   W(1)=1.0000
   W(2)=0.9999
   W(3)=0.9994
   W(4)=0.9982
   W(5)=0.9957
   W(6)=0.9915
   W(7)=0.9850
   W(8)=0.9760
   W(9)=0.9641
   W(10)=0.9488
   W(11)=0.9299
   W(12)=0.9070
   W(13)=0.8796
   W(14)=0.8471
   W(15)=0.8089
   W(16)=0.7640
   W(17)=0.7110
   W(18)=0.6480
   W(19)=0.5715
   W(20)=0.4749
   W(21)=0.3416
   TEMP=0.16
   DI=1.0
   DVOLT=0.1
   DO 1 K=1,21
   WRITE (6,13) TEMP
   C=1.76*W(K)/TEMP
   VOLT=0.0
   DO 2 I=1,40
   U=VOLT/W(K)
   UU=U*U
   IF (U-1.0) 4,4,5
 5 T1=SQRT(1.0-1.0/UU)
   GO TO 6
 4 T1=1.0
 6 DT=0.005*T1
   T=0.5*DT
   S=0.0
   DO 3 J=1,200
   Y1=1.0/SQRT(1.0-T*T)
   Y2=Y1*Y1*Y1
   Y3=C*(Y1-U)
   Y4=1.0/(1.0+EXP(Y3))
   Y5=C*(Y1+U)
   Y6=1.0/(1.0+EXP(Y5))
   Y7=-C*Y1*Y1*Y1*(Y4*(Y4-1.0)+Y6*(Y6-1.0))
   S=S+Y7
 3 T=T+DT
   S=S*DT
   S2=0.0
   IF (U-1.0) 7,7,8
 8 DTT=0.002*(1.0-T1)
   TT=T1+0.5*DTT
   DO 9 J=1,500
   Y1=1.0/SQRT(1.0-TT*TT)
   Y2=Y1*Y1*Y1
   Y3=C*(Y1-U)
   Y5=C*(Y1+U)
   IF (Y3-20.0) 14,14,15
14 Y4=1.0/(1.0+EXP(Y3))
   Y6=1.0/(1.0+EXP(Y5))
   GO TO 16
15 Y4=EXP(-Y3)
   Y6=EXP(-Y5)
16 Y7=-C*Y1*Y1*Y1*(Y4*(Y4-1.0)+Y6*(Y6-1.0))
   S2=S2+Y7
 9 TT=TT+DTT
   S2=S2*DTT
 7 RES=1.0/(S+S2)
   WRITE(6,11)U,VOLT,RES,S,S2
 2 VOLT=VOLT+DVOLT
 1 TEMP=TEMP+0.04
   STOP
   END
```

The program above calculates the dynamical normalized resistance ('RES') as a function of V/Δ(0) ('V') (cf. Fig.I.11 and 12). The following program compares the result of the approximale formula (I.43) with the exact formula (I.42).

```
      REAL MC
      WRITE (6,10)
   10 FORMAT(' SPT/SIN')
      DIMENSION W(22)
      W(1)=1.0000
      W(2)=0.9999
      W(3)=0.9994
      W(4)=0.9982
      W(5)=0.9957
      W(6)=0.9915
      W(7)=0.9850
      W(8)=0.9760
      W(9)=0.9641
      W(10)=0.9488
      W(11)=0.9299
      W(12)=0.9070
      W(14)=0.8471
      W(15)=0.8089
      W(16)=0.7640
      W(17)=0.7110
      W(18)=0.6480
      W(19)=0.5715
      W(20)=0.4749
      W(21)=0.3416
      W(22)=0.0000
      TEMP=0.16
      DO 4 K=1,22
      C=1.76*W(K)/TEMP
      WRITE (6,11) TEMP
      CON=1.0E-7
      U=0.05
      DU=0.05
      DO 2 II=1,18
      SOM=0.0
      I=-1
      DO 3 M=1,100000
      J=M
      I=-I
      MC=M*C
      CALL BESK(MC,BES0,BES1)
```

```
      TERM=2*I*BES1*MC
      SOM=SOM+TERM
      IF(ABS(TERM/SOM).LT.CON) GOTO1
    3 CONTINUE
    1 WRITE (6,11) SOM,U,TEMP,J
   11 FORMAT(1X,E20.7,2F5.2,I8)
    2 U=U+DU
    4 TEMP=TEMP+0.04
      STOP
      END
      SUBROUTINE BESK(X,BES0,BES1)
C     BESSELFUNCTIES K0 EN K1
      IF(X-2.0)4,3,3
    3 E=EXP(X)
      W=SQRT(X)
      T=2.0/X
     0AK0=1.25331414-.07832358*T+.02189568*T**2
     1-.01062446*T**3+.00587872*T**4-.00251540*T**5
     2+.00053208*T**6
     0AK1=1.25331414+.23498619*T-.03655620*T**2
     1+.01504268*T**3-.00780353*T**4+.00325614*T**5
     2-.00068245*T**6
      BES0=AK0/(E*W)
      BES1=AK1/(E*W)
      RETURN
    4 H=X/2.0
      D=X/3.75
      G=ALOG(H)
     0AI0=1.0+3.5156229*D**2+3.0899424*D**4
     1+1.2067492*D**6+.2659732*D**8
     2+.0360768*D**10+.0045813*D**12
      AI1=.50+.87890594*D**2+.51498869*D**4
     1+.15084934*D**6+.02658733*D**8
     2+.00301532*D**10+.00032411*D**12
     0AKI0=-.57721566+.42278420*H**2+.23069756*H**4
     1+.03488590*H**6+.00262698*H**8
     2+.00010750*H**10+.00000740*H**12
     0AKI1=1.0+.15443144*H**2-.67278579*H**4
     1-.18156897*H**6-.01919402*H**8
     2-.00110404*H**10-.00004686*H**12
      BES0=AKI0-G*AI0
      BES1=AKI1/X+G*AI1*X
      RETURN
      END
```

The last program calculates the current ('S') for a SS junction as a function of the voltage V/Δ(0) ('VOLT').

```
   11 FORMAT(1X,F10.2,F10.2,E20.7)
   13 FORMAT(1X,F4.2)
      DIMENSION W(21)
      W(1)=1.0000
      W(2)=0.9999
      W(3)=0.9994
      W(4)=0.9982
      W(5)=0.9957
      W(6)=0.9915
      W(7)=0.9850
      W(8)=0.9760
      W(9)=0.9641
      W(10)=0.9488
      W(11)=0.9299
      W(12)=0.9070
      W(13)=0.8796
      W(14)=0.8471
      W(15)=0.8089
      W(16)=0.7640
      W(17)=0.7110
      W(18)=0.6480
      W(19)=0.5715
      W(20)=0.4749
      W(21)=0.3416
      TEMP=0.16
      DO 1 K=1,21
      WRITE (6,13) TEMP
      C=1.76*W(K)/TEMP
      VOLT=0.01
      DO 2 I=1,100
      U=VOLT/W(K)
      IF (U-0.5/C) 21,21,22
   21 DVOLT=0.01
      GO TO 23
   22 DVOLT=0.1
   23 DI=-1.0+SQRT(1.0+1.0/U)
      DX=0.02*DI
      X=1.0+0.5*DX
      S=0.0
      DO 3 J=1,50
      Y1=1.0/(X*X-1.0)
      J=SQRT(Y1+U*U)
      Y2=X*X*J-U*U/J
      Y3=C*(J*X-U)
      Y4=EXP(Y3)
      Y5=1.0/(Y4+1.0)
      Y6=C*(J*X+U)
      Y7=EXP(Y6)
      Y8=1.0/(Y7+1.0)
      IF (C*U-0.01) 7,7,8
    7 Y9=EXP(-C*J*X)
      Y10=(1.0+Y9)*(1.0+Y9)
      Y11=2.0*C*U*Y9/Y10
      GO TO 9
    8 Y11=Y5-Y8
    9 Y12=Y1*Y2*Y11*W(K)
      S=S+Y12
    3 X=X+DX
      S=S*DX
      WRITE (6,11)U,VOLT,S
      IF (VOLT-1.0)2,2,1
    2 VOLT=VOLT+DVOLT
    1 TEMP=TEMP+0.04
      STOP
      END
```

SUMMARY

In its present sophisticated form, the BCS theory describes the phenomena of superconductivity with high accuracy. Superconducting tunnel junctions have been used in many experiments and have mainly led to the believe that the BCS theory, in its more elaborate form, is able to describe the experimental results with an accuracy which is better than 1%. These junctions consist of a three layer structure: a superconductor (S) - isolating layer - and a metal which can be normal (N) or superconducting (S).

In this thesis some promising properties of SS and SN junctions are investigated.

The tunneling effect is explained in the first Chapter with the aid of simple semiconductor diagrams. This simplification is attractive because of the well known energie-gap picture from semiconductors. However, superconductors and semiconductors are basically different and it is shown that one has to be very cautious in the interpretation of the semiconductor diagrams. A more theoretical formalism, based on a tunneling Hamiltonian and first order pertubation theory, leads to the same result as the simple model. Some specific cases have been evaluated and computer calculations are presented so that one can predict the behaviour of a specific junction in terms of the relevant parameters (temperature, energy-gap). The results of the BCS theory are part of the assumptions in the calculations.

In Chapter II the applicability of SN and SS junctions is investigated as absolute thermometers in the temperature range 0.1 T_c to T_c, T_c being the critical temperature of the superconductor. For aluminium used in our experiments this means a range of 0.12 - 1.1 K. As a substrate and cooling agent at the same time, ruby was used. This paramagnetic salt (Al_2O_3+Cr^{3+}) reaches a temperature of ~ 0.08 K after adiabatic demagnetization. We show that the 'BCS' thermometer has many interesting properties: a fast response time ($< 10^{-6}$ sec), a minimum amount of dissipated power (10^{-12} Watt at 1 K) and a high sensitivity. The accuracy is not high as compared to a Ge thermometer; but the 'BCS' thermometer is absolute, which means that no calibration against any other thermometer is needed. SN junctions are better suited for thermometer purposes than SS junctions, as the latter suffers from additional side effects, which tend to obscure the temperature dependence of the junction.

In Chapter III it is shown that superconducting SS junctions can be used as generators and detectors of incoherent, monochromatic phonons with a frequency corresponding to the energy-gap (for tin: $2\Delta \approx 300$ GHz). The practical applicability is investigated by means of phonon transmission through sapphire and ruby. In addition it has been shown that a magnet field is able to tune the frequency of the monochromatic phonons. Apart from the use of SS junctions as quantum detectors, they can also be used as bolometers. The propagation of shock waves through He gas is investigated with the same experimental techniques. Some remarkeable features of the shock waves are treated. Finally, a proposal is made to do a real spectroscopic experiment in KCl : ^{6}Li.

SAMENVATTING

De BCS theorie in zijn huidige vorm beschrijft het gedrag van supergeleiders met een hoge nauwkeurigheid. Supergeleidende tunnel junctions hebben in vele experimenten zeer veel bijgedragen tot de huidige opvatting dat de moderne BCS theorie tot op 1% juist is. Deze junctions bestaan uit een drie lagen struktuur: supergeleider(s) - isolerende laag - en een metaal wat normaal (N) of supergeleidend (S) kan zijn.

In dit proefschrift worden enkele veel belovende eigenschappen onderzocht van SS en SN junctions.

In het eerste hoofdstuk wordt het tunneleffekt aan de hand van halfgeleiderdiagrammen fenomenologisch verklaard. Deze simplificatie ligt voor de hand omdat het beeld van de energie gap vertrouwd is vanuit de halfgeleiders. Supergeleiders zijn echter fundamenteel verschillend;er wordt aangetoond dat voorzichtigheid geboden is bij de interpretatie van de halfgeleiderdiagrammen. Een formalisme met behulp van een tunnel Hamiltoniaan geeft dezelfde resultaten als het eenvoudige model. Tot slot worden in dit hoofdstuk de specifieke gevallen (SN en SS) nader uitgewerkt, en worden computerberekeningen gepresenteerd waardoor het gedrag van SS en SN junctions als funktie van de relevante parameters (temperatuur, energiegap) te voorspellen is. In deze berekeningen is de BCS theorie verwerkt.

Hoodstuk II behandelt de toepassing van SN en SS junctions als

absolute thermometers in het temperatuurgebied van 0.1 T_c tot T_c, waarbij T_c de kritische temperatuur van de supergeleider is. Voor het gebruikte aluminium komt dit overeen met het gebied 0.12 - 1.2 K. Om de junctions te kunnen koelen werd gebruik gemaakt van het paramagnetische zout robijn (Al_2O_3+Cr^{3+}) wat adiabatisch gedemagnetiseerd werd. Er wordt aangetoond dat de 'BCS' thermometer vele goede eigenschappen bezit: een snelle responsie tijd ($< 10^{-6}$ sec), een minimaal gedissipeerd vermogen (10^{-12} Watt bij 1 K) en een hoge gevoeligheid. De absolute nauwkeurigheid is niet zo hoog als bv. een CMN gecalibreerde G_e thermometer. Daarentegen is de 'BCS' thermometer absoluut: er zijn geen extra calibraties nodig tegen een andere thermometer. SN junctions zijn beter geschikt dan SS junctions, omdat bij de laatste vaak neveneffekten optreden, die het temperatuur afhankelijke karakter van de junction verstoren.

In Hoofdstuk III wordt aangetoond dat met behulp van supergeleidende SS junctions incoherente, monochromatische fononen kunnen worden opgewekt en gedetekteerd met een frekwentie, die overeenkomt met de energiegap (voor tin: $2\Delta \approx 300$ GHz). Er wordt onderzocht in hoeverre dit praktisch toepasbaar is aan de hand van fonontransmissie door saffier en robijn. Tevens wordt onderzocht in hoeverre de frekwentie te verstemmen is met behulp van een magneetveld. Dat junctions niet alleen gebruikt kunnen worden als kwantum detektoren wordt aangetoond in het laatste gedeelte, waar de voortplanting van schokgolven in He gas wordt onderzocht. Enkele opvallende eigenschappen van deze golven worden uitvoerig besproken. Tot slot wordt een voorstel gedaan voor een werkelijk spectroscopic experiment in KCl : ^{6}Li.

CURRICULUM VITAE

Ik ben geboren op 20 maart 1946 in Arnhem. Na het eindexamen middelbare school (H.B.S.-B) te hebben afgelegd aan het Thomas à Kempis college te Arnhem begon ik in september 1963 met de studie in de wis- en natuurkunde aan de Katholieke Universiteit van Nijmegen. In 1966 werd het kandidaatsexamen afgelegd (natuur- en wiskunde met scheikunde), en in 1969 het doktoraal examen. Sindsdien ben ik werkzaam als wetenschappelijk medewerker in de groep experimentele natuurkunde IV van de Katholieke Universiteit Nijmegen onder leiding van Prof. P. Wyder. Naast het promotie-onderzoek werd deelgenomen aan het geven van onderwijs in de vorm van werkcolleges en praktika.

Nijmegen, oktober 1973 J.W.M. Bakker

notes

notes

notes

notes

notes

notes

notes

notes